I

Tuhý, M., Hrstka, T., Ettler, V., 2020. Automated mineralogy for quantification and partitioning of metal(loid)s in particulates from mining/smelting-polluted soils. *Environmental Pollution* 266: 115118. https://doi.org/10.1016/j.envpol.2020115118

Environmental Pollution 266 (2020) 115118

Contents lists available at ScienceDirect

Environmental Pollution

journal homepage: www.elsevier.com/locate/envpol

Automated mineralogy for quantification and partitioning of metal(loid)s in particulates from mining/smelting-polluted soils

Marek Tuhý [a], Tomáš Hrstka [b], Vojtěch Ettler [a, *]

[a] Institute of Geochemistry, Mineralogy and Mineral Resources, Faculty of Science, Charles University, Albertov 6, 128 00, Prague 2, Czech Republic
[b] Institute of Geology of the Czech Academy of Sciences, Rozvojová 269, 165 00, Prague 6, Czech Republic

ARTICLE INFO

Article history:
Received 27 May 2020
Received in revised form
25 June 2020
Accepted 25 June 2020
Available online 1 July 2020

Keywords:
Automated mineralogy
Polluted soil
Heavy mineral fraction
Metal(loid)s
Mining and smelting

ABSTRACT

Topsoils near active and abandoned mining and smelting sites are highly polluted by metal(loid) contaminants, which are often bound to particulates emitted from ore processing facilities and/or windblown from waste disposal sites. To quantitatively determine the contaminant partitioning in the soil particulates, we tested an automated mineralogy approach on the heavy mineral fraction extracted from the mining- and smelting-polluted topsoils exhibiting up to 1920 mg/kg As, 5840 mg/kg Cu, 4880 mg/kg Pb and 3310 mg/kg Zn. A new generation of automated scanning electron microscopy (autoSEM) was combined and optimized with conventional mineralogical techniques (XRD, SEM/EDS, EPMA). Parallel digestions and bulk chemical analyses were used as an independent control of the autoSEM-calculated concentrations of the key elements. This method provides faster data acquisition, the full integration of the quantitative EDS data and better detection limits for the elements of interest. We found that As was mainly bound to the apatite group minerals, slag glass and metal arsenates. Copper was predominantly hosted by the sulfides/sulfosalts and the Cu-bearing secondary carbonates. The deportment of Pb is relatively complex: slag glass, Fe and Mn (oxyhydr)oxides, metal arsenates/vanadates and cerussite were the most important carriers for Pb. Zinc is mainly bound to the slag glass, Fe (oxyhydr)oxides, smithsonite and sphalerite. Limitations exist for the less abundant contaminants, which cannot be fully quantified by autoSEM due to spectral overlaps with some major elements (e.g., Sb vs. Ca, Cd vs. K and Ca in the studied soils). AutoSEM was found to be a useful tool for the determination of the modal phase distribution and element partitioning in the metal(loid)-bearing soil particulates and will definitely find more applications in environmental soil sciences in the future.

1. Introduction

The understanding of modal composition (i.e., the relative abundance of individual phases/minerals in %) in a solid sample is of key importance for the quantitative information about the element partitioning (called "deportment") between the individual phases (Pirrie and Rollinson, 2011; Hrstka et al., 2018 and references therein). Scanning electron microscopy (SEM)-based automated mineralogy using QEMSCAN® or MLA (mineral liberation analysis) instruments were originally developed for the mining industry (Fandrich et al., 2007; Lastra, 2007; Rollinson et al., 2011; Gu et al., 2014; Warlo et al., 2019; Meima and Rammlmair, 2020), but have also found applications in mineralogy and petrology (Camm et al., 2003; Power et al., 2009; Pérez-Barnuevo et al., 2013; Hrstka et al., 2018), the characterization of mine tailings (Redwan et al., 2012; Pooler and Dold, 2017), slag materials and slag-derived particulates (Morrison et al., 2016; Pietranik et al., 2018), particulate matter (Williamson et al., 2013) and soils (Kelm et al., 2014; Entwistle et al., 2017; Harvey et al., 2017).

Soils in the vicinity of mining and smelting industries exhibit high concentrations of inorganic contaminants contained in the deposited metal(loid)-bearing particulates with complex mineralogical compositions, which originate from the smelters and/or are windblown from the mine tailing ponds or smelting waste disposal sites (Ettler, 2016 and references therein). Knowledge of the solid speciation and partitioning of metal(loid) contaminants in the heavy mineral fraction (predominantly composed of metal(loid)-bearing particulates) is necessary for understanding their fate and the environmental risks related to their potential mobilization (e.g., during wildfires; see example of Hg in Tuhý et al., 2020 and of Pb in

* Corresponding author.
E-mail address: ettler@natur.cuni.cz (V. Ettler).

https://doi.org/10.1016/j.envpol.2020.115118

Kristensen et al., 2014 and references therein).

The standard approach for visualization and analysis of individual particulates by SEM is extremely time-consuming and generally only up to a few hundred analyses are collected (Knight and Henderson, 2006; Lanteigne et al., 2012; Ettler et al., 2016; Tyszka et al., 2016). When transmission electron microscopy (TEM) is used for the visualization and analysis of nanoparticles in polluted soils, an even lower number of particles are generally analyzed (Schindler and Hochella, 2017; Mantha et al., 2019). Another problem might be related to the analyst/operator bias, because he/she selects the particles for the subsequent analysis by electron microscopy. Especially heavy particles, presumably containing heavy elements like metals and metalloids, attract his/her eyes. As a result, even when hundreds of particles are being analyzed, the resulting statistics might not be representative for the entire studied sample.

Automated mineralogy could overcome these difficulties and its application to highly polluted soils near mining and smelting operations is the major baseline for this article. Here, a new generation of automated SEM was optimized by the quantitative data from an electron microprobe analysis (EPMA) and validated by a parallel bulk chemical analysis. A novel "dot mapping" approach was adopted to provide fast, quantitative and statistically robust data on the complex samples. This approach uses a combination of backscattering electron (BSE) imaging and energy dispersion spectroscopy (EDS) at different resolutions to overcome some common problems related to the analysis of particles with a complex chemistry and fine textures. The main aim was to verify the robustness of this approach and to check whether this new generation technique can really be used for obtaining quantitative data on the partitioning of metal(loid)s in the heavy mineral fraction of a mineralogically complex soil system.

2. Materials and methods

2.1. Soil samples and sample processing

The tested topsoil samples originate from a highly contaminated area near the Tsumeb copper smelter (19°15′S, 17°42′E) in the semi-arid north of Namibia. The smelter has been operating for more than 100 years and is currently processing imported Cu concentrates from all around the world. In July 2013, three biomass-rich topsoil samples (topsoil layer with litter/grass fragments) were collected in a pollution hotspot near the smelter and flotation tailing/slag disposal sites. The three experimental topsoil samples developed under the most common vegetation in the studied area: A - *Acacia* spp., AM - *Acacia* spp. and the marula (*Sclerocarya birrea*) and G - grass (*Aristida stipitata*). The samples were disaggregated in a cutting machine (Fritsch Pulverisette 14) and sieved to <2 mm. Previous investigations have shown that the metal(loid)s in soils affected by the mining and smelting activities are bound to the metal-rich heavy particulates (Ettler, 2016; Ettler et al., 2016; Lanteigne et al., 2012; Tyszka et al. 2016). Therefore, the heavy mineral fractions from the <2 mm fraction of each sample were obtained using 1,1,2,2-tetrabromoethane (density 2.96 g/cm^3), centrifuged at 1800 rpm (Janetzki S70D, Germany) and were further used for the automated mineralogy investigation. The aliquot parts of the original samples and heavy mineral fractions were milled in a planetary agate mill (Fritsch Pulverisette, Germany) to an analytical fineness and were further used for the determination of the bulk chemical compositions and phase compositions using X-ray diffraction analysis (XRD) (see below).

2.2. Bulk chemistry

Both the topsoil samples and heavy mineral fractions were digested in mineral acids. The weighed amount of the sample (0.2 g of the topsoil and 0.05 g of the heavy mineral fraction) was dissolved in Teflon beakers (Savillex®, USA) in 10 ml of HF (49% v/v) and 0.5 ml of $HClO_4$ (70% v/v) overnight on a hot plate (130 °C). The mixture was carefully evaporated to near dryness and the procedure was repeated with an additional 5 ml of HF (49% v/v) and 0.5 ml of $HClO_4$ (70% v/v). The residue was then dissolved in 2% HNO_3 (v/v) and diluted to 100 ml. The obtained digests were analyzed (As, Ca, Cd, Cu, Fe, Pb, Sb, Zn) either by quadrupole-based inductively coupled plasma mass spectrometry (ICP-MS; Thermo-Scientific Xseries^{II}, USA) or, in the Fe and Ca case, by flame atomic absorption spectroscopy (FAAS; Varian SpectrAA 280 FS, Australia).

The accuracy of the digestion procedures and the subsequent analytical measurements (QC/QA: quality control/quality assurance) was continuously controlled by the addition of blank samples and the following certified reference materials: zinc concentrate (CZN-4) and copper concentrate (CCU-1e), both certified by the CCRMP-Canadian Certified Reference Materials Project (CANMET, Canada). A good agreement between the measured and certified values was observed (Table S1).

2.3. Mineralogical investigations

The specimens were analyzed using an X-ray powder diffraction analysis (XRD; Bruker D8 Advanced diffractometer, Germany) equipped with a LynxEye Xe detector, operating with Bragg-Brentano geometry and CuKα radiation ($\lambda_{K\alpha1}$ = 1.540598 Å) at 40 kV and 40 mA over the range of 4–80° 2θ, with a step size of 0.015° and a counting time of 0.8 s per step. X'Pert HighScore Plus 3.0.3 software coupled with Crystallography Open Database (COD) (Gražulis et al., 2012) was used for the phase determination.

The heavy mineral fractions were prepared as polished sections. To exclude the unwanted dissolution of potentially unstable phases, the specimens were polished in alcohol. The samples were firstly examined under a Leica DM LP (Leica, Germany) polarizing microscope. A TESCAN Integrated Mineral Analyzer (TIMA) (TESCAN VEGA3 GMH, Czech Republic) automated scanning electron microscopy (autoSEM) equipped with energy dispersion spectroscopy (EDS; 4 detectors PulseTor 30, USA) was used for scanning all the surfaces of the polished sections, the analysis of the modal compositions, the automated search and identification of metal(loid)-bearing phases and metal(loid) quantitative deportment. Using the TIMA software v1.6.68, the modal and texture analyses were performed using the specifically designed "dot mapping mode" called TIMA DotMapping (TDM) (Hrstka et al., 2018). This method combines a high-resolution (0.4 μm in our case) back-scattering electron (BSE) imaging and a lower resolution (2.5 μm in our case) EDS mapping. The initial BSE scan is used to discriminate particles from the background (epoxy resin) and the grain borders, between the individual phases in the heterogeneous particles. The "lower-resolution" EDS measurements/mapping provides additional elemental information for the phase identification of each segment and helps to detect different phases with the same BSE signal (the detailed parameters of the autoSEM measurements are given in Table S2).

Based on the preliminary autoSEM results, we used an electron probe microanalyzer (EPMA; JEOL JXA-8530F, Japan) equipped with a field emission gun electron source (FEG) for SEM imaging and energy dispersion spectrometry (EDS; spectrometer: JEOL JED-2300F) on the selected sample areas. The same instrument

equipped with five wavelength dispersion spectrometers (WDS) was used for the quantitative chemical analysis of the individual phases (program for the measurement of silicates and oxides with an accelerating voltage of 15 kV and a beam current of 10 nA; program for sulfides, sulfosalts and metallic phases with an accelerating voltage of 20 kV and a beam current of 4 nA) (the standards and detection limits are given in Tables S3 and S4). A total of 250 EPMA spot analyses were acquired. The quantitative EPMA data were used for the optimization of the chemical compositions of individual phases used in the autoSEM software for the phase distribution and element deportment calculations.

The final cross-check of the element partitioning was performed by comparing the autoSEM-calculated results with the bulk chemical compositions of the heavy mineral fractions obtained by the acid digestion.

3. Results and discussion

3.1. Metal(loid)s-bearing particles in mining- and smelter-polluted topsoils

In mining and smelting areas, the majority of contamination is generally concentrated in the topsoil layers (Ettler, 2016 and references therein; Podolský et al., 2015; Mihaljevič et al., 2019) often in the form of contaminant-bearing particles (Ettler et al., 2016; Lanteigne et al., 2012; Leguédois et al., 2004; Schindler and Hochella, 2017). Our samples were collected at <1 km distance from the Tsumeb smelter and the adjacent tailings and slag disposal sites, and the concentrations of the metal(loid) contaminants in the topsoils are very high (mg/kg): As (1020–1920), Cu (4630–5840), Pb (3270–4880), Zn (2410–3310). Cadmium and Sb were found in much lower concentrations (57–81 and 146–266 mg/kg, respectively) (Table S5). Generally, one order of magnitude higher metal(loid) concentrations are found in the heavy mineral fractions indicating that the majority of the contaminants are likely bound to phases of high density. The metal(loid) concentration in the heavy mineral fractions were in the following ranges (mg/kg): As (8800–11100), Cd (99.4–232), Cu (17400–23800), Pb (14100-21200), Sb (2400–2900), Zn (20100–22900). Therefore, for the purpose of understanding the contaminant distribution and partitioning in the particulates, we only used the heavy mineral fractions to be consistent with the previous investigations (Ettler et al., 2016; Tyszka et al., 2016; Harvey et al., 2017).

The XRD analysis indicated that the heavy mineral fractions are composed of both geogenic minerals and phases related to the ore processing. Sample A is predominantly composed of quartz (SiO_2), pyroxene group mineral (diopside; $MgCaSi_2O_6$) and dolomite [$(Ca,Mg)CO_3)_2$], sample AM mainly contains diopside, quartz and olivine (fayalite; Fe_2SiO_4) and sample G contains dolomite and pyroxenes (Fig. S1). However, the phase compositions of the heavy mineral fractions are very complex (also see the other minor phases in Fig. S1), and the diffractograms typically exhibit an elevated background between 15 and 40° 2theta, corresponding to the amorphous and nanocrystalline phases formed at high temperatures during the smelting and refining processes (such as slag glass).

The particles in the studied topsoils exhibit large variability in shapes, sizes and compositions. The typical mineral/phase associations observed in the heavy mineral fractions of the studied topsoils by SEM are shown in Fig. 1. The representative EPMA analyses of the metal(loid)-bearing phases are reported in Tables S6–S11 in the Supplementary Material. The geogenic particles originate from the geological environments, but also correspond to the particles produced by the mechanical processing of the ores (ore and gangue minerals, mine tailing fragments windblown from disposal sites). Dolomite (Fig. 1d, e, f, l), calcite (Fig. 1h), barite (Fig. 1a, c) and quartz (Fig. 1g) belong to the most frequently observed gangue minerals. Anhedral fragments of ore minerals, especially sulfides and sulfosalts, originating from the mineral processing plants are also present: pyrite (FeS_2; Fig. 1b, k, l), chalcopyrite ($CuFeS_2$; Fig. 2d) and enargite (Cu_3AsS_4) are common, because of their high content in the processed ore (Tuhý et al., 2020; Kříbek et al., 2018). Sulfides/sulfosalts usually exhibit well-developed alteration rims composed of metal-bearing Fe oxides (Fig. 1e) or metal rich carbonates (Fig. 1i). Unweathered euhedral grains of pyrite and sphalerite are rarely seen. The EPMA indicates that the primary sulfides/sulfosalts are key metal(loid)-bearing phases among the topsoil particles (Table S6). Arsenates belonging to the adelite mineral group and corresponding to the primary minerals or *in-situ* weathered products are also commonly detected: duftite [$PbCu(AsO_4)(OH)$] and conichalcite [$CaCu(AsO_4)(OH)$] (Fig. 1h, k). Other unidentified Pb-arsenates, phosphates (pyromorphite-like phase) and vanadates (mottramite [$(Cu,Zn)Pb(VO_4)(OH)$]) also occur (Fig. 1h) in agreement with previously published data on metal(loid)s in the Tsumeb soils (Ettler et al., 2016). Secondary carbonates such as azurite [$Cu_3(CO_3)_2(OH)_2$], malachite [$Cu_2(OH)_2CO_3$], smithsonite ($ZnCO_3$) and cerussite (Table S10) are often associated with primary minerals (e.g., geogenic silicates; Fig. 1a, g) and can also be related to the original mineralization or formed during the weathering process. As indicated by SEM/EDS, common carbonates (calcite, dolomite) forming alteration rims around the primary ore minerals are Pb, Cu, Zn-rich (e.g., Fig. 1i). However due to the grain size and porous texture of the objects, it was not possible to quantitatively analyze them by EPMA.

At Tsumeb, the smelting slags are reprocessed by milling and flotation and the obtained slag tailing is used as a cover of old mine tailings to limit the dust dispersion in the area (see the technological details in Ettler et al., 2009 and Jarošíková et al., 2017). However, the studied topsoils contain large amounts of slag fragments, which have been windblown from the nearby disposal sites (Kříbek et al., 2016; Ettler et al., 2016). These heterogeneous grains are predominantly composed of glassy matrix enclosing spinels, silicates and small-size metallic/intermetallic/sulfidic droplets (Fig. 1c, f, h-l). Droplets are formed due to the immiscibility of the sulfidic and silicate melts during the slag quenching (Fig. 1c, f, j) (Piatak et al., 2015 and references therein; Harvey et al., 2017). Some of these droplets correspond to digenite (Cu_9S_5), covellite (CuS), bornite (Cu_5FeS_4), an intermediate solid solution (iss) in the system Cu–Fe–S or other complex intermetallic phases as commonly observed for other slags (Vítková et al., 2010; Piatak et al., 2015; Ettler et al., 2016) (Table S6). Due to their micrometric sizes, these droplets are often difficult to quantitatively analyze by EPMA (e.g., Fig. 1f). Glass is a ubiquitous phase in the slag particles (Fig. 1f, h, j). Despite the high variability in compositions (even within a single slag particle), the glass is usually metal(loid)-rich with up to 33.9 wt. % PbO, 6.61 wt. % ZnO, 3.2 wt. % CuO, 0.26 wt. % CdO and 2.18 wt. % As_2O_5 (Table S11). Euhedral or skeletal grains of spinels (mainly of magnetite composition, Fe_3O_4) and high-temperature silicates (olivine- and melilite-type phases), frequently found in slags (Piatak et al., 2015 and references therein), are embedded in the glass and indicate a relatively quick crystallization from the melt (Fig. 1c, f, j-l; Table S8). Interestingly, no weathering features are developed on the slag grains in contrast to other studies focused on the slag-like particulates in the smelter-affected soils (Leguédois et al., 2004; Knight and Henderson, 2006; Lanteigne et al., 2012; Lanteigne et al., 2014). This phenomenon can be related to the fact that the slag fragments are continuously windblown from the disposal sites and deposited into the

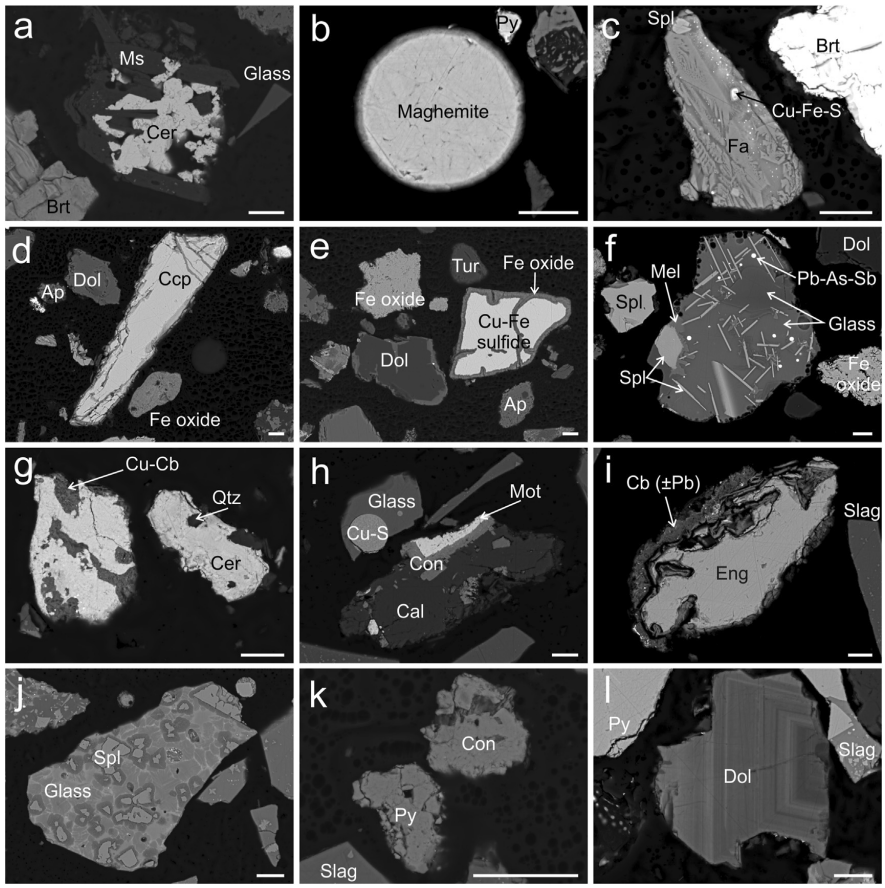

Fig. 1. The back-scattered electron (BSE) micrographs of the typical particle/mineral assemblages in the heavy mineral fraction (a-f: sample AM; g-l: sample A; scale bar represents 10 μm). (a) Cerussite aggregates embedded in muscovite crystals; (b) Spherical smelter-derived maghemite particle; (c) Slag particle composed of skeletal fayalite crystals enclosed in a glassy matrix with sulfidic inclusions and spinels; (d) Chalcopyrite ore grain in association with dolomite, apatite and Fe oxides; (e) Cu-Fe sulfide grain with alteration rim composed of Fe oxide associated with the tourmaline, apatite and dolomite grains; (f) Slag particle composed of melilite, spinels and intermetallic compounds occurring in the glass matrix; (g) Cerussite grains intergrown with Cu-bearing carbonates and quartz; (h) Slag glassy particle with a spherical Cu-S inclusion in association with geogenic calcite intergrown with conichalcite and mottramite; (i) Enargite grain with microcrystalline carbonate rim enriched in Pb; (j) Polyphase slag particle composed of spinel crystals and metal-rich glass; (k) Pyrite and conichalcite grains; (l) Zoned dolomite fragment. Abbreviations: Ap - apatite [$Ca_5(PO_4)_3(F,Cl,OH)$], Brt – baryte ($BaSO_4$), Cal – calcite ($CaCO_3$), Cb – carbonate (variable composition), Ccp – chalcopyrite ($CuFeS_2$), Cer – cerussite ($PbCO_3$), Con – conichalcite [$CaCu(AsO_4)(OH)$], Dol – dolomite [$CaMg(CO_3)_2$], Eng – enargite (Cu_3AsS_4), Fa – fayalite (Fe_2SiO_4), Mel – melilite [$Ca_2(Mg,Al,Fe,Zn)Si_2O_7$], Mot – mottramite [$PbCu(VO_4)(OH)$], Ms – muscovite [$KAl_2(AlSi_3O_{10})(F,OH)_2$], Py – pyrite ($FeS_2$), Qtz – quartz ($SiO_2$), Spl – spinel (variable composition), Tur – tourmaline (variable composition).

soil system, whereas they have been residing in the soil for a long time at other sites (e.g., Mortagne-du-Nord, France; Leguédois et al., 2004). The observed Fe(III) oxides and hydroxides can have variable origins. Maghemite (Fe_2O_3) typically forms rounded particles (Fig. 1b), similar to those observed at other smelting sites (Lanteigne et al., 2012; Ettler et al., 2016). They presumably originate from the roasting/smelting process and were emitted from the smelter as flue dust particles (Walker et al., 2015; Bromstad et al., 2017; Jarošíková et al., 2018); the EPMA indicates that maghemite does not contain significant amounts of metal(loid)s (Table S7). Other Fe(III) oxides and hydroxides as well as Mn oxides are of various origins (geogenic/pedogenic, mine tailings, weathering products) and usually form anhedral grains (Fig. 1d) or porous aggregates (Fig. 1e and f). Some of them are important carriers of metal(loid)s (Pb, Cu, Zn, As) (Table S7).

3.2. Automated mineralogy

3.2.1. Phase distribution

AutoSEM performed between 29 and 75 million analyses and analyzed between 33 and 72 thousand individual particles per sample (Table S2). Fig. 2 shows the comparisons between the BSE images obtained by SEM and the autoSEM phase maps, which indicate the ability of the latter method to even detect sub-micrometric grains (see, e.g., the tiny droplets of Cu sulfides within the slag fragment in Fig. 2e). The quantitative phase distributions including both particles of geogenic and anthropogenic origin are reported in Table 1. The proportion of the individual phases

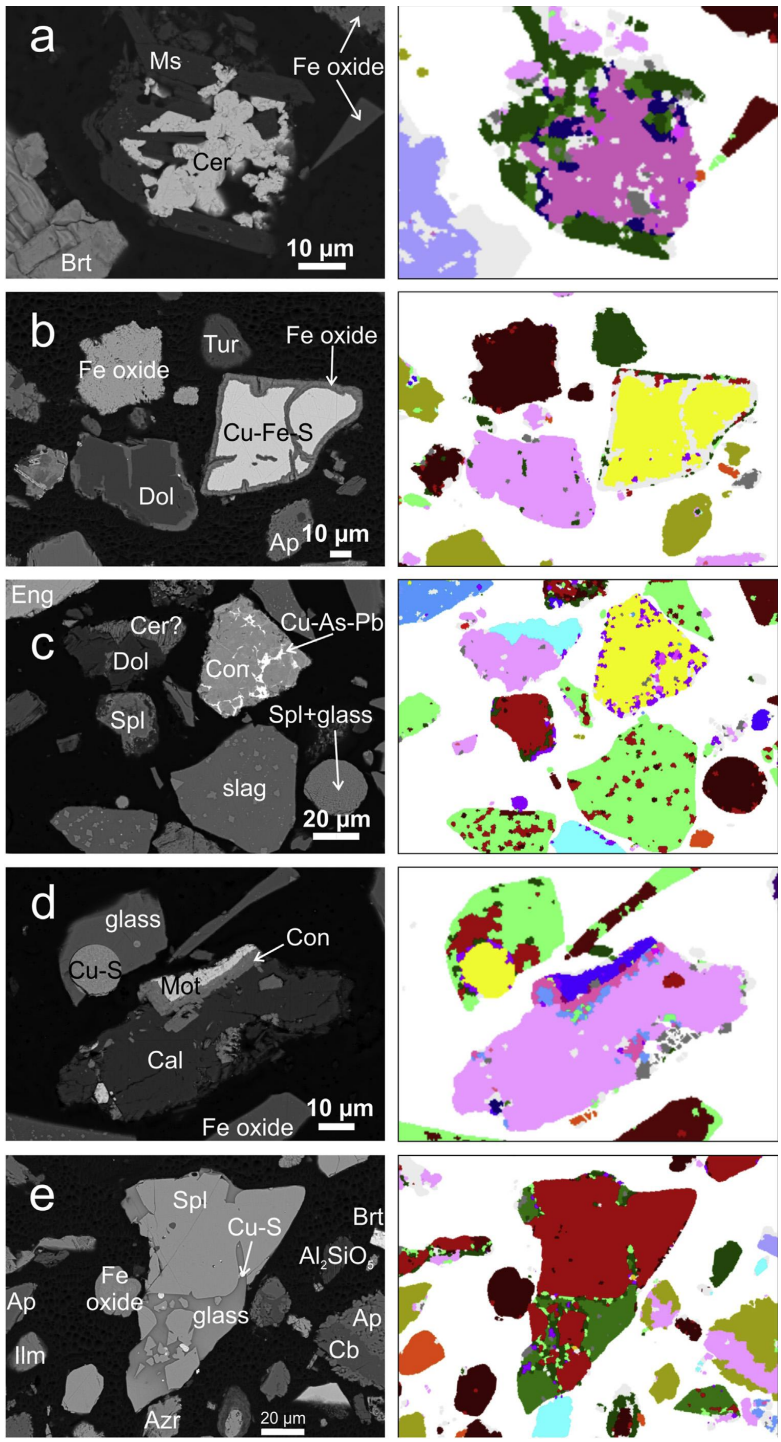

Fig. 2. Comparison of the BSE micrographs of the topsoil heavy mineral fractions and the autoSEM (TIMA) phase maps (a,b: sample AM; c-e: sample A). (a) Cerussite aggregates enclosed in the muscovite crystals; (b) Cu-Fe sulfide grain with altered rim composed of Fe oxide associated with tourmaline, apatite and dolomite; (c) Slag particles in association with carbonates (cerussite, dolomite), spherical slag particles with spinels and glass, conichalcite and intermetallic Cu-As-Pb inclusions (d) Slag glassy fragment with a spherical Cu-S inclusion in association with geogenic calcite intergrown with conichalcite and mottramite; (e) Slag particle composed of spinel crystals embedded in a glass matrix containing Cu sulfide inclusions in association with apatite, ilmenite, Fe oxide, azurite, unspecified Al silicate mineral (Al_2SiO_5) and baryte. For phase abbreviations, see Figure 1. Additional abbreviation: Ilm – ilmenite ($FeTiO_3$), Azr – azurite [$Cu_3(CO_3)_2(OH)_2$]..

Table 1
Phase composition of the heavy mineral fractions of the studied topsoil samples (%).

Class	Mineral/phase	Composition	A	AM	G
Carbonates	Azurite/malachite	$Cu_3(CO_3)_2(OH)_2$/$Cu_2(OH)_2CO_3$	0.6	2.28	0.74
	Calcite/dolomite	$CaCO_3$/$CaMg(CO_3)_2$	4.21	10.71	5.35
	Cerussite	$PbCO_3$	0.57	0.98	0.24
	Smithsonite	$ZnCO_3$	0.81	0.05	0.72
Silicates	Glass	Si—Ca—Fe—Al—Pb—Zn	45.84	4.74	40.65
	Olivine	$(Mg,Fe,Mn)_2SiO_4$	0.47	0.42	0.51
	Quartz	SiO_2	1.1	1.72	0.59
	Other silicates	Variable composition	3.79	10.79	3.87
	Zircon	$ZrSiO_4$	0.22	1.09	0.16
Oxides and hydroxides	Spinel series	$(Zn,Mg,Fe,Cu)(Fe,Al,Cr)_2O_4$	0.28	0.27	0.21
	Fe (oxyhydr)oxides	Fe—O	2.67	28.06	3.15
	Fe (oxyhydr)oxides metal-rich	Fe—O—Pb—Zn—As—Cu	25.74	8.2	22.98
	Rutile/ilmenite	TiO_2, $FeTiO_3$	1.78	5.02	0.92
	Mn oxides	Mn—O-(Pb—Cu—As)	0.04	3.54	0.05
Arsenates/vanadates/phosphates	Apatite group	$Ca_5(PO_4)_3(F,Cl,OH)$	0.86	12.37	1.36
	Conichalcite	$CaCu(AsO_4)(OH)$	0.35	0.01	0.59
	Duftite	$PbCu(AsO_4)(OH)$	0.56	0.19	1
	Monazite	$(REE)PO_4$	0.05	0.1	0.03
	Mottramite	$PbCu(VO_4)(OH)$	0.22	0.71	0.22
	Unidentified arsenates	Variable composition	0.2	0.09	0.36
Sulfides/sulfosalts/metals	Cu sulfides	Cu—S	1.27	1.02	2.27
	Enargite	Cu_3AsS_4	0.49	0.03	1.14
	Galena	PbS	0.15	0.12	0.15
	Metallic Cu	Cu	0.03	0.02	0.05
	Pyrite	FeS_2	1.61	0.41	3.1
	Sphalerite	ZnS	0.19	0	0.35
Others			**5.90**	**7.06**	**9.24**

corresponds to the % of the area in the polished section (epoxy resin excluded). Based on the huge amount of data recorded and the individual particles analyzed per sample (34–72 thousands; Table S2), we might assume that this value corresponds to the volume % in the sample. The topsoils developed under *Acacia* spp. (sample A) and in the grassland (sample G) are similar in the modal phase composition, with the predominant slag glass (40.7–45.8%), metal-rich (oxyhydr)oxides (23–25.7%) and calcite/dolomite (4.21–5.35%). The proportion of the other phases in samples A and G is less than 4%. In contrast, sample AM is depleted in the slag glass (only 4.74%) and is mainly composed of Fe (oxyhydr)oxides (28.1%), apatite group minerals (12.4%) and calcite/dolomite (10.7%). The residue of the other phases ranged from 5.90 to 9.24% (Table 1), which is relatively low in comparison with other studies (Pietranik et al., 2018).

3.2.2. Deportment of metal(loid) contaminants

The results of the deportment of the major contaminants (As, Cu, Pb, Zn) are reported in Table 2. In this case, the percentage corresponds to the fraction of a given element bound within the individual phases/group of phases.

Arsenic is mainly bound to the apatite group minerals (5.6–23.7%), the slag glass (10.4–15.3%) and metal arsenates (duftite, conichalcite, unidentified Pb arsenates; 20.6–28.9%). A

Table 2
Deportment of the major contaminants (As, Cu, Pb, Zn) in the heavy mineral fractions of the topsoil samples (%).

		As			Cu			Pb			Zn		
Phase	**Composition**	**A**	**AM**	**G**	**A**	**AM**	**G**	**A**	**AM**	**G**	**A**	**AM**	**G**
Apatite group	$Ca_5(PO_4)_3(F,Cl,OH)$	20.90	5.56	23.73	1.32	0.09	1.64	1.27	0.11	2.07	2.43	0.94	3.88
Azurite/malachite	$Cu_3(CO_3)_2(OH)_2$/$Cu_2(OH)_2CO_3$	–	–	–	18.77	66.42	15.83	0.12	0.56	0.13	–	–	–
Calcite/dolomite	$CaCO_3$/$CaMg(CO_3)_2$	2.43	4.15	2.56	1.89	0.92	2.29	2.95	2.60	4.48	3.50	10.44	5.47
Cerussite	$PbCO_3$	–	–	–	–	–	–	18.53	39.72	6.51	0.29	3.36	0.08
Conichalcite	$CaCu(AsO_4)(OH)$	11.13	1.00	11.42	3.90	0.10	4.49	–	–	–	–	–	–
Cu sulfides	Cu—S	–	–	–	34.98	17.69	36.68	–	–	–	–	–	–
Duftite	$PbCu(AsO_4)(OH)$	12.26	14.17	13.48	4.30	1.43	5.31	10.06	4.23	16.30	0.42	0.80	0.67
Enargite	Cu_3AsS_4	6.75	1.38	8.81	10.86	0.59	17.55	2.15	0.13	5.09	–	–	–
Fe (oxyhydr)oxides	Fe—O	0.33	11.35	0.23	–	–	–	–	–	–	0.12	6.78	0.12
Fe (oxyhydr)oxides metal-rich	Fe—O—Pb—Zn—As—Cu	10.69	14.42	5.71	7.68	2.60	5.15	21.63	8.51	23.05	22.93	32.46	18.52
Galena	PbS	0.79	2.10	0.47	–	–	–	2.00	2.09	2.00	–	–	–
Glass	Si—Ca—Fe—Al—Pb—Zn	16.73	15.28	10.42	12.70	1.36	7.73	31.10	12.16	27.09	38.24	30.32	36.3
Metallic Cu	Cu	–	–	–	1.37	1.14	1.70	–	–	–	–	–	–
Mn oxides	Mn—O-(Pb—Cu—As)	0.04	6.59	0.04	0.05	2.02	0.05	0.17	9.26	0.23	–	–	–
Mottramite	$PbCu(VO_4)(OH)$	1.07	11.19	0.65	1.82	5.49	1.24	4.41	16.84	3.96	–	–	–
Pb oxides/sulphates	Pb—S—O	–	–	–	–	–	–	0.38	0.13	0.74	–	–	–
Sphalerite	ZnS	–	–	–	–	–	–	–	–	–	5.41	0.09	8.78
Smithsonite	$ZnCO_3$	–	–	–	–	–	–	–	–	–	18.71	6.06	14.65
Unidentified Pb-arsenates	Pb—As—O	3.62	5.39	4.00	–	–	–	4.85	2.63	7.91	0.26	0.63	0.41
Other As phases		12.91	7.16	18.34	–	–	–	–	–	–	–	–	–
Other Zn phases		–	–	–	–	–	–	–	–	–	6.79	7.45	10.09
Residue		**0.35**	**0.26**	**0.14**	**0.36**	**0.15**	**0.34**	**0.38**	**1.03**	**0.44**	**0.9**	**0.67**	**1.03**

significant amount of As is also bound to Fe and Mn (oxyhydr)oxides, which exhibit relatively low As concentrations, but are present in the samples in a relatively high proportion (Tables 1 and S7). Sulfosalts (enargite) and mottramite (where As^V substitutes for V^V, Table S9) are also key As hosts (Table 1). A relatively high amount of As (7.16–18.3%) has not been attributed to any phase group and was assigned as "other As phases. The unclassified As might occur in the autoSEM-undetectable mining- or smelter-derived nanoparticles (Mantha et al., 2019) or in phases not assigned to any group. It is important to recall that the Tsumeb Cu smelter processes As-rich concentrate and the emitted flue dust contains tiny particles of arsenolite (As_2O_3) (Jarošíková et al., 2018). These submicrometric arsenolite crystals have often been detected at the vegetation surfaces in the Tsumeb area (Kříbek et al., 2016, 2018; Tuhý et al., 2017) and could also be deposited into the soil, mainly from leaf litter.

Copper is mainly bound to Cu sulfides and sulfosalts and in the secondary Cu-bearing carbonates, but also occurs to a minor extent in other phases: arsenates and vanadates, the slag glass, Fe and Mn (oxyhydr)oxides (Table 2).

The deportment of Pb is similar for samples A and G in agreement with the similarity in the phase distribution (Tables 1 and 2). Here, the Pb is mainly bound to the slag glass (27.1–31.1%), metal-rich (oxyhydr)oxides (21.6–23.1%) and arsenates (14.9–24.2%). In contrast, the Pb in sample AM is predominantly found in cerussite (39.7%), mottramite (16.8%), slag glass including (sub)micrometric Pb-bearing metallic droplets (12.2%) and Mn oxides (9.26%).

Zinc is mainly hosted in the slag glass particles (30.3–38.2%), metal-rich Fe (oxyhydr)oxides (18.5–32.5%), smithsonite (6.06–18.7%) and primary sphalerite (0.09–8.78%) (Table 2). The zinc is also found in the geogenic or mining-derived carbonates (calcite/dolomite) (up to 10.4%).

Unfortunately, it was not possible to obtain results for Cd and Sb due to their much lower concentrations in the samples compared to the other contaminants. In the case of Cd, there is also an overlap of Cd *Lα* (3.133 keV) with K *Kα* (3.314 keV) in the EDS spectra; in addition, Cd *Lα* overlaps with Ca *Kα* (3.692 keV) in Ca-rich spots. However, based on the test measurements performed, we assume that the Cd is predominantly bound to arsenates (ca. 7%; Table S9), sphalerite (ca. 2%), slag particles (ca. 0.1%; Table S11) and carbonates (ca. 0.1%; Table S10). In the case of Sb, there is also an overlap between Sb *Lα* (3.604 keV) and Ca *Kα* (3.692 keV). However, most of the Sb content was detected in intermetallic droplets of (sub) micrometric size entrapped within the slag glass particles (Fig. 1f). These droplets cannot be readily analyzed by EPMA and, thus, the Sb deportment cannot be quantified. The overall deportment of the studied contaminants (As, Cu, Pb, Zn) was quite successful as indicated by the low % in the residues (corresponding to the unidentified phases).

3.3. Advantages and limitations of the automated mineralogy in soil science

Automated mineralogy is a very convenient method to obtain large numbers of spot analyses in a short period of time (hours) and with a relatively high resolution. This is especially valuable in the mining industries, where information pointing to the process gains that can be made is of crucial importance (Lastra, 2007; Fandrich et al., 2007; Gu et al., 2014). A clear advantage is that the method analyzes the entire sample surface. The typical situation, when an operator makes a series of spot analyses using conventional SEM/EDS and/or EPMA and overlooks some of the important minerals/phases due to his or her fatigue or bias, is overcome (Pirrie and Rollinson, 2011). In this context, instead of analyzing small numbers of grains (up to several tens/hundreds of spot analyses), the autoSEM approach is definitely more suitable and robust for the sample description from the statistical point of view (Pirrie and Rollinson, 2011; Hrstka et al., 2018 and references therein).

The quantitative phase compositions and element deportments calculated by the autoSEM software are more reliable when the software database of mineral compositions is optimized by the EPMA. This approach is often necessary for complex environmental samples, such as contaminated soils. However, this requires several steps of analysis: (1) pre-screening by autoSEM; (2) the EPMA-WDS analyses of the phases selected on the basis of the autoSEM preliminary data; (3) a final evaluation using an EPMA-optimized autoSEM database. This is a time-consuming procedure especially in the early stages of the investigation and is strictly based on the experience and set of skills of the autoSEM operator, who is responsible for the data acquisition and final processing.

Pirrie and Rollinson (2011) define the conditions for the statistical validity of the autoSEM measurements based on the number of particles analyzed within one sample, which is, in turn, related to the grain size of the sample prepared as a standard 30-mm polished resin block. Moreover, it also depends on the abundance of the phases of interest in a given sample. The main issue is the sample preparation, because a density-dependent segregation of particles in an epoxy resin might appear. This problem can be overcome by sample replication, re-polishing and re-analyzing (e.g., Hrstka, 2008; Pirrie and Rollinson, 2011). Mixing the sample with laboratory-grade graphite of a small grain size can also solve the density-related problems during the sample preparation; this approach will reduce the differential settling of the heavier particles (Pirrie and Rollinson, 2011). Vertical transverse sectioning is also a suitable approach, which could be applied to solve this problem (Pooler and Dold, 2017).

In this study, we checked the accuracy of the autoSEM-calculated results by comparing them with the bulk chemical analysis of the sample (Table 3). Despite the fact that our polished sections were prepared in a standard way (without preventing the differential settling of the particles), a very good agreement was achieved (Table 3) and the obtained autoSEM data can be considered accurate. This indicates that the parallel digestion and bulk chemical analysis of the sample is a good way to verify the autoSEM-calculated element deportments and might reduce the cost of the analyses and data processing time of any additional replicates. Measurement mode optimization can play an important role in providing the best data in a reasonable timeframe and with reduced costs. The newly developed TDM (applied in the present study) or other novel measurement techniques provide significant benefits compared to the original QEMSCAN® and MLA analysis routines. Apart from the speed improvements related to TDM, the major benefits of the TIMA system is the full integration of the quantitative EDS analysis and the use of a patented segmentation algorithm, which allows for the automated summing of the spectra from the homogenous areas of the individual grains and provides

Table 3
Comparison of the bulk metal(loid) concentrations calculated by autoSEM with the bulk chemical analyses obtained by the acid digestion of the heavy mineral fractions of the studied topsoils (in wt.%).

Code	A		AM		G	
Element	autoSEM	Digestion	autoSEM	Digestion	autoSEM	Digestion
As	0.82	1.11	0.25	0.88	1.34	0.94
Ca	4.76	5.80	7.84	5.49	4.75	5.92
Cu	2.07	2.38	2.17	1.74	3.03	1.98
Fe	30.66	27.12	28.16	29.10	28.37	26.80
Pb	2.16	2.12	1.79	1.41	2.40	1.96
Sb	-	0.25	–	0.29	–	0.24
Zn	2.25	2.29	0.41	2.01	2.56	2.15

better detection limits for the elements of interest (Hrstka et al., 2018). While similar detection limits can be reached under specific settings on the QEMSCAN® system resulting in an increased X-ray counts per pixel, this comes with a huge time penalty and limits the real-life applications of such an approach (Andersen et al., 2009).

There are numerous limitations of using autoSEM for contaminated soil investigations. Our contaminated topsoils are specific because they contain a large number of grains of variable grain size and very complex phase compositions compared to standard (ore)-geology samples which generally have much larger crystals and smaller phase diversity (Fandrich et al., 2007; Pirrie and Rollinson, 2011; Hrstka et al., 2018). In addition, soil heavy mineral fractions probably do not correspond to the overall contamination of the soil samples. The mass of the heavy mineral fraction separated from the contaminated soils is rarely reported and it is, thus, impossible to make quantitative calculations. According to our own measurements (experimental topsoils; $n = 3$), the heavy mineral fraction of the <2-mm sieved topsoils accounted for 4.31 ± 1.81% of the total mass. However, when the amounts of metal(loid)s bound to the heavy mineral fractions are calculated, they correspond to 24.3 ± 8.44% of the total content in the topsoil (median: 21.5%), which is a relatively modest amount of the total metal(loid)s contained in the samples. It means that part of the contamination can be bound to a less dense soil fraction, such as metal(loid)-bearing phases embedded/locked in larger crystals of quartz, calcite and other geogenic minerals. Moreover, contaminant-bearing particles might be attached to the plant surfaces (e.g., leaf cuticle) in the form of (nano)particles (Kříbek et al. 2014, 2016; 2018; Tuhý et al., 2017; Uzu et al. 2009) or absorbed by the plants' roots (Kříbek et al. 2014; Mihaljevič et al. 2015; Uzu et al. 2009) and end up in the soil organic matter (Mantha et al., 2019), which is finally not a part of the heavy mineral fractions that were examined.

In complex soil systems, there is also a problem with the software setting of the concentration boundaries in the individual phases, where element substitutions may occur. In smelter-polluted areas, where slag fragments are frequently found in soils, glass can exhibit large variability in contaminant concentrations (Table S11; see Ettler et al., 2009). Subsequently, the classification and clustering of phases according to the variability in their compositions is highly dependent on the experience of the operator and/or the other persons, who are processing the data. Applications of machine learning/artificial intelligence (ML/AI)-assisted clustering are under development to overcome these limitations (Hrstka et al., 2017a,b).

4. Conclusions

Heavily polluted soils in the vicinity of mining and smelting industries contain numerous metal(loid)-bearing particulates, which exhibit very complex mineralogical compositions. Risk element partitioning in these phases cannot be quantitatively evaluated using conventional techniques, such as the standard SEM/EDS and/or EPMA, which provide relatively low numbers of analyses and can be affected by operator bias. For this purpose, a new generation of automated mineralogy was applied to the heavy mineral fractions of the topsoil samples polluted by emissions from a Cu smelter and the particulates from the nearby waste disposal sites (tailings, slags). The deportment of the metal(loid)s, occurring in high concentrations (thousands of mg/kg) in the studied topsoils, was quantitatively performed: As, Cu, Pb and Zn were predominantly found in the slag glassy particles, sulfides/sulfosalts and Fe and Mn (oxyhydr)oxides. For the studied soils, limitations still exist for contaminants found in lower concentrations (less than the lower hundreds of mg/kg, such as Sb and Cd), which cannot be fully determined due to the spectral overlaps with the major elements and/or nugget effects. Nevertheless, when combined with traditional mineralogical techniques (XRD, SEM/EDS, EPMA), autoSEM with the novel "dot mapping" mode is a useful tool for the determination of the modal phase distribution as well as the textural relations (e.g., liberation, association, exposure). This technique provides a valuable insight into element partitioning, which is of key importance for the assessment of the metal(loid)s' environmental fate in soils.

CRediT authorship contribution statement

Marek Tuhý: Conceptualization, Resources, Methodology, Investigation, Formal analysis, Validation, Visualization, Writing - original draft, Writing - review & editing, Funding acquisition. **Tomáš Hrstka:** Methodology, Investigation, Formal analysis, Visualization, Writing - review & editing. **Vojtěch Ettler:** Conceptualization, Resources, Methodology, Investigation, Formal analysis, Visualization, Writing - original draft, Writing - review & editing, Funding acquisition, Supervision, Project administration.

Declaration of competing interest

The authors declare that they have no known competing financial interests or personal relationships that could have appeared to influence the work reported in this paper.

Acknowledgements

This study was supported by the Czech Science Foundation (GAČR project no. 19-18513S) and a student grant attributed to Marek Tuhý from the Grant Agency of Charles University (GAUK 1598218). The Charles University team was partially supported by institutional funding from the Center for Geosphere Dynamics (UNCE/SCI/006). The research at the Institute of Geology ASCR was co-financed by the institutional support of RVO 67985831 and Strategy AV21/4 of the Czech Academy of Sciences. Part of the equipment used for this study was purchased from the Operational Programme Prague – Competitiveness (Project CZ.2.16/3.1.00/21516). The kind help of our colleagues is gratefully acknowledged: Michal Čurda (XRD), Martin Racek (EPMA), Marie Fayadová (digestions), František Veselovský (heavy mineral fraction separation). Mr. Alan Harvey Cook is thanked for his review of the English in the manuscript. We acknowledge the thorough reviews of four anonymous reviewers, which substantially helped to improve the original version of the manuscript and the Associate Editor, prof. Jörg Rinklebe, for handling the manuscript.

Appendix A. Supplementary data

Supplementary data to this article can be found online at https://doi.org/10.1016/j.envpol.2020.115118.

References

Andersen, J.C.O., Rollinson, G.K., Snook, B., Herrington, R., Fairhurst, R.J., 2009. Use of QEMSCAN® for the characterization of Ni-rich and Ni-poor goethite in laterite ores. Miner. Eng. 22, 1119–1129. https://doi.org/10.1016/j.mineng.2009.03.012.

Bromstad, M.J., Wrye, L.A., Jamieson, H.E., 2017. The characterization, mobility, and persistence of roaster-derived arsenic in soils at Giant Mine. NWT. Appl. Geochem. 82, 102–118. https://doi.org/10.1016/j.apgeochem.2017.04.004.

Camm, G.S., Butcher, A.R., Pirrie, D., Hughes, P.K., Glass, H.J., 2003. Secondary mineral phases associated with a historic arsenic calciner identified using automated scanning electron microscopy; a pilot study from Cornwall, UK. Miner. Eng. 16, 1269–1277. https://doi.org/10.1016/j.mineng.2003.07.005.

Entwistle, J.A., Hunt, A., Boisa, N., Dean, J.R., 2017. Enhancing the interpretation of in vitro bioaccessibility data by using computer-controlled scanning electron

microscopy (CCSEM) at the individual particle level. Environ. Pollut. 228, 443–453. https://doi.org/10.1016/j.envpol.2017.03.050.
Ettler, V., 2016. Soil contamination near non-ferrous metal smelters: a review. Appl. Geochem. 64, 56–74. https://doi.org/10.1016/j.envpol.2014.04.035.
Ettler, V., Johan, Z., Kříbek, B., Veselovský, F., Mihaljevič, M., Vaněk, A., Penížek, V., Majer, V., Sracek, O., Mapani, B., Kamona, F., Nyambe, I., 2016. Composition and fate of mine- and smelter-derived particles in soils of humid subtropical and hot semi-arid areas. Sci. Total Environ. 563–561, 329–339. https://doi.org/10.1016/j.scitotenv.2016.04.133.
Ettler, V., Johan, Z., Kříbek, B., Šebek, O., Mihaljevič, M., 2009. Mineralogy and environmental stability of slags from the Tsumeb smelter, Namibia. Appl. Geochem. 24, 1–15. https://doi.org/10.1016/j.apgeochem.2008.10.003.
Fandrich, R., Gi, Y., Burrows, D., Moeller, K., 2007. Modern SEM-based mineral liberation analysis. Int. J. Miner. Process. 84, 310–320. https://doi.org/10.1016/j.minpro.2006.07.018.
Gražulis, S., Daškevič, A., Merkys, A., Chateigner, D., Lutterotti, L., Quirós, M., Serebryanaya, N.R., Moeck, P., Downs, R.T., LeBail, A., 2012. Crystallography Open Database (COD): an open-access collection of crystal structures and platform for world-wide collaboration. Nucleic Acids Res. 40, D420–D427. https://doi.org/10.1093/nar/gkr900.
Gu, Y., Schouwstra, R.P., Rule, C., 2014. The value of automated mineralogy. Miner. Eng. 58, 100–103. https://doi.org/10.1016/j.mineng.2014.01.020.
Harvey, P.J., Rouillon, M., Dong, C., Ettler, V., Handley, H.K., Taylor, M.P., Tyson, E., Tennant, P., Telfer, V., Trinh, R., 2017. Geochemical sources, forms and phases of soil contamination in an industrial city. Sci. Total Environ. 584–585, 505–514. https://doi.org/10.1016/j.scitotenv.2017.01.053.
Hrstka, T., 2008. Preliminary results on the reproducibility of sample preparation and QEMSCAN® measurements for heavy mineral sands samples. Proceedings of 9th International Congress for Applied Mineralogy. Australasian Institute of Mining and Metallurgy, Carlton, Australia, pp. 107–111.
Hrstka, T., Gottlieb, P., Moravec, J., Lokoč, J., 2017a. The future of SEM-based automated mineralogy and artificial intelligence in applied mineralogy. In: Fiore, S. (Ed.), Applied Mineralogy & Advanced Materials. Scientific Research Abstracts, vol. 6. Digilabs, Bari, p. 42.
Hrstka, T., Motl, D., Gottlieb, P., Hladil, J., 2017b. Using an automated approach in building a dust particle atlas for research and environmental monitoring. In: Fiore, S. (Ed.), Applied Mineralogy & Advanced Materials. Scientific Research Abstracts, vol. 6. Digilabs, Bari, p. 43.
Hrstka, T., Gottlieb, P., Skála, R., Breiter, K., Motl, D., 2018. Automated mineralogy and petrology — applications of TESCAN integrated mineral analyzer (TIMA). J. Geosci. 63, 47–63. https://doi.org/10.3190/jgeosci.250.
Jarošíková, A., Ettler, V., Mihaljevič, M., Kříbek, B., Mapani, B., 2017. The pH-dependent leaching behavior of slags from various stages of a copper smelting process: environmental implications. J. Environ. Manag. 187, 178–186. https://doi.org/10.1016/j.jenvman.2016.11.037.
Jarošíková, A., Ettler, V., Mihaljevič, M., Drahota, P., Culka, A., Racek, M., 2018. Characterization and pH-dependent environmental stability of arsenic trioxide-containing copper smelter flue dust. J. Environ. Manag. 209, 71–80. https://doi.org/10.1016/j.jenvman.2017.12.044.
Kelm, U., Avendano, M., Balladares, E., Helle, S., Karlsson, T., Pinchera, M., 2014. The use of water-extractable Cu, Mo, Zn, As, Pb concentrations and automated mineral analysis of flue dust particles as tools for impact studies in topsoil exposed to past emissions of a Cu-smelter. Chem. Erde 74, 365–373. https://doi.org/10.1016/j.chemer.2013.12.001.
Knight, R.D., Henderson, P.J., 2006. Smelter dust in humus around Rouyn-Noranda. Québec. Geochem.-Explor. Environ. Anal. 6, 203–214. https://doi.org/10.1144/1467-7873/05-087.
Kristensen, L.J., Taylor, M.P., Odigie, K.O., Hibdon, S.A., Flegal, A.R., 2014. Lead isotopic compositions of ash sourced from Australian bushfires. Environ. Pollut. 190, 159–165. https://doi.org/10.1016/j.envpol.2014.03.025.
Kříbek, B., Šípková, A., Ettler, V., Mihaljevič, M., Majer, V., Knésl, I., Mapani, B., Penížek, V., Vaněk, A., Šráček, O., 2018. Variability of the copper isotopis composition in soil and grass affected by mining and smelting in Tsumeb, Namibia. Chem. Geol. 493, 121–135. https://doi.org/10.1016/j.chemgeo.2018.05.035.
Kříbek, B., Majel, V., Knésl, I., Keder, J., Mapani, B., Kamona, F., Mihaljevič, M., Ettler, V., Penížek, V., Vaněk, A., Šráček, O., 2016. Contamination of soil and grass in the Tsumeb smelter area, Namibia: modeling of contaminants dispersion and ground geochemical verification. Appl. Geochem. 64, 75–91. https://doi.org/10.1016/j.apgeochem.2015.07.006.
Kříbek, B., Majer, V., Knésl, I., Nyambe, I., Mihaljevič, M., Ettler, V., Šráček, O., 2014. Concentrations of arsenic, copper, cobalt, lead and zinc in cassava (*Manihot esculenta* Crantz) growing on uncontaminated and contaminated soils of the Zambian Copperbelt. J. Afr. Earth Sci. 99, 713–723. https://doi.org/10.1016/j.jafrearsci.2014.02.009.
Lanteigne, S., Schindler, M., McDonald, A.M., Skeries, K., Abdu, Y., Mantha, N.N., Murayama, M., Hawthorne, F.C., Hochella Jr., M.F., 2012. Mineralogy and weathering of smelter-derived spherical particles in soils: implications for the mobility of Ni and Cu in the surficial environment. Water Air Soil Pollut. 223, 3619–3641. https://doi.org/10.1007/s11270-012-1135-3.
Lanteigne, S., Schindler, M., McDonald, A., 2014. Distribution of metal(loid)s in smelter-derived particulate matter in soils, mineralogical insights into their retention and release in a low-T environment. Can. Mineral. 52, 453–471. https://doi.org/10.3749/canmin.52.3.453.
Lastra, R., 2007. Seven practical application cases of liberation analysis. Int. J. Miner. Process. 84, 337–347. https://doi.org/10.1016/j.minpro.2006.07.017.
Leguédois, S., van Oort, F., Jongmans, T., Chevallier, P., 2004. Morphology, chemistry and distribution of neoformed spherulites in agricultural land affected by metallurgical point-source pollution. Environ. Pollut. 130, 135–148. https://doi.org/10.1016/j.envpol.2003.12.023.
Mantha, H., Schindler, M., Hochella, M.F., 2019. Occurrence and formation of incidental metallic Cu and CuS nanoparticles in organic-rich contaminated surface soils in Timmins, Ontario. Environ. Sci.: Nano 6, 163–179. https://doi.org/10.1039/s8en00994e.
Meima, J.A., Rammlmair, D., 2020. Investigation of compositional variations in chromitite ore with imaging laser induced breakdown spectroscopy and spectral angle mapper classification algorithm. Chem. Geol. 532, 119376. https://doi.org/10.1016/j.chemgeo.2019.119376.
Mihaljevič, M., Baieta, R., Ettler, V., Vaněk, A., Kříbek, B., Penížek, V., Drahota, P., Trubač, J., Šráček, O., Chrastný, V., Mapani, B., 2019. Tracing the metal dynamics in semi-arid soils near mine tailings using stable Cu and Pb isotopes. Chem. Geol. 515, 61–76. https://doi.org/10.1016/j.chemgeo.2019.03.026.
Mihaljevič, M., Ettler, V., Vaněk, A., Penížek, A., Svoboda, M., Kříbek, B., Šráček, O., Mapani, B.S., Kamona, A.F., 2015. Trace elements and the lead isotopic record in marula (*Sclerocarya birrea*) tree rings and soils near the Tsumeb smelter, Namibia. Water Air Soil Pollut. 226, 177. https://doi.org/10.1007/s11270-015-2440-4.
Morrison, A.L., Swierczek, Z., Gulson, B.L., 2016. Visualisation and quantification of heavy metal accessibility in smelter slags: the influence of morphology on availability. Environ. Pollut. 210, 271–281. https://doi.org/10.1016/j.envpol.2015.11.030.
Pérez-Barnuevo, L., Pirard, E., Castroviejo, R., 2013. Automated characterization of intergrowth textures in mineral particles. A case study. Miner. Eng. 52, 136–142. https://doi.org/10.1016/j.mineng.2013.05.001.
Piatak, N.M., Parsons, M.B., Seal II, R.R., 2015. Characteristics and environmental aspects of slag: a review. Appl. Geochem. 57, 236–266. https://doi.org/10.1016/j.apgeochem.2014.04.009.
Pietranik, A., Kierczak, J., Tyszka, R., Schulz, B., 2018. Understanding heterogeneity of a slag-derived weathered material: the role of automated SEM-EDS analyses. Minerals 8, 513. https://doi.org/10.3390/min8110513.
Pirrie, D., Rollinson, G.K., 2011. Unlocking the applications of automated mineral analysis. Geol. Today 27, 226–235. https://doi.org/10.1111/j.1365-2451.2011.00818.x.
Podolský, F., Ettler, V., Šebek, O., Ježek, J., Mihaljevič, M., Kříbek, B., Šráček, O., Vaněk, A., Penížek, V., Majer, V., Mapani, B., Kamona, F., Nyambe, I., 2015. Mercury in soil profiles from metal mining and smelting areas in Namibia and Zambia: distribution and potential sources. J. Soils Sediments 15, 648–658. https://doi.org/10.1007/s11368-014-1035-9.
Pooler, R., Dold, B., 2017. Optimization and quality control of automated quantitative mineralogy analysis for acid rock drainage prediction. Minerals 7, 12. https://doi.org/10.3390/min7010012.
Power, M.R., Pirrie, D., Camm, G.S., Andersen, J.C.Ø., 2009. The mineralogy of efflorescence on as calciner building in SW England. Miner. Mag. 73, 27–42. https://doi.org/10.1180/minmag.2009.073.1.27.
Redwan, M., Rammlmair, D., Meima, J.A., 2012. Application of mineral liberation analysis in studying micro-sedimentological structures within sulfide mine tailing and their effect on hardpan formation. Sci. Total Environ. 414, 480–493. https://doi.org/10.1016/j.scitotenv.2011.10.038.
Rollinson, G.K., Andersen, J.C.O., Stickland, R.J., Boni, M., Fairhurst, R., 2011. Characterization of non-sulphide zinc deposits using QEMSCAN®. Miner. Eng. 24, 778–787. https://doi.org/10.1016/j.mineng.2011.02.004.
Schindler, M., Hochella Jr., M.F., 2017. Sequestration of Pb-Zn-Sb- and As-bearing incidental nanoparticles by mineral surface coatings and mineralized organic matter in soils. Environ. Sci.-Process Impacts 19, 1016–1027. https://doi.org/10.1039/c7em00202e.
Tuhý, M., Rohovec, J., Matoušková, Š., Mihaljevič, M., Kříbek, B., Vaněk, A., Mapani, B., Göttlicher, J., Steininger, R., Majzlan, J., Ettler, V., 2020. The potential wildfire effects on mercury remobilization from topsoils and biomass in a smelter-polluted semi-arid area. Chemosphere 247, 125972. https://doi.org/10.1016/j.chemosphere.2020.125972.
Tuhý, M., Ettler, V., Mihaljevič, M., Rohovec, J., Hrstka, T., Matoušková, Š., 2017. Mineralogy of smelter- and mining- derived particles in semi-arid soils and their potential mobilization during wildfires. In: Mercier-Langevin, P., Dube, B., Bardoux, M., Ross, P.S., Dion, C. (Eds.), Mineral Resources to Discover Vols 1-4. Society for Geology Applied to Mineral Deposit (SGA), Geneva, pp. 1229–1231.
Tyszka, R., Pietranik, A., Kierczak, J., Ettler, V., Mihaljevič, M., Medynska-Juraszek, A., 2016. Lead isotopes and heavy minerals analyzed as tools to understand the distribution of lead and other potentially toxic elements in soils contaminated by Cu smelting (Legnica, Poland). Environ. Sci. Pollut. Res. 23, 24350–24363. https://doi.org/10.1007/s11356-016-7655-4.
Uzu, G., Sobanska, S., Aliouane, Y., Pradere, P., Dumat, C., 2009. Study of lead phytoavailability for atmospheric industrial micronic and sub-micronic particles in relation with lead speciation. Environ. Pollut. 154, 1178–1185. https://doi.org/10.1016/j.envpol.2008.09.053.
Vítková, M., Ettler, V., Johan, Z., Kříbek, B., Šebek, O., Mihaljevič, M., 2010. Primary and secondary phases in copper-cobalt smelting slags from the Copperbelt Province, Zambia. Mineral. Mag. 74, 581–600. https://doi.org/10.1180/minmag.2010.074.4.581.
Walker, S.R., Jamieson, H.E., Lanzirotti, A., Hall, G.E.M., Peterson, R.C., 2015. The effect of ore roasting on arsenic oxidation state and solid phase speciation in

gold mine tailings. Geochem. Explor. Environ. Anal. 15, 273–291. https://doi.org/10.1144/geochem2013-238.

Warlo, M., Wanhainen, C., Bark, G., Butcher, A.R., McElroy, I., Brising, D., Rollinson, G.K., 2019. Automated quantitative mineralogy optimized for simultaneous detection of (precious/critical) rare metals and base metals in a production-focused environment. Minerals 9, 440. https://doi.org/10.3390/min9070440.

Williamson, B.J., Rollinson, G., Pirrie, D., 2013. Automated mineralogical analysis of PM10: new parameters for assessing PM toxicity. Environ. Sci. Technol. 47, 5570–5577. https://doi.org/10.1021/es305025e.

II

Tuhý, M., Rohovec, J., Matoušková, Š., Mihaljevič, M., Kříbek, B., Vaněk, A., Mapani, B., Göttlicher, J., Steininger, R., Majzlan, J., Ettler, V., 2020. The potential wildfire effects on mercury remobilization from topsoils and biomass in a smelter-polluted semi-arid area. *Chemosphere* 247: 125972. https://doi.org/10.1016/j.chemosphere.2020.125972

Chemosphere 247 (2020) 125972

Contents lists available at ScienceDirect

Chemosphere

journal homepage: www.elsevier.com/locate/chemosphere

Short Communication

The potential wildfire effects on mercury remobilization from topsoils and biomass in a smelter-polluted semi-arid area

Marek Tuhý [a, **], Jan Rohovec [b], Šárka Matoušková [b], Martin Mihaljevič [a], Bohdan Kříbek [c], Aleš Vaněk [d], Ben Mapani [e], Jörg Göttlicher [f], Ralph Steininger [f], Juraj Majzlan [g], Vojtěch Ettler [a, *]

[a] Institute of Geochemistry, Mineralogy and Mineral Resources, Faculty of Science, Charles University, Albertov 6, 128 00, Prague 2, Czech Republic
[b] Institute of Geology, Academy of Sciences of the Czech Republic, Rozvojová 269, 165 00, Prague 6, Czech Republic
[c] Czech Geological Survey, Geologická 6, 152 00, Prague 5, Czech Republic
[d] Department of Soil Science and Soil Protection, Faculty of Agrobiology, Food and Natural Resources, Czech University of Life Sciences Prague, Kamýcká 129, 165 21, Prague 6, Czech Republic
[e] Department of Geology, Faculty of Science, University of Namibia, Private Bag, 13301, Windhoek, Namibia
[f] Institute for Photon Science and Synchrotron Radiation, Karlsruhe Institute of Technology, Hermann-von-Helmholtz-Platz 1, DE-76344, Eggenstein-Leopoldshafen, Germany
[g] Institute of Geosciences, Friedrich-Schiller University, Burgweg 11, D-07749, Jena, Germany

HIGHLIGHTS

- Wildfires can affect smelter-impacted soils and vegetation in semi-arid Namibia.
- Mercury released from contaminated biomass-rich topsoils at ~340 °C.
- Smelter surroundings (184 km^2) contain ~300 kg of Hg remobilizable by wildfire.

GRAPHICAL ABSTRACT

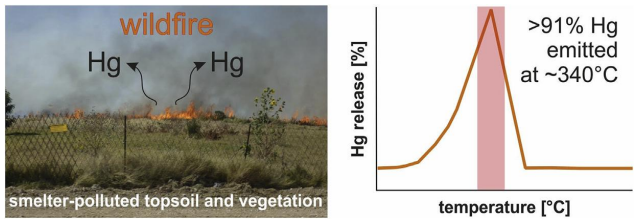

ARTICLE INFO

Article history:
Received 26 August 2019
Received in revised form
6 January 2020
Accepted 18 January 2020
Available online 21 January 2020

Patryk Oleszczuk

Keywords:
Mercury
Topsoils
Vegetation
Wildfire

ABSTRACT

Wildfires can be responsible for significant mercury (Hg) emissions especially in contaminated areas. Here, we investigated the Hg distribution in topsoils and vegetation samples and temperature-dependent Hg mobilization from biomass-rich topsoils collected near a copper (Cu) smelter in Tsumeb (semi-arid Namibia), where Hg-rich Cu concentrates are processed. The thermo-desorption (TD) experiments conducted on representative biomass-rich topsoils (3.9–7.7 mg Hg/kg) indicated that more than 91% of the Hg was released at ~340 °C, which corresponds to the predominant grassland-fire conditions. The mineralogical investigation indicated that the Hg comes mainly from the deposited smelter emissions because no distinct Hg-rich microparticles corresponding to the windblown dust from the nearby disposal sites of the technological materials (concentrates, slags, tailings) were found. A comparison with the TD curves of the Hg reference compounds confirmed that the Hg in the biomass-rich topsoils occurs as a mixture of Hg bound to the organic matter and metacinnabar (black HgS), which exhibits similarities with the TD pattern of smelter flue dust residue. Despite the installation of a sulfuric acid plant in the smelter in 2015 and a calculated drop in the estimated Hg emissions (from 1301 ± 457 kg/y for the period 2004–2015 to 67 ± 5 kg/y after 2015), the Hg legacy pool in the smelter

* Corresponding author.
** Corresponding author.
E-mail addresses: marek.tuhy@natur.cuni.cz (M. Tuhý), ettler@natur.cuni.cz (V. Ettler).

https://doi.org/10.1016/j.chemosphere.2020.125972

Smelter pollution
Semi-arid Namibia

surroundings can potentially be re-emitted back to the atmosphere by wildfire. Using the Hg spatial distribution data in the area (184 km^2), the estimates indicate that up to 303 kg and 1.3 kg can be remobilized from the topsoils and vegetation, respectively.

1. Introduction

Mercury (Hg) is a global pollutant and understanding its cycling on Earth is of key importance (Driscoll et al., 2013), especially because of the predicted increase in Hg emissions (Streets et al., 2009). Biomass combustion significantly contributes to the Hg flux into the atmosphere (Campos et al., 2015; Friedli et al., 2003, 2009; Navrátil et al., 2009; Pirrone et al., 2010; Selin, 2009; Wiedinmeyer and Friedli, 2007), with an estimated annual release of 675 ± 240 tons of Hg, which represent 13% of the natural contribution (Friedli et al., 2009; Pirrone et al., 2010). Combustion processes during wildfires have significant effects on soil (Pereira et al., 2019), which is an important pool responsible for Hg sequestration on the continents (Giesler et al., 2017; Smith-Downey et al., 2010). Despite the temperature- and speciation-dependence of Hg release (Hojdová et al., 2009; Navarro, 2008; Reis et al., 2015; Rumayor et al., 2017), wildfires cause almost complete Hg remobilization from the vegetation cover, litter and topsoil (Abraham et al., 2018a; Campos et al., 2015; Engle et al., 2006; Friedli et al., 2001, 2003), with Hg emissions mainly in the form of gaseous elemental Hg (Hg^0) (Friedli et al., 2001). The risk of wildfire-driven Hg remobilization can be magnified in the proximity of single pollution sources (e.g., mines and smelters), where soils exhibit elevated Hg concentrations (Abraham et al., 2018b; Ettler et al., 2007).

About 80% of the world's refined copper (Cu) today is produced by pyrometallurgical technologies (Schlesinger et al., 2011). However, due to the long-term decrease of the Cu ore grade (Mudd and Jowitt, 2018) and the depletion of the Cu reserves suitable for such pyrometallurgical processing, the treatment of low-quality Cu ores, especially arsenic-bearing concentrates has now come to the forefront (Safarzadeh et al., 2014). Copper ores containing enargite (Cu_3AsS_4) and tennantite ($Cu_{12}As_4S_{13}$) exhibit elevated concentrations of As, but also other deleterious elements (Sb, Bi, Hg), which complicate the technological process itself and can also be harmful for the environment. Understanding the fate of the Hg in the environmental compartments affected by the Cu smelting is the main motivation for our study, which focuses on (i) the Hg spatial distribution in the vegetation and topsoil samples near an operating Cu smelter in the semi-arid north of Namibia and (ii) the experimental evidence of Hg release from contaminated biomass-rich topsoils using a thermo-desorption analysis (TD) to simulate wildfire conditions. The obtained results, combined with the reported Cu smelter production rate and calculated smelter-related Hg annual emissions, were used to estimate the Hg emissions potentially generated by wildfires in this semi-arid area.

2. Materials and methods

2.1. Field sampling

The samples were collected in the vicinity of the Tsumeb Cu smelter (19°15′S, 17°42′E) in northern Namibia. Tsumeb is situated 1310 m above sea level, approximately 375 km NNE of Windhoek, the capital of Namibia. The area exhibits a subtropical semi-arid climate with average annual temperatures of 25 °C, 470 mm of rainfall and 30% relative humidity. South-easterly winds are the most frequent in the area (Figs. 1 and S1). Easterly winds also occur during the winter months, whereas during summer (January) and autumn (April), north-easterly winds are more frequent (Ettler et al., 2016; Kříbek et al., 2016). The smelter has been operating for more than 100 years and is currently processing imported Cu concentrates containing enargite and tennantite from all around the world (the historical and technological details are contained the Supplementary Material). The mining and smelting activities at this site left huge amounts of various waste (tailings, slags) (Jarošíková et al., 2017) and caused the substantial contamination of the nearby soils (Kříbek et al., 2016; Podolský et al., 2015). Previous screening of the smelter-affected soils at this and other smelting sites (Ettler et al., 2007; Podolský et al., 2015) indicated that Hg is mainly bound in the uppermost soil horizons, but it has been experimentally documented that the fires severely affect only the first cm of the soil (Badía et al., 2017; Girona-García et al., 2018). For this reason, in order to understand the spatial distribution of the potentially remobilizable Hg by wildfires around the Tsumeb smelter, topsoil samples (depth 0–1 cm; n = 28) and vegetation samples (mainly grass species *Aristida stipitata* and *Eragrostis porosa*; n = 30) were collected in 2004 to cover the area of ca. 184 km^2 (the details on the sampling/sample processing are given in Kříbek et al., 2016). In July 2013, three larger biomass-rich topsoil samples (topsoil with litter/grass fragments) were collected in the most contaminated zone near the smelter and flotation tailing/slag disposal sites. They developed under the commonest vegetation in the studied area: A - *Acacia* sp., AM - *Acacia* sp. and marula [*Sclerocarya birrea*] and G - grass (*Aristida stipitata*) (Fig. S1) (Ettler et al., 2016; Kříbek et al., 2016). These samples (denoted as the "experimental samples" below) were disaggregated in a cutting machine (Fritsch Pulverisette 14), sieved to <2 mm, milled in a planetary agate mill (Fritsch Pulverisette) to an analytical fineness and were further used for wildfire simulation experiments. To decipher the role of dust generated by mining and smelting in the contamination of the topsoils and vegetation, waste materials from the historical disposal sites (tailings, n = 5; slags, n = 4) and technological samples originating from the smelter (feed concentrates, n = 2; flue dust cleaning residues, n = 4) (Table 1) were collected in June 2012 and July 2013.

2.2. Bulk chemical and mineralogical analyses

The total Hg concentrations in all the samples were determined using cold-vapor atomic absorption spectrometry (CV-AAS; Leco-Altec AMA 254). Mercury spatial distributions and surface area calculations around the Tsumeb smelter were plotted and calculated using the Surfer software, version 10 (Golden Software Inc.) (Kříbek et al., 2016). The total sulfur (S_{tot}), the total, the organic and the inorganic carbon (C_{tot}, C_{org} and C_{inorg}) contents were determined using the combination of the ELTRA CS 530 and CS 500 TIC analyzers. The analytical details and quality control/quality assurance data (QC/QA) using certified reference materials are given in Table S1.

The phase composition of the samples was determined using X-ray diffraction analysis (XRD; PANalytical X'Pert Pro). The selected technological and all the experimental samples were further investigated using scanning electron microscopy (SEM) and a field-

Table 1
Chemical and mineralogical characteristics of the samples.

Samples	Characteristics	Hg [ng/g]	C_{tot} [%]	S_{tot} [%]	Mineralogy (XRD)[a]
Experimental topsoils	A — acacia litter [*Acacia* spp.]	7660	17.59	0.547	Qtz, Ms, Kfs, Cal, Dol, Mag
	AM — acacia [*Acacia* spp.] + marula [*Sclerocarya birrea*] litter	6300	22.47	0.614	Qtz, Ms, Kfs, Cal, Dol, Mag
	G — grass fragments	3880	15.18	0.256	Qtz, Ms, Kfs, Cal, Dol, Mag
Spatial distribution	Vegetation (n = 30)	2.97—186	NA	NA	NA
	Topsoil (n = 28)	23.3—3790	NA	NA	NA
Technological	C1 — Cu concentrate (Bulgaria)	20,700	0.200	37.2	Py, Cpy, Tn, Enr, Qtz
	C2 — Cu concentrate (Chile)	39,900	0.462	35.2	Py, Enr, Ccp, Pn, Qtz
	Flue gas residues (n = 4)	3330 - 219 000[1]	4.15[3]	3.00[3]	Ars, Cla, Gp, Qtz, Gn[3]
	Tailings (n = 5)	306—35,10[1]	7.25—8.52	0.059—2.21	Dol, Ms, Kfs, Qtz, Gp, Cal[2]
	Slags (n = 4)	193—844[1]	0.056—0.889	0.421—6.27	Gl, Spl, Ol, Qtz, Cpx[2]

NA - not analyzed.
References: [1]Podolský et al. (2015), [2]Ettler et al. (2019), [3]Jarošíková et al. (2018).
[a] Abbreviations: Ars — arsenolite (As_2O_3), Cal — calcite ($CaCO_3$), Ccp — chalcopyrite ($CuFeS_2$), Cla — claudetite (As_2O_3), Cpx — clinopyroxene ($CaFeSi_2O_6$), Dol — dolomite ($CaMgCO_3$), Enr — enargite (Cu_3AsS_4), Gl — glass, Gn — galena (PbS), Gp — gypsum ($CaSO_4 \cdot 2H_2O$), Kfs — K-feldspar ($KAlSi_3O_8$), Mag — magnetite (Fe_3O_4), Ms — muscovite $[KAl_2(Si_3Al)O_{10}(OH,F)_2]$, Ol — olivine ($Fe_2SiO_4$), Pn — pentlandite $[(Fe,Ni)_9S_8]$, Py — pyrite (FeS_2), Qtz — quartz (SiO_2), Spl — spinel $[(Fe^{2+},Mg,Zn)(Fe^{3+},Al,Cr)_2O_4]$, Tn — tennantite $[(Cu,Fe)_{12}As_4S_{13}]$.

emission gun electron probe microanalyzer (FEG-EPMA; JEOL JXA-8530F). The X-ray absorption near-edge structure (XANES) and the extended X-ray absorption fine structure (EXAFS) spectra of the powdered experimental and technological samples and reference compounds were collected at the SUL-X beamline at the Angströmquelle Karlsruhe (ANKA, Eggenstein-Leopoldshafen, Germany). The spectra were measured either in the transmission mode (for the standards) or in the fluorescence mode (for the samples) at the Hg L_1 (14.84 keV) and L_3 (12.28 keV) edges. Micro-X-ray fluorescence (μ-XRF) spectroscopy (Bruker M4 TORNADO) was used on the polished sections prepared for the experimental samples to check the sample homogeneity and verify the potential presence of Hg-rich hotspots. The analytical details related to the mineralogical investigations are given in the Supplementary Material.

2.3. Simulation of Hg remobilization during wildfires

The thermo-desorption (TD) experiments were applied to the experimental samples to simulate the temperature-dependent Hg release (Leco-Altec AMA 254 CV-AAS; temperature range: 75—670 °C regulated using the software modification). An experimental sample was placed into a heating cell (quartz) throughout the experiment for all the temperature steps. At each temperature step, Hg captured on amalgamator was released and quantified according to the calibration common for bulk Hg measurements. Despite the fact that the TD experiments are often carried out in an inert atmosphere (N_2) to avoid interferences and undesired reactions (Rumayor et al., 2017), our experiments were conducted under an O_2 gas flow to better simulate the wildfire conditions. However, selected runs were also performed under an N_2 atmosphere to avoid an uncontrolled O_2-driven biomass burning. In total, each TD curve was constructed from 16 data points. The TD experiment was conducted in 3 replicates for the experimental samples (n = 3), for the Hg-bearing Cu concentrates (n = 2), the other selected technological samples (tailing, slag, flue gas residue) (n = 1) and the following reference compounds: Metranal®3 Strawberry Leaves reference material (produced by Analytika Ltd., Czech Republic, representing the Hg bound to the organic matter, OM) and synthetic compounds such as metacinnabar (black HgS), cinnabar (red HgS), red HgO and Hg(II) adsorbed to goethite (FeOOH). All the mineral reference compounds were prepared according to the methodology described by Hojdová et al. (2009) by diluting with quartz powder or alumina before the TD analysis. The experimental samples were also studied using thermogravimetry (TG; SDT 650, TA Instruments) to determine the temperature-related mass loss (25—1000 °C; step: 10 °C/min; air).

3. Results and discussion

3.1. Mercury concentration and solid speciation

The dust particles from the waste disposal sites and emissions from the Tsumeb smelter are thought to be major sources of contamination in the area (Ettler et al., 2019; Jarošíková et al., 2017; Kříbek et al., 2016; Podolský et al., 2015). At the time of sampling (2012—2013), the smelter processed Hg-rich copper concentrates imported from Bulgaria and Chile grading 21—40 mg Hg/kg (Table 1) (dundeeprecious.com; Jarošíková et al., 2017). Despite quite variable Hg concentrations in Cu concentrates worldwide (up to 6000 mg/kg; median: 4 mg/kg, mean: 62 mg/kg) (Hylander and Herbert, 2008), the mean Hg concentration (30.3 mg/kg) in the concentrates processed at Tsumeb is far above the world median value. Mercury in the concentrates is mainly bound in sulfosalts (up to 0.27 wt% Hg) and sulfides (up to 0.18 wt% Hg) (Tables 1 and S3; Fig. S2). Given the volatile behavior of Hg during the high-temperature smelting process (Hylander and Herbert, 2008; Wiederhold et al., 2013), its concentrations in the flue gas residues are much higher than in the slags (3300—219,000 ng/g and 193—844 ng/g, respectively) (Table 1). Mercury occurs in the Tsumeb smelter flue dust in residual and newly formed sulfides, sulfosalts, (inter)metallic phases and unidentified complex phases (Fig. S2) (Jarošíková et al., 2018). Mercury concentrations in the tailings (306—3510 ng/g) are slightly higher than in the slags, however, no specific Hg-bearing phases were identified (Table 1).

Mercury in the vegetation samples collected around the Tsumeb site is significantly lower (2.97—186 ng/g) than in the topsoils (23.3—3790 ng/g) (Table 1), but the two datasets exhibited a statistically significant correlation (Pearson correlation coefficient: r = 0.4075, P = 0.0314). The Hg spatial distribution patterns indicate that the prevailing wind direction has a significant role in the Hg transport (Fig. 1). Nevertheless, the shape of the Hg hotspot in the topsoils is less elongated likely due to the limited transport distance of the particles from the smelter and the nearby disposal sites. In contrast, Hg in the vegetation probably reflects the ability of plants to uptake the gaseous Hg (Lodenius et al., 2003; Millhollen et al., 2006), which can be transported over larger distances from the source (Wu et al., 2014; Yin et al., 2009). The experimental samples exhibit higher concentrations (3880—7660 ng/g) than the

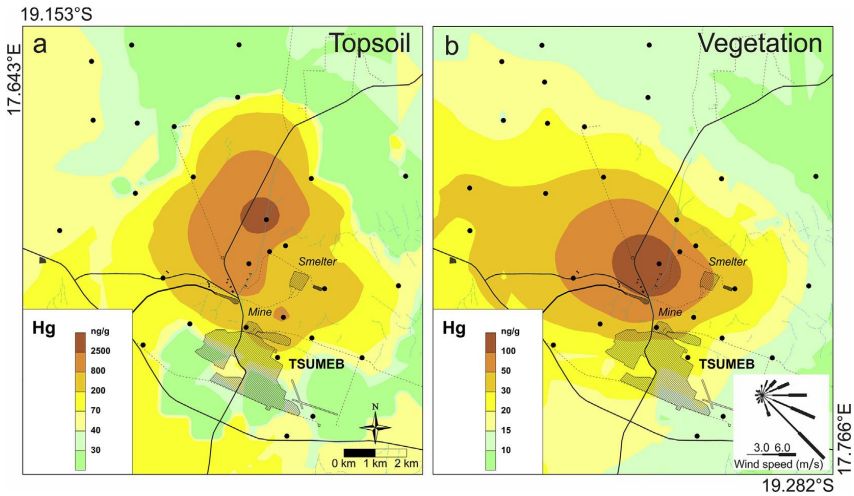

Fig. 1. Mercury spatial distribution in the topsoils (A) and the vegetation (B) around the Tsumeb smelter. The sampling points are marked by the black dots.

topsoils sampled in 2004, which can be attributed to an increase in the smelter production and the Hg emissions over time (Table S4). No specific Hg-bearing phases were detected in the experimental samples (Table 1). Despite numerous attempts to optimize the XAS measurements, the resulting data did not yield the desired information about the Hg speciation in our experimental and technological samples due to the low Hg concentrations for this method and overlaps of the Hg L_3 edge with a more intense As *K* edge. The μ-XRF did not reveal any Hg hotspots (Hg-rich particles) in the experimental samples preventing the application of μ-XANES and μ-EXAFS (more details given in the Supplementary Material).

3.2. Thermo-desorption and Hg released during a simulated wildfire

The thermo-desorption curves for the experimental samples are similar and show a sharp peak at ~340 °C, indicating that more than 91% of Hg was remobilized at this temperature (Fig. 2a). The TG measurements show a massive weight loss (17–30%) of the samples between 250 and 450 °C (Fig. S6a), which might be related to the combustion processes under the oxygen-rich atmosphere. Nevertheless, the same TD results were obtained under the N_2-atmosphere (Fig. S6b) and confirmed that, in this case, the Hg release is not influenced by the O_2-driven uncontrolled biomass burning in the instrument furnace. The TD curves of the technological materials indicated that the peak of the Hg release occurred in the temperature interval of 210–480 °C (maximum: ~260 °C) for the flue gas residue, in the interval of 260–550 °C (maximum: ~420 °C) for the slag and the mine tailing and in the interval of 260–550 °C (maximum: ~480 °C) for both concentrates (Fig. 2b). The TD patterns of the reference compounds are reported in Fig. 2c. Mercury bound to the organic matter exhibited an Hg release in the

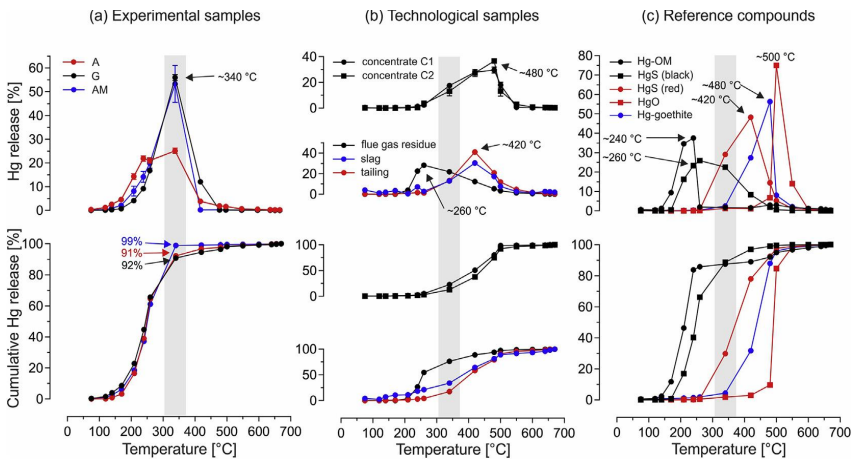

Fig. 2. Mercury thermo-desorption curves for (a) the biomass-rich topsoils (experimental samples), (b) the technological samples (Cu concentrates, flue gas residue, slag, tailings) and (c) the reference compounds indicating a temperature-dependent Hg release.

temperature interval of 140–260 °C (peak maximum: ~240 °C) followed by metacinnabar (black HgS) exhibiting a rather flat release pattern in the interval of 210–480 °C (maximum: ~260 °C) very similar to the flue gas residue (Fig. 2b and c). Cinnabar (red HgS) and Hg bound to the goethite exhibited an Hg release in the temperature range of 340–550 °C, but had maximum peaks at ~420 °C and ~480 °C, respectively. The TD curve of HgO indicated that the Hg release in the temperature interval of 420–550 °C with the peak at ~500 °C. A comparison of the TD curves for the reference compounds with the literature data show some differences, which might be caused by the variability of the experimental setups used; however, the temperature-dependent sequence is similar to those reported in other TD studies (Hojdová et al., 2009; Reis et al., 2015; Rumayor et al., 2017). Given the fact that it was not possible to determine the exact Hg speciation in the experimental samples using a combination of mineralogical and spectroscopic techniques, based on the TD curves of the reference compounds, it can be hypothesized that the Hg in the experimental samples occurs as a mixture of Hg bound to the organic matter and metacinnabar, which presumably originates from the flue gas stream in the smelter. Metacinnabar can be formed by the roasting/smelting of the ores (Kim et al., 2004) and it is more stable than cinnabar at more than ~400 °C (Ballirano et al., 2013). We assume that, if present, the metacinnabar in our biomass-rich topsoils is probably associated with nm-sized particulates, because no distinct Hg-bearing particles were found in the experimental samples by the conventional techniques (Fig. S5). The occurrence of ultra-micrometric particles is quite common in flue dust residues from smelting (Jarosíková et al., 2018; Fig. S2c) and the similarity between the TD patterns of the metacinnabar and the flue dust residue supports this hypothesis (Fig. 2b and c).

3.3. Environmental implications

The temperatures during wildfires range from 50 °C up to 1500 °C (Neary et al., 1999), but for grassland fires they generally reach their maximum at ~350 °C for a short period of time (Ryan, 2002). Friedli et al. (2007) demonstrated that Hg was completely released from organic soils at 300 °C after 5 min heat exposure, which is in agreement with our TD result showing an almost complete Hg remobilization at ~340 °C (Fig. 2a). The potential Hg remobilizations were calculated to estimate a wildfire event affecting all the studied area. For this prediction, we used the Hg spatial distribution data from 2004 (Fig. 1) and measured the mass of the grass and topsoil per area (grass: 256 ± 70 g/m^2, height of 40–45 cm during the dry season, n = 9; topsoils: 6050 ± 2330 g/m^2, depth 0–1 cm, n = 10). Based on the previous investigations showing that the burning is mainly limited to the first cm and the temperatures beneath the burned soil surface rapidly decrease with the depth (Badía et al., 2017; Girona-García et al., 2018), we assume that our spatial Hg distribution data for the vegetation and topsoil (0–1 cm) can be used to predict the "worst-case scenario" of the wildfire-driven Hg remobilization in the studied area. The predictions were calculated for the hotspots and the entire studied area (Fig. 1) and indicate that up to 1.3 kg of Hg from the vegetation cover (grass) and 303 kg of Hg from the topsoil can be remobilized during such a wildfire event (Table 2). The amounts of remobilizable Hg for the entire studied area (vegetation: 0.07 g/ha, topsoil: 16.45 g/ha) are in the same order of magnitude as those at other sites (Europe: 1.1–75.1 g/ha; North America: 0.36–30 g/ha) (Campos et al., 2015; Engle et al., 2006; Navrátil et al., 2009; Webster et al., 2016). The remobilizable Hg in the hotspots is much higher and corresponds to 0.5 g Hg/ha for the vegetation and 229 g Hg/ha for the topsoil (Table 2).

Our study site cannot compete with the much larger area of boreal forests of the northern hemisphere, where wildfires have been identified as significant sources of atmospheric Hg pollution (Friedli et al. 2007, 2009; Wiedinmeyer and Friedli, 2007). However, it represents a significant source of Hg contamination due to high fire frequency in the area and due to the continuous Hg enrichment of the vegetation, litter and topsoil derived from an operating Cu smelter. The emissions from Cu smelters are dependent on the adopted flue gas cleaning technologies. The Tsumeb smelter commissioned a sulfuric acid plant (SAP) in 2015, but the flue-gas cleaning technology before this was only based on simple dust collectors (DC) and fabric filters (FF; bag-house units). We estimated the Hg emissions from the Tsumeb smelter for the time period of 2004–2018 based on the Cu production, the mean Hg concentration in the concentrates (30.3 mg/kg) and the Hg removal efficiencies of the individual flue-gas cleaning technologies [DC + FF: 66% (Wu et al., 2016); DC + FF + SAP: 99% (Hylander and Herbert, 2008; Wu et al., 2016)]. The estimated Hg emissions for the period 2004–2015 were 760–2022 kg Hg/y (average: 1301 ± 457 kg Hg/y) (Table S4). After the installation of the SAP, the Hg emissions dropped to 61–73 kg Hg/y (average: 67 ± 5 kg Hg/y) for the period 2016–2018 (Table S4). Despite high uncertainties in these calculations (e.g., the changing composition of feed concentrates and their Hg concentrations) (Wu et al., 2016), our estimates are in a good agreement with the predictions of Hg emissions for Namibia (AMAP/UNEP, 2013). For instance, 1836 kg Hg resulting from non-ferrous metal production were predicted for year 2010 (AMAP/UNEP, 2013), while our calculation yielded 1225 kg Hg for the Tsumeb smelter, which is currently the only smelting facility in Namibia (Table S4). It has been nevertheless reported that only 14% of the Hg emissions from smelters are deposited locally and most emissions go into the global pool (Wu et al., 2014). Thus, the calculated Hg deposition in the local ecosystem corresponded to 106–283 kg Hg/year for the period before the installation of the SAP; this amount roughly agrees with the total Hg pool in the vegetation and topsoil calculated for our 2004 data (Table 2).

Apart from wildfires, spontaneous Hg re-emissions from the contaminated soils can occur (Agnan et al., 2016; Briggs and Gustin, 2013; Eckley et al., 2016; Zhu et al., 2016, 2018). The review papers indicate that the highest soil Hg fluxes were observed at abandoned Hg mining sites and also in naturally enriched soil environments (up to thousands of ng/m^2/h; Agnan et al., 2016; Eckley et al., 2016; Zhu et al., 2016 and references therein). Elevated Hg soil fluxes were also reported near Cu smelters; for example, Eckley et al. (2015) found that after the closure of a Cu smelter in Canada, Hg emissions from the polluted soil increased and accounted for 108 ng/m^2/h. At this rate, the Hg re-emissions can last for hundreds of years before the background Hg concentration is re-established in the soil. Spontaneous Hg flux from soil to atmosphere is highly dependent on soil Hg concentrations (Agnan et al., 2016; Eckley

Table 2
Model calculations of the potential Hg remobilization by wildfire.

Code		Area [ha]	Remobilizable Hg [g]	Remobilizable Hg per area [g/ha]
Vegetation	Hotspot	433	205	0.50
	Entire map	18,418	1310	0.07
Topsoil	Hotspot	213	48,847	229.3
	Entire map	18,418	302,975	16.45

et al., 2016; Zhu et al., 2018). Using the linear regression relationship between Hg fluxes and substrate Hg concentrations determined by Agnan et al. (2016) and assuming the Hg concentration range in our experimental samples (up to 7.7 mg Hg/kg), the calculated Hg flux for the Tsumeb topsoil would be less than 65 ng/m^2/h. Assuming this Hg re-emission rate, the model calculation for our Hg-rich hotspot (213 ha) would give Hg emissions of less than 1.2 kg/y, which is significantly less compared to the potential wildfire-driven Hg remobilization (Table 2).

4. Conclusion

Polluted vegetation and topsoils near a Cu smelter in Tsumeb (semi-arid Namibia), where Hg-rich Cu concentrates are processed, are vulnerable to burning. Using the thermo-desorption experiments on the representative biomass-rich topsoils with a high Hg content (3.9–7.7 mg/kg), we simulated the temperature dependent release of Hg during wildfires. More than 91% of the Hg was released at ~340 °C, which corresponds to the predominant grassland-fire conditions. Despite the installation of efficient flue-gas cleaning technologies in the Tsumeb Cu smelter, the Hg legacy pool in the smelter surroundings will contribute to the Hg emissions until its complete burn-out during wildfires. Using the Hg spatial distribution data in the area (184 km^2), the estimates indicate that ~300 kg Hg can be remobilized by wildfire. Field measurements of the Hg fluxes (Eckley et al., 2016) and the application of Hg isotopic techniques (Wiederhold et al., 2013) would be useful tools for better understanding the individual processes linked to the wildfires and their role in Hg cycling near the active smelters in the semi-arid regions.

CRediT authorship contribution statement

Marek Tuhý: Conceptualization, Data curation, Formal analysis, Funding acquisition, Investigation, Methodology, Project administration, Visualization, Writing - original draft. **Jan Rohovec:** Conceptualization, Data curation, Formal analysis, Funding acquisition, Investigation, Methodology, Writing - review & editing. **Šárka Matoušková:** Data curation, Formal analysis, Writing - review & editing. **Martin Mihaljevič:** Data curation, Resources, Writing - review & editing. **Bohdan Kříbek:** Data curation, Resources, Writing - review & editing. **Ben Mapani:** Data curation, Formal analysis, Resources, Writing - review & editing. **Jörg Göttlicher:** Data curation, Formal analysis. **Ralph Steininger:** Data curation, Formal analysis. **Juraj Majzlan:** Data curation, Formal analysis, Writing - review & editing. **Vojtěch Ettler:** Conceptualization, Data curation, Formal analysis, Funding acquisition, Investigation, Methodology, Project administration, Resources, Supervision, Validation, Visualization, Writing - original draft.

Acknowledgements

This study was supported by the Czech Science Foundation (GAČR projects no. 19-18513S and 19-08614S) and a student grant attributed to Marek Tuhý from the Grant Agency of Charles University (GAUK 1598218). The Charles University team was partially supported by institutional funding from the Center for Geosphere Dynamics (UNCE/SCI/006). The research at the Institute of Geology ASCR was co-financed by the institutional support of RVO 67985831. Part of the equipment used for this study was purchased from the Operational Programme Prague – Competitiveness (Project CZ.2.16/3.1.00/21516). The kind support from Hans Nolte and Pierre Reinecke (Dundee Precious Metals Tsumeb, DPMT) was highly appreciated. We thank numerous colleagues for their support: Petr Drahota (XRD), Martin Racek (SEM, EPMA), Vít Penížek (soil sampling), Vladimír Majer (drawing plots in Surfer). A. Harvey Cook is thanked for his review of the English in the manuscript. The thorough reviews of two anonymous reviewers helped to significantly improve the original version of the manuscript.

Appendix A. Supplementary data

Supplementary data to this article can be found online at https://doi.org/10.1016/j.chemosphere.2020.125972.

References

Abraham, J., Dowling, K., Florentine, S., 2018a. Effects of prescribed fire and post-fire rainfall on mercury mobilization and subsequent contamination assessment in a legacy mine site in Victoria, Australia. Chemosphere 190, 144–153. https://doi.org/10.1016/j.chemosphere.2017.09.117.

Abraham, J., Dowling, K., Florentine, S., 2018b. Assessment of potentially toxic metal contamination in the soils of a legacy mine site in Central Victoria, Australia. Chemosphere 192, 122–132. https://doi.org/10.1016/j.chemosphere.2017.10.150.

Agnan, Y., Le Dantec, T., Moore, C.W., Edwards, G.C., 2016. New constraints on terrestrial surface-atmosphere fluxes of gasous elemental mercury using a global database. Environ. Sci. Technol. 50, 507–524. https://doi.org/10.1021/acs.est.5b04013.

Amap/Unep, 2013. Technical Background Report for the Global Mercury Assessment 2013. Arctic Monitoring and Assessment Programme. Norway/UNEP ChemicalsBranch, Oslo. Geneva, Switzerland.

Badía, D., López-García, S., Martí, C., Ortíz-Perpiñá, O., Girona-García, A., Casanova-Gascón, J., 2017. Burn effects on soil properties associated to heat transfer under contrasting moisture content. Sci. Total Environ. 601–602, 1119–1128. https://doi.org/10.1016/j.scitotenv.2017.05.254.

Ballirano, P., Botticelli, M., Maras, A., 2013. Thermal behavior of cinnabar, α-HgS, and the kinetics of the β-HgS (metacinnabar) → α-HgS conversion at room temperature. Eur. J. Mineral. 25, 957–965. https://doi.org/10.1127/0935-1221/2013/0025-2341.

Briggs, C., Gustin, M.S., 2013. Building upon the conceptual model for soil mercury flux: evidence of a link between moisture evaporation and Hg evasion. Water Air Soil Pollut. 224, 1744. https://doi.org/10.1007/s11270-013-1744-5.

Campos, I., Vale, C., Abrantes, N., Keizer, J.J., Pereira, P., 2015. Effects of wildfire on mercury mobilization in eucalypt and pine forest. Catena 131, 149–159. https://doi.org/10.1016/j.catena.2015.02.024.

Driscoll, C.T., Mason, R.P., Chan, H.M., Jacob, D.J., Pirrone, N., 2013. Mercury as a global pollutant: sources, pathways, and effects. Environ. Sci. Technol. 47, 4967–4983. https://doi.org/10.1021/es305071v.

Dundee Precious Metals Ltd. accessed July 10, 2019. https://www.dundeeprecious.com/English/Operating-Regions/Current-Operations/Tsumeb/Overview/default.aspx.

Eckley, C.S., Blanchard, P., McLennan, D., Mintz, R., Sekela, M., 2015. Soil-air mercury flux near a large industrial emission source before and after closure (Flin Flon, Manitoba, Canada). Environ. Sci. Technol. 49, 9750–9757. https://doi.org/10.1021/acs.est.5b01995.

Eckley, C.S., Tate, M.T., Lin, C.J., Gustin, M., Dent, S., Eagles-Smith, C., Lutz, M.A., Wickland, K.P., Wang, B., Gray, J.E., Edwards, G.C., Krabbenhoft, D.P., Smith, D.B., 2016. Surface-air mercury fluxes across Western North America: a synthesis of spatial trends and controlling variables. Sci. Total Environ. 568, 651–665. https://doi.org/10.1016/j.scitotenv.2016.02.121.

Engle, M.A., Gustin, M.S., Johnson, D.W., Murphy, J.F., Miller, W.W., Walker, R.F., Wright, J., Markee, M., 2006. Mercury distribution in two Sierran forest and one desert sagebrush steppe ecosystems and the effects of fire. Sci. Total Environ. 367, 222–233. https://doi.org/10.1016/j.scitotenv.2005.11.025.

Ettler, V., Rohovec, J., Navrátil, T., Mihaljevič, M., 2007. Mercury distribution in soil profiles polluted by lead smelting. Bull. Environ. Contam. Toxicol. 78, 12–16. https://doi.org/10.1007/s00128-007-9033-x.

Ettler, V., Johan, Z., Kříbek, B., Veselovský, F., Mihaljevič, M., Vaněk, A., Penížek, V., Majer, V., Sracek, O., Mapani, B., Kamona, F., Nyambe, I., 2016. Composition and fate of mine- and smelter-derived particles in soils of humid subtropical and hot semi-arid areas. Sci. Total Environ. 563, 329–339. https://doi.org/10.1016/j.scitotenv.2016.04.133.

Ettler, V., Cihlová, M., Jarošíková, A., Mihaljevič, M., Drahota, P., Kříbek, B., Vaněk, A., Penížek, V., Sráček, O., Klementová, M., Engel, Z., Kamona, F., Mapani, B., 2019. Oral bioaccessibility of metal(loid)s in dust materials from mining areas of northern Namibia. Environ. Int. 124, 205–2015. https://doi.org/10.1016/j.envint.2018.12.027.

Friedli, H.R., Radke, L.F., Lu, J.Y., 2001. Mercury in smoke from biomass fires. Geophys. Res. Lett. 28, 3223–3226. https://doi.org/10.1029/2000GL012704.

Friedli, H.R., Radke, L.F., Lu, J.Y., Banic, C.M., Leaitch, W.R., MacPherson, J.I., 2003. Mercury emissions from burning of biomass from temperate North American forests: laboratory and airborne measurements. Atmos. Environ. 37, 253–267. https://doi.org/10.1016/S1352-2310(02)00819-1.

Friedli, H.R., Radke, L.F., Payne, N.J., McRae, D.J., Lynham, T.J., Blake, T.W., 2007. Mercury in vegetation and organic soil at an upland boreal forest site in Prince Albert National Park, Saskatchewan, Canada. J. Geophys. Res. 112, G01004.

https://doi.org/10.1029/2005JG000061.
Friedli, H., Arellano, A., Cinnirella, S., Pirrone, N., 2009. Initial estimates of mercury emissions to the atmosphere from global biomass burning. Environ. Sci. Technol. 43, 3507–3513. https://doi.org/10.1021/es802703g.
Giesler, R., Clemmensen, K.E., Wardle, D.A., Klaminder, J., Binder, R., 2017. Boreal forests sequester large amounts of mercury over millennial time scales in the absence of wildfires. Environ. Sci. Technol. 51, 2621–2627. https://doi.org/10.1021/acs.est.6b06369.
Girona-García, A., Badía-Villas, D., Martí-Dalmau, C., Ortíz-Perpiñá, O., Mora, J.L., Armas-Herrera, C.M., 2018. Effects of prescribed fire for pasture management on soil organic matter and biological properties: a 1-year study case in the Central Pyrenees. Sci. Total Environ. 618, 1079–1087. https://doi.org/10.1016/j.scitotenv.2017.09.127.
Hojdová, M., Navrátil, T., Rohovec, J., Penížek, V., Grygar, T., 2009. Mercury distribution and speciation in soils affected by historic mercury mining. Water Air Soil Pollut. 200, 89–99. https://doi.org/10.1007/s11270-008-9895-5.
Hylander, L.D., Herbert, R.B., 2008. Global emission and production of mercury during the pyrometallurgical extraction of nonferrous sulfide ores. Environ. Sci. Technol. 42, 5971–5977. https://doi.org/10.1021/es800495g.
Jarošíková, A., Ettler, V., Mihaljevič, M., Kříbek, B., Mapani, B., 2017. The pH-dependent leaching behavior of slags from various stages of a copper smelting process: environmental implications. J. Environ. Manag. 187, 178–186. https://doi.org/10.1016/j.jenvman.2016.11.037.
Jarošíková, A., Ettler, V., Mihaljevič, M., Drahota, P., Culka, A., Racek, M., 2018. Characterization and pH-dependent environmental stability of arsenic trioxide-containing copper smelter flue dust. J. Environ. Manag. 209, 71–80. https://doi.org/10.1016/j.jenvman.2017.12.044.
Kim, C.S., Rytuba, J.J., Brown Jr., G.E., 2004. Geological and anthropogenic factors influencing mercury speciation in mine waste: an EXAFS spectroscopy study. Appl. Geochem. 19, 379–393. https://doi.org/10.1016/S0883-2927(03)00147-1.
Kříbek, B., Majer, V., Knésl, I., Keder, J., Mapani, B., Kamona, F., Mihaljevič, M., Ettler, V., Penížek, V., Vaněk, A., Šráček, O., 2016. Contamination of soil and grass in the Tsumeb smelter area, Namibia: modeling of contaminants dispersion and ground geochemical verification. Appl. Geochem. 64, 75–91. https://doi.org/10.1016/j.apgeochem.2015.07.006.
Lodenius, M., Tulisalo, E., Soltanpour-Gargari, A., 2003. Exchange of mercury between atmosphere and vegetation under contaminated conditions. Sci. Total Environ. 304, 169–174. https://doi.org/10.1016/S0048-9697(02)00566-1.
Millhollen, A.G., Gustin, M.S., Obrist, D., 2006. Foliar mercury accumulation and exchange for three tree species. Environ. Sci. Technol. 40, 6001–6006. https://doi.org/10.1021/es0609194.
Mudd, G.M., Jowitt, S.M., 2018. Growing global copper resources, reserves and production: discover is not the only control on supply. Econ. Geol. 113, 1235–1267. https://doi.org/10.5382/econgeo.2018.4590.
Navarro, A., 2008. Review of characteristics of mercury speciation and mobility from areas of mercury mining in semi-arid environments. Rev. Environ. Sci. Biotechnol. 7, 287–306. https://doi.org/10.1007/s11157-008-9139-6.
Navrátil, T., Hojdová, M., Rohovec, J., Penížek, V., Vařilová, Z., 2009. Effect of fire on pools of mercury in forest soil, central Europe. Bull. Environ. Contam. Toxicol. 83, 269–274. https://doi.org/10.1007/s00128-009-9705-9.
Neary, D.G., Klopatek, C.C., DeBano, L.F., Fjolliot, P.F., 1999. Fire effects on below ground sustainability: a review and synthesis. For. Ecol. Manage. 122, 51–71. https://doi.org/10.1016/S0378-1127(99)00032-8.
Pereira, P., Mataix-Solera, J., Úbeda, X., Rein, G., Cerdà, A., 2019. Fire Effects on Soil Properties. CSIRO Publishing, Clayton South.
Pirrone, N., Cinnirella, S., Feng, X., Finkelman, R.B., Friedli, H.R., Leaner, J., Mason, R., Mukherjee, A.B., Stracher, G.B., Streets, D.G., Telmer, K., 2010. Global mercury emissions to the atmosphere from anthropogenic and natural sources. Atmos. Chem. Phys. 10, 5951–5964. https://doi.org/10.5194/acp-10-5951-2010.
Podolský, F., Ettler, V., Šebek, O., Ježek, J., Mihaljevič, M., Kříbek, B., Šráček, O., Vaněk, A., Penížek, V., Majer, V., Mapani, B., Kamona, F., Nyambe, I., 2015. Mercury in soil profiles from metal mining and smelting areas in Namibia and Zambia: distribution and potential sources. J. Soils Sediments 15, 648–658. https://doi.org/10.1007/s11368-014-1035-9.
Reis, A.T., Coelho, J.P., Rucandio, I., Davidson, C.M., Duarte, A.C., Pereira, E., 2015. Thermo-desorption: a valid tool for mercury speciation in soils and sediments? Geoderma 237, 98–104. https://doi.org/10.1016/j.geoderma.2014.08.019.
Rumayor, M., Gallego, J.R., Rodríguez-Valdés, E., Díaz-Somoano, M., 2017. An assessment of the environmental fate of mercury species in highly polluted brownfields by means of thermal desorption. J. Hazard Mater. 325, 1–7. https://doi.org/10.1016/j.jhazmat.2016.11.068.
Ryan, K.C., 2002. Dynamic interactions between forest structure and fire behavior in boreal ecosystems. Silva Fenn. 36, 13–39. https://doi.org/10.14214/sf.548.
Safarzadeh, M.S., Moats, M.S., Miller, J.D., 2014. Recent trends in the processing of enargite concentrates. Miner. Process. Extr. Metall. Rev. 35, 283–367. https://doi.org/10.1080/08827508.2012.723651.
Schlesinger, M.E., King, M.J., Sole, K.C., Davenport, W.G., 2011. Extractive Metallurgy of Copper, fifth ed. Elsevier, Oxford, UK, p. 456.
Selin, N.E., 2009. Global biogeochemical cycling of mercury: a review. Annu. Rev. Environ. Resour. 34, 43–63. https://doi.org/10.1146/annurev.environ.051308.084314.
Smith-Downey, N.V., Sunderland, E.M., Jacob, D.J., 2010. Anthropogenic impacts on global storage and emissions of mercury from terrestrial soils: insights from a new global model. J. Geophys. Res. 115, G03008. https://doi.org/10.1029/2009JG001124.
Streets, D.G., Zhang, Q., Wu, Y., 2009. Projections of global mercury emissions in 2050. Environ. Sci. Technol. 43, 2983–2988. https://doi.org/10.1021/es802474j.
Webster, J.P., Kane, T.J., Obrist, D., Ryan, J.N., Aiken, G.R., 2016. Estimating mercury emissions resulting from wildfire in forests of the Western United States. Sci. Total Environ. 568, 578–586. https://doi.org/10.1016/j.scitotenv.2016.01.166.
Wiederhold, J.G., Smith, R.S., Siebner, H., Jew, A.D., Brown Jr., G.E., Bourdon, B., Kretzschmar, R., 2013. Mercury isotope signatures as tracers for Hg cycling at the New Idria Hg mine. Environ. Sci. Technol. 47, 6137–6145. https://doi.org/10.1021/es305245z.
Wiedinmeyer, C., Friedli, H., 2007. Mercury emission estimates from fires: an initial inventory for the United States. Environ. Sci. Technol. 41, 8092–8098. https://doi.org/10.1021/es071289o.
Wu, Q., Wang, S., Zhang, L., Hui, M., Wang, F., Hao, J., 2016. Flow analysis of the mercury associated with nonferrous ore concentrates: implications on mercury emissions and recovery in China 2016. Environ. Sci. Technol. 50, 1796–1803. https://doi.org/10.1021/acs.est.5b04934.
Wu, Q., Wang, S., Wang, L., Liu, F., Lin, C.J., Zhang, L., Wang, F., 2014. Spatial distribution and accumulation of Hg in soil surrounding a Zn/Pb smelter. Sci. Total Environ. 496, 668–677. https://doi.org/10.1016/j.scitotenv.2014.02.067.
Yin, X., Yao, C., Song, J., Li, Z., Zhang, C., Qian, W., Bi, D., Li, C., Teng, Y., Wu, L., Wan, H., Luo, Y., 2009. Mercury contamination in vicinity of secondary copper smelters in Fuyang, Zhejiang Province, China: levels and contamination in topsoils. Environ. Pollut. 157, 1787–1793. https://doi.org/10.1016/j.envpol.2009.02.018.
Zhu, W., Lin, C.J., Wang, X., Sommar, J., Fu, X., Feng, X., 2016. Global observations and modelling of atmosphere-surface exchange of elemental mercury: a critical review. Atmos. Chem. Phys. 16, 4451–4480. https://doi.org/10.5194/acp-16-4451-2016.
Zhu, W., Li, Z., Li, P., Yu, B., Lin, C.J., Sommar, J., Feng, X., 2018. Re-emission of legacy mercury from soil adjacent to closed point sources of Hg emission. Environ. Pollut. 242, 718–727. https://doi.org/10.1016/j.envpol.2018.07.002.

III

Tuhý, M., Ettler, V., Rohovec, J., Matoušková, Š., Mihaljevič, M., Kříbek, B., Mapani, B., 2021. Metal(loid)s remobilization and mineralogical transformations in smelter-polluted savanna soils under simulated wildfire conditions. *Journal of Environmental Management* 293: 112899. https://doi.org/10.1016/j.jenvman.2021.112899

Journal of Environmental Management 293 (2021) 112899

Contents lists available at ScienceDirect

Journal of Environmental Management

journal homepage: www.elsevier.com/locate/jenvman

Metal(loid)s remobilization and mineralogical transformations in smelter-polluted savanna soils under simulated wildfire conditions

Marek Tuhý [a,**], Vojtěch Ettler [a,*], Jan Rohovec [b], Šárka Matoušková [b], Martin Mihaljevič [a], Bohdan Kříbek [c], Ben Mapani [d]

[a] Institute of Geochemistry, Mineralogy and Mineral Resources, Faculty of Science, Charles University, Albertov 6, 128 00, Prague 2, Czech Republic
[b] Institute of Geology, Academy of Sciences of the Czech Republic, Rozvojová 269, 165 00, Prague 6, Czech Republic
[c] Czech Geological Survey, Geologická 6, 152 00, Prague 5, Czech Republic
[d] Department of Mining and Process Engineering, Faculty of Engineering, Namibia University of Science and Technology, Private Bag, 13388, Windhoek, Namibia

ARTICLE INFO

Keywords:
Wildfire
Soil
Metal(loid)s
Remobilization
Smelter pollution

ABSTRACT

The surroundings of mines and smelters may be exposed to wildfires, especially in semi-arid areas. The temperature-dependent releases of metal(loid)s (As, Cd, Cu, Pb, Zn) from biomass-rich savanna soils collected near a Cu smelter in Namibia have been studied under simulated wildfire conditions. Laboratory single-step combustion experiments (250–850 °C) and experiments with a continuous temperature increase (25–750 °C) were coupled with mineralogical investigations of the soils, ashes, and aerosols. Metals (Cd, Cu, Pb, Zn) were released at >550–600 °C, mostly at the highest temperatures, where complex aerosol particles, predominantly composed of slag-like aggregates, formed. In contrast, As exhibited several emission peaks at ~275 °C, ~370–410 °C, and ~580 °C, reflecting its complex speciation in the solid phase and indicating its remobilization, even during wildfires with moderate soil heating. At <500 °C, As was successively released via the transformation of As-bearing hydrous ferric oxides, arsenolite (As_2O_3) grains attached to the organic matter fragments, metal arsenates, and/or As-bearing apatite, followed by the thermal decomposition of enargite (Cu_3AsS_4) at >500 °C. The results indicate that the active and abandoned mining and smelting sites, especially those highly enriched in As, should be protected against wildfires, which can be responsible for substantial As re-emissions.

1. Introduction

Wildfire activity has increased in numerous places on Earth partially as a result of climate change among other factors (Westerling et al., 2006; Gross et al., 2020; Kganyago and Shikwambana, 2020; Weber and Yadav, 2020; Witze, 2020). Wildfires cause atmospheric pollution, contribute to the long-range transport of aerosols (Creamean et al., 2016) and have direct effects on human health (Weinhold, 2011), soil properties (Campos et al., 2016; Pereira et al., 2019), land erosion and the subsequent contamination of watersheds (Bladon et al., 2014; Cerrato et al., 2016; Abraham et al., 2017; Rahman et al., 2018). Since the last decade, the environmental effects of wildfires have attracted the attention of many scientists and resulted in the publication of focused special issues of scientific journals (Muñoz-Rojas and Pereira, 2020 and references therein) and books (Pereira et al., 2019).

Compared to the above-mentioned environmental impacts, the processes related to wildfire-driven emissions of trace elements have been studied less, although Nriagu (1989) estimated that the global emissions of metal(loid) contaminants from wildfires and biomass burning average 1900 t Pb, 7600 t Zn, 3800 t Cu, 190 t As and 110 t Cd per year. Laboratory and field experiments demonstrated that Hg is especially easily mobilized even by moderate fires, when the soil and biomass are heated to temperatures around 350 °C (Wiedinmeyer and Friedli, 2007; Friedli et al., 2009; Campos et al., 2015; Abraham et al., 2018a; Howard et al., 2019; Tuhý et al., 2020a). Aerosols from biomass burning have been found to contain many trace metallic elements, including Cu, Zn, Pb, and Cd, as demonstrated by studies from the African savanna (Gaudichet et al., 1995), Australia (Isley and Taylor, 2020), the USA (Jahn et al., 2021) and Asia (Kayee et al., 2020), where wildfires are quite frequent. Many studies confirmed that the emitted metals could be transported hundreds of kilometers from the fire (Young and Jan 1977; Creamean et al., 2016).

* Corresponding author.
** Corresponding author.
E-mail addresses: marek.tuhy@natur.cuni.cz (M. Tuhý), ettler@natur.cuni.cz (V. Ettler).

https://doi.org/10.1016/j.jenvman.2021.112899
Received 15 March 2021; Received in revised form 6 May 2021; Accepted 24 May 2021
Available online 2 June 2021

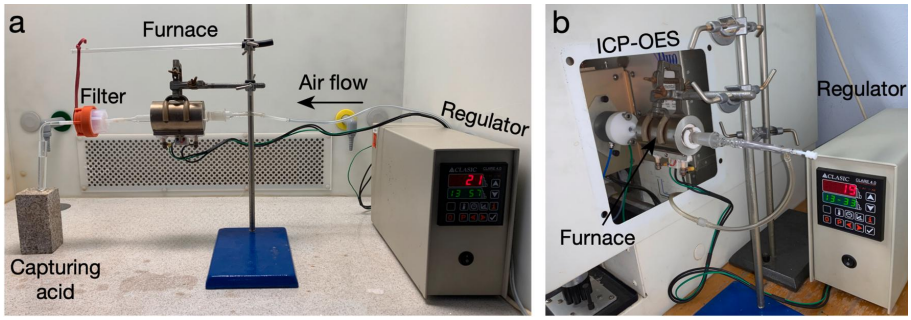

Fig. 1. Laboratory wildfire simulation experimental setups. a) Single-step combustion setup consisting of a temperature regulated resistance furnace and an air supply, with a PTFE filter assembly at the outlet, and a glass pipette for bubbling the outlet gas into the vial containing 5% (v/v) HNO_3; b) Setup with a continuous temperature increase and online detection consisting of the same regulated furnace connected directly to the ICP-OES operating under an Ar flow.

Table 1
Chemical and mineralogical compositions of the biomass-rich topsoils and industrial waste samples.

Bulk chemistry	As	Cd	Cu	Fe	Pb	Zn	C_{org}	C_{inorg}	S_{tot}
	mg kg^{-1}						%		
Experimental topsoil samples[a]									
A	2070 ± 42.9	74.7 ± 2.81	7090 ± 184	34,400 ± 166	4820 ± 99.5	3480 ± 82.6	14.9 ± 0.04	2.67 ± 0.02	0.55 ± 0.01
AM	1870 ± 54	55.0 ± 1.68	5610 ± 133	30,200 ± 542	3340 ± 82.9	2530 ± 72.1	20.7 ± 0.10	1.97 ± 0.02	0.61 ± 0.01
G	1180 ± 44.2	55.1 ± 2.11	4920 ± 180	27,300 ± 1120	3450 ± 132	2450 ± 86	12.7 ± 0.16	2.49 ± 0.11	0.26 ± 0.01
Industrial waste samples									
Mine tailing dust[b]	3190	126	6530	5063	5810	5320	1.27	6.54	0.10
Smelter slag dust[b]	3800	50	6680	250,000	22,300	48,500	0.07	<0.01	0.53
Smelter flue dust[c]	533,000	715	10,700	20,200	34,100	14,100	4.15	<0.01	3.00

Mineralogy	Phase composition (XRD)	Additional phases detected by SEM/EPMA
Experimental topsoil samples[b]		
A	Qtz, Ms, Kfs, Cal, Dol, Mag	Gl, HFO, sulfides/sulfosalts, carbonates, arsenates, Ap
AM	Qtz, Ms, Kfs, Cal, Dol, Mag	HFO, Ap, Rt, Gl, carbonates, sulfides/sulfosalts, arsenates, vanadates
G	Qtz, Ms, Kfs, Cal, Dol, Mag	Gl, HFO, sulfides/sulfosalts, carbonates, arsenates, Ap
Industrial waste samples		
Mine tailing dust[c]	Dol, Ms, Qtz, Cal	Con, Duf, Gn, Sm, Wil, Cu sulfides
Smelter slag dust[c,d]	Gl, Spl, Ol, Cpx, Qtz	Cu sulfides
Smelter flue dust[e]	Asl, Cla, Gp, Qtz, Cv, Gn	Ang, Sp, various arsenates

Abbreviations: Ang – anglesite ($PbSO_4$), Ap – apatite [$Ca_5(PO_4)_3(OH,F,Cl)$], Asl – arsenolite (As_2O_3), Cal – calcite ($CaCO_3$), Cla – claudetite (As_2O_3), Con – conichalcite [$CaCu(AsO_4)(OH)$], Cpx – clinopyroxene, of hedenbergite composition ($CaFeSi_2O_6$), Cv – covellite (CuS), Dol – dolomite [$CaMg(CO_3)_2$], Duf – duftite [$PbCu(AsO_4)(OH)$], Gl – slag glass, Gn – galena (PbS), Gp – gypsum ($CaSO_4{\cdot}2H_2O$), HFO – hydrous ferric oxides, Kfs – K-feldspar ($KAlSi_3O_8$), Mag – magnetite (Fe_3O_4), Ms – muscovite [$KAl_2(Si_3Al)O_{10}(OH,F)_2$], Ol – olivine, mainly of fayalite (Fe_2SiO_4) composition, Qtz –quartz (SiO_2), Rt – rutile (TiO_2), Sm – smithsonite ($ZnCO_3$), Sp – sphalerite (ZnS), Spl – spinel [$(Fe^{2+},Mg,Zn)(Fe^{3+},Al,Cr)_2O_4$], Wi – willemite ($Zn_2SiO_4$).

[a] Collected under the acacia trees (A), acacia and marula trees (AM) and in a grassland (G); mean ± standard deviation.
[b] Data from Tuhý et al. (2020b).
[c] Data from Ettler et al. (2019).
[d] Data from Jarošíková et al. (2017).
[e] Data from Jarošíková et al. (2018).

Soils contaminated by human activities appear to contribute to trace metal remobilization by wildfires. For example, Pb isotopic investigations of the ash from wildfires in the USA and Australia showed that the ash contained industrial Pb from gasoline combustion (Odigie and Flegal, 2011, 2014; Kristensen and Taylor, 2014; Wu et al., 2017). Other studies from Australia compared the Pb isotopic compositions of aerosols before, during, and after the wildfire periods; the authors found that the interpretation of the Pb isotopic patterns is not straightforward, but the contribution of remobilized anthropogenic Pb seems to occur (Kristensen et al., 2017; Isley and Taylor, 2020).

There is a particularly high risk of contaminant remobilization back into the atmosphere in highly polluted semi-arid areas in the vicinity of abandoned or active mines and smelters (Abraham et al., 2018a,b). Particulates emitted by mining and smelting industries or windblown from waste disposal sites have very complex chemical and mineralogical compositions; they adhere to the surfaces of vegetation, are deposited onto the soil surface as leaf litter, and are incorporated into the topsoil organic matter (Kříbek et al., 2016; Ettler et al., 2016; Tuhý et al., 2020b), where they become vulnerable to transformations during the wildfire-induced heating. It is important to stress that wildfires underneath the tree canopies cause greater soil heating due to the wood fuel presence (Pereira et al., 2019). Several studies from Cu mining areas in Zambia hypothesized that this phenomenon could be responsible for the greater re-emission of metals from contaminated wooded savanna than from grassland sites (Mihaljevič et al., 2011; Ettler et al., 2014).

However, the mechanisms and processes controlling the remobilization of metal(loid) contaminants from the burned soil and biomass remain poorly understood. To help to fill this knowledge gap, this

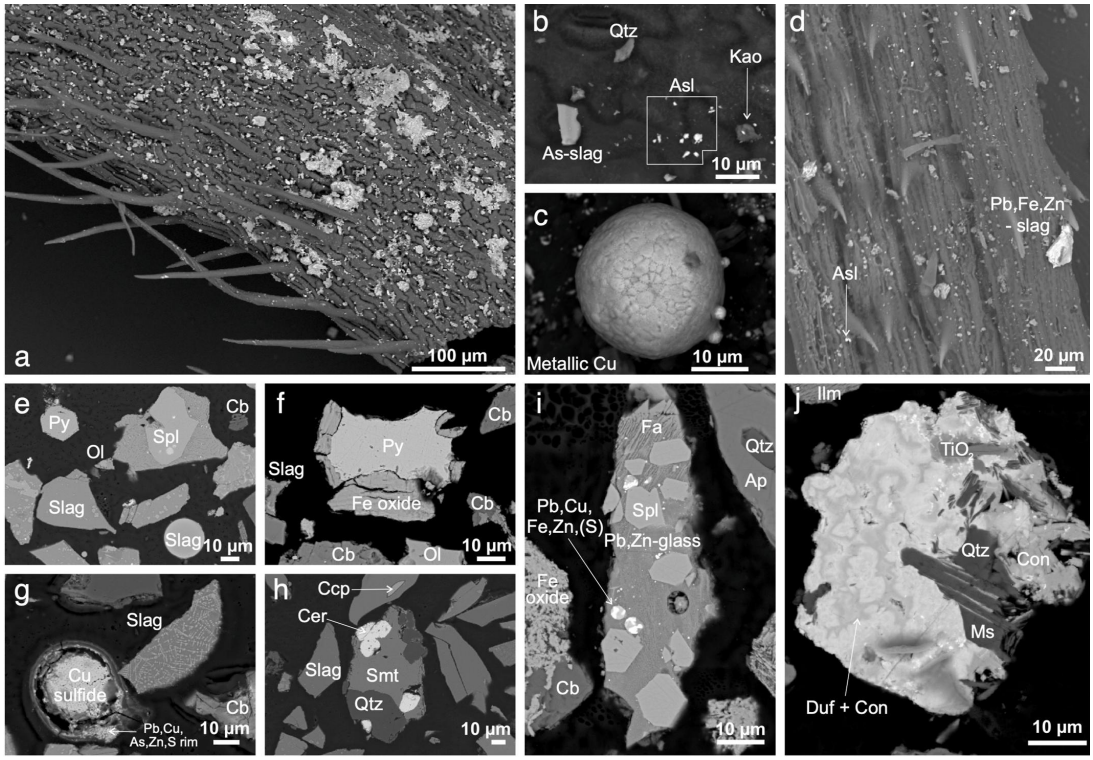

Fig. 2. FEG-SEM micrographs in back-scattered electrons (BSE) of the metal(loid)-bearing particles adhering to the surfaces of the biomass fragments from the topsoils (a–d) and in the heavy mineral fraction of the topsoils. a) Plant fragment covered with the windblown dust particles; b) Geogenic (quartz, kaolinite) and smelter-derived particles (As-slag, arsenolite) attached to the vegetation surface; c) Smelter-emitted spherical Cu metal particle; d) Fragment of grass with attached arsenolite and metal-bearing slag particles; e) Euhedral pyrite and carbonate grains associated with various slag particles, f) Pyrite grain with a weathering rim composed of Fe (oxyhydr)oxide, olivine from slag, glassy slag fragments and carbonates; g) Slag particle, carbonate grain and weathered spherical particle composed of primary Cu sulfide and a Pb, Cu, As, Zn, S-rich rim; h) Slag fragments with chalcopyrite inclusion and a complex particle composed of cerussite, smithsonite and quartz; i) Carbonate, Fe oxides, quartz and apatite surrounding a slag particle composed of fayalite crystals, spinels and intermetallic droplets embedded in a metal-rich glassy matrix; j) Geogenic aggregate of duftite and conichalcite intergrown with quartz, muscovite and an unspecified TiO_2 mineral; Abbreviations: Ap - apatite [$Ca_5(PO_4)_3(F,Cl,OH)$], Asl – arsenolite (As_2O_3), Cb – carbonate (variable composition), Ccp – chalcopyrite ($CuFeS_2$), Cer – cerussite ($PbCO_3$), Con – conichalcite [$CaCu(AsO_4)(OH)$], Duf – duftite [$PbCu(AsO_4)(OH)$], Gn – galena (PbS), Ilm – ilmenite ($FeTiO_3$), Kao – kaolinite [$Al_2Si_2O_5(OH)_4$], Ms – muscovite [$KAl_2(AlSi_3O_{10})(OH)_2$], Ol – olivine [$(Mg,Fe)_2(SiO_4)$], Py – pyrite ($FeS_2$), Qtz – quartz ($SiO_2$), Smt – smithsonite ($ZnCO_3$), Spl – spinel (variable composition).

paper's main objective is to investigate the release of metal(loid)s from highly polluted biomass-rich savanna topsoils collected near mines and smelters located in semi-arid Namibia under simulated wildfire conditions. Many previous laboratory wildfire-simulation studies focusing on soil heating have been conducted in muffle furnaces (e.g., Johnston et al., 2019), but this technique has many limitations, such as the lack of oxygen circulation and the impossibility of aerosol sampling (Pereira et al., 2019 and references therein). For this reason, we used a novel setup of laboratory burning experiments and combined them with comprehensive chemical and multi-method mineralogical investigations of the initial materials, ashes, and aerosols. This approach enabled one to estimate the fluxes of the metals (Cd, Cu, Pb, Zn) and the metalloid (As), which were the main potentially toxic elements in the studied topsoils, and to describe the related mineralogical transformations over a broad temperature range corresponding to conditions extending from low to high-intensity wildfires (250–850 °C).

2. Materials and methods

2.1. Field sampling and experimental samples preparation

The experimental biomass-rich topsoil samples were collected in July 2013 immediately adjacent to the Tsumeb Cu smelter and waste disposal area (Namibia; 19°15′S, 17°42′E) on the lee side of prevailing winds (Figure S1 in the Supplementary Material). Our previous investigations reported high levels of contaminants bound in the uppermost soil horizons (Mihaljevič et al., 2015; Ettler et al., 2016; Kříbek et al., 2016). It is known that wildfires mainly affect the uppermost centimeters in the soil profile (Badía et al., 2017; Girona-García et al., 2018). Therefore, to perform the wildfire-simulating experiments, only the upper topsoils (litter/grass fragments included; 0–1 cm depth) were collected. The samples were representative of the topsoils developed under the most common vegetation cover in the area surrounding the smelter complex: *Acacia* sp. [A], *Acacia* sp. and marula (*Sclerocarya birrea*) [AM], and grass (*Aristida stipitata*) [G]. The vegetation cover has an influence on the organic matter content in the topsoil and litter.

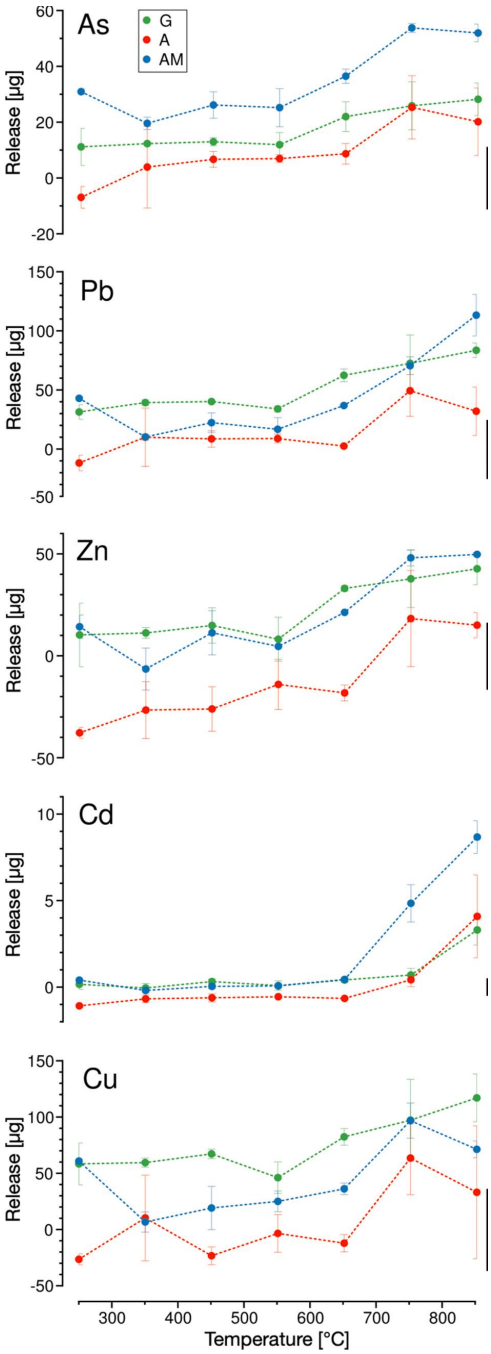

Fig. 3. Amounts of the metal(loid)s released from the heated experimental topsoils (in µg; initial sample mass: 0.2 g) as a function of the temperature as obtained by the single-step combustion setup. The trend lines were drawn to guide the eyes. No release corresponds to zero baselines, which represent the amount of element in an unburned sample (the black line on the right side of each graph shows the maximum standard deviations calculated from the sample digestions replicates). Positive values correspond to a release, and negative values and their standard deviations correspond to an accumulation of a given element. The experimental topsoil samples were collected under the acacia trees (A), acacia and marula trees (AM) and in a grassland (G).

Under the shrubs and trees, the topsoils contain wood debris, which, as a fuel, can generate different conditions when affected by wildfires compared to the biomass fragments in grassland plots (Pereira et al., 2019).

The topsoil samples were firstly disaggregated in a cutting machine (Fritsch Pulverisette 14, Germany) and sieved to <2 mm (Retsch, Germany). The heavy mineral fractions were separated using a heavy liquid (1,1,2,2-tetrabromethane), centrifuged (Janetzki S70D, Germany) for 30 min at 1800 rpm, and prepared as polished sections for the electron microscope observations of the metalloid-hosting phases. In addition, specimens of the vegetation fragments (wood, leaves, twigs) collected from each sample were investigated under an optical microscope, then attached to a carbon tape, carbon-coated, and prepared for electron microscopy. To obtain the experimental topsoil samples for the bulk chemical composition determinations and wildfire-simulating experiments, the <2 mm-sieved topsoil aliquots were milled in an agate mill (Fritsch Pulverisette, Germany) to ensure homogeneity.

Moreover, three industrial waste dust samples originating from the mining and smelting circuit in the Tsumeb smelter area were also collected to obtain representative examples of dust materials, which can be windblown from the smelter and waste disposal sites and can adhere to vegetation surfaces and be deposited into the soils: mine tailing dust, granulated slag dust, flue dust from air-pollution-control systems in the smelter (Ettler et al., 2009; Jarošíková et al., 2017, 2018; Ettler et al., 2019).

2.2. Soil chemical analyses

To obtain the bulk concentrations of the metal(loid)s in the experimental topsoils, the samples were acid-digested in a closed system without preliminary ashing to eliminate the investigated elements' potential losses. The sample aliquots (0.2 g) were placed into polytetrafluoroethylene (PTFE) digestion vessels (Savillex®, USA), and 8 mL of HNO_3 (65%), 30 µL of H_2O_2 (30%), and 30 µL of HF (40%) were added. Afterward, the digestion vessels were closed and tempered on a hot plate at 300 °C for 8 h. Both the liquid and solid residuals were carefully transferred to a centrifuge vessel using deionized water (DIW; MilliQ, Millipore, USA). This solution was centrifuged (Hettich UNIVERSAL 320 R, Germany) for 5 min at 4000 rpm. The obtained liquids were transferred into 50 mL volumetric flasks and diluted accordingly (subsample #1). The residual solids were transferred into PTFE digestion vessels (Savillex, USA) using DIW, which was then slowly evaporated. In the next step, 10 mL of HF (40%) and 0.5 mL $HClO_4$ (70%) were added to the residue in the open PTFE vessel, and the mixture was heated to 150 °C and slowly evaporated to near dryness. Subsequently, the samples were dissolved in concentrated HNO_3 and diluted to 50 mL (5% HNO_3) (subsample #2). The obtained digests were analyzed by a combination of inductively coupled plasma optical emission spectrometry (ICP-OES, Agilent 5110 SVDV, USA) and inductively coupled plasma mass spectrometry (ICP-MS, ThermoScientific iCAP™, Germany). The total metal(loid)s concentrations in the original samples were calculated by combining the values found in subsamples #1 and #2. The accuracy of the digestion and analytical procedures (QC/QA) was checked by a combination of the NIST 1515 (Apple Leaves), NIST 1573a (Tomato Leaves), Metranal3™ (Strawberry Leaves), NIST 2711a (Montana Soil

Table 2
Key metal(loid)-hosting phases in the experimental topsoils (adapted from Tuhý et al., 2020b). Note: It was not possible to quantify the Cd deportment in the individual samples, but according to the EPMA analyses, the Cd was mainly bound in arsenates, sulfides, slag glass and carbonates. For the phase compositions and abbreviations, see Fig. 1 and Table 1.

Element	Sample	Phase
As	A	apatite, slag glass, arsenates
	AM	slag glass, HFO, duftite
	G	apatite, arsenates, duftite
Cu	A	sulfides, azurite/malachite, slag glass
	AM	azurite/malachite, sulfides, mottramite
	G	sulfides, sulfosalts, azurite/malachite
Pb	A	slag glass, HFO, cerussite
	AM	cerussite, mottramite, slag glass
	G	slag glass, HFO, sulfides
Zn	A	slag glass, HFO, smithsonite
	AM	HFO, slag glass, calcite, dolomite
	G	slag glass, HFO, smithsonite

2), CCU-1e (Copper Concentrate) and CZN-4 (Zinc Concentrate) certified reference materials and was found to be satisfactory (Table S1). The organic carbon (C_{org}), inorganic carbon (C_{inorg}), and total sulfur (S_{tot}) were determined using a combination of the ELTRA CS 530 and CS 500 TIC analyzers (ELTRA, Germany) (the QC/QA results are available in Tuhý et al., 2020a).

2.3. Mineralogical analyses

The X-ray diffraction analysis (XRD) of the solid samples (topsoils, site-specific industrial waste samples) was performed by a PANalytical X'Pert Pro diffractometer (PANalytical, the Netherlands) equipped with an X'Celerator detector operating in the Bragg-Brentano geometry using CuK_α radiation (0.15418 nm) at 40 kV and 30 mA over a range 2–80° 2theta (step 0.02°, counting time 150 s per step). The diffractograms were analyzed in the X'Pert HighScore Plus 3.0 software coupled with the Crystallography Open Database (COD). The biomass and soil heavy mineral fractions were investigated under an optical microscope (Leica DM LP, Germany) and an electron probe microanalyzer (EPMA; JEOL JXA-8530F, Japan) equipped with a field emission gun electron source (FEG), detectors for the scanning electron microscopy (SEM) imaging, energy dispersion spectrometry (EDS; JEOL JED-2300F, Japan) and five wave dispersion spectrometers (WDS) for the qualitative and quantitative analyses. Details about the EPMA analytical conditions, standards, and detection limits are given elsewhere (Tuhý et al., 2020b).

2.4. Laboratory wildfire simulations

Many laboratory experiments investigating the thermal stability of soils to simulate wildfire conditions have been conducted in simple muffle furnaces (e.g., Johnston et al., 2016; Johnston et al., 2018; Johnston et al., 2019). However, such a device does not provide sufficient oxygen circulation, which is typical for real wildfires (Pereira et al., 2019). Therefore, we introduced novel experimental setups to better simulate the potential wildfire effects on the topsoils under laboratory conditions. We used a single-step combustion experiment to measure emissions at fixed temperatures (250–850 °C) covering a range of potential soil heating levels during wildfires, and a continuous temperature increase experiment to characterize constituents according to their thermal stability. We focused only on As, Cd, Cu, Pb, and Zn, which were the main contaminants released by the mines and smelters in the studied area (processing of Cu–Pb ores with substantial amounts of As, Cd and Zn), and which were found in the studied topsoils in the highest concentrations.

2.4.1. Single-step combustion setup

The apparatus used for the single-step combustion is shown in Fig. 1a. The device was designed to simulate wildfire conditions for a range of potential soil temperatures by the precise temperature setting, continuous delivery of fresh air coupled with both a smoke outcome and the possibility of sampling the ash and aerosols. During the burning procedure, a mass of 0.2 g of the homogenized topsoil sample was placed in a corundum boat and heated for 25 min in a pre-heated resistance furnace (Clasic CZ, Czech Republic) equipped with a quartz tube. A CLARE 4.0 programmable regulator (Clasic CZ, Czech Republic) connected to a K-type (NiCr–Ni) thermocouple controlled the furnace's temperature. The burning experiments were conducted under synthetic air in order to closely simulate wildfire conditions and to ensure the repeatability of the experiment; the air supply (ca. 50 mL min^{-1}) was controlled by an analog gas flow meter (IN-ECO, Slovakia) with an adjustable flow. For the selected runs, a PTFE filter assembly (porosity 1–2 μm, diameter 47 mm; both produced by Savillex®, USA) was placed at the outlet of the burning chamber (Fig. 1a) to trap the aerosol particles for the additional mineralogical investigations. The final part of the setup consisted of a glass pipette for bubbling the outlet gas in the trapping solution (5% HNO_3) (Fig. 1a). The experimental sample combustions were performed at the following temperatures to cover a temperature range occurring during wildfires: 250, 350, 450, 550, 650, 750, and 850 °C (Ryan, 2002; Pereira et al., 2019). Including the setup adjustment and validation, a total of 110 burning experiments were performed. All the experiments were used for the mass loss determination and homogeneity testing, and 42 of them (2 replicates per each temperature step for each of the 3 experimental topsoils) were used for the contaminant release determinations. The obtained ashes (digested and analyzed using the same procedure as the original soils, see above), trapping solutions, and solutions obtained by washing the setup components (quartz tube and glass pipette; heated concentrated HNO_3) were all analyzed. For the metal(loid)s mass balance calculations, the chemical compositions of the original soil and the obtained ash were used. Moreover, mineralogical methods were used to investigate the ashes (XRD, FEG-SEM) and the aerosol particles trapped by the filtering unit (FEG-SEM).

2.4.2. Setup with continuous temperature increase and online ICP-OES detection

An experimental setup with a continuous temperature increase and direct detection (called "thermo-desorption") has often been used to understand the thermal stability of volatile elements such as Hg (Tuhý et al., 2020a). We assume it can also be used as a proxy method for speciation purposes for other elements affected by burning.

The apparatus consisted of the combustion unit similar to the setup specified in section 2.4.1 (without the filter assembly) directly connected to the quartz injector of the ICP-OES plasma torch (at a distance of 5.5 cm). An Iris Intrepid II XSP ICP-OES instrument (Thermo-Scientific, USA) operating in the axial plasma mode was used as a detector (Fig. 1b). The sample was gradually heated from 25 °C up to 750 °C for 14 min 30 s, applying a linear slope of 50 °C min^{-1}. The combustion products were directly introduced into the ICP-OES plasma employing an Ar stream (50 mL min^{-1}), and the selected elements of interest (As, Pb, Zn, S) were continuously and simultaneously detected (at the analytical lines of 189.0 nm, 220.3 nm, 213.8 nm, and 182.0 nm, respectively). In the used temperature range, it was impossible to observe the Cu (324.7 nm) and Cd (226.5 nm) signals. In the case of Cu, the released amount of this poorly volatile element was probably too low, while the most sensitive wavelength of Cd (228.8 nm) was unusable due to the heavy interference with the highly abundant As. This experiment has been performed for topsoils under each of the three common vegetation types, and, due to comparison purposes, for the site-specific industrial waste dust samples in order to depict the role of solid speciation of the metal(loid)s on their temperature-induced release.

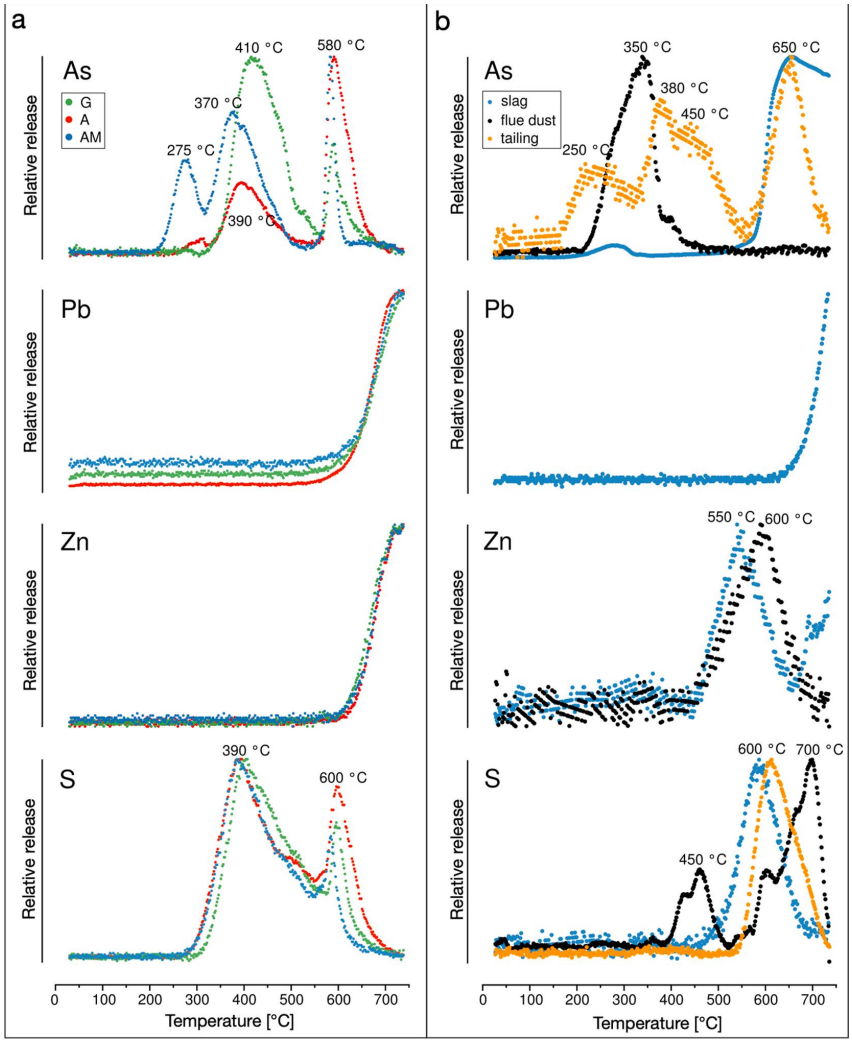

Fig. 4. Relative release of the selected metal(loid)s and sulfur as obtained by the wildfire-simulating setup with a continuous temperature increase and online measurement. a) Temperature-dependent release from the experimental topsoils collected under the acacia trees (A), acacia and marula trees (AM) and in a grassland (G); b) Temperature-dependent release from heated industrial waste samples (slag, flue dust, tailing).

3. Results

3.1. Chemical and mineralogical compositions of soils and industrial waste samples

The experimental soils exhibited similarly high concentrations of metal(loid)s with the highest values in sample A (up to 2070 mg As kg^{-1}, 7090 mg Cu kg^{-1}, 4820 mg Pb kg^{-1}, 3480 mg Zn kg^{-1}) (Table 1). The Cd concentrations were significantly lower compared to the other contaminants (55–75 mg kg^{-1}). The bulk mineralogy (XRD) of the three experimental topsoil samples was similar, with a dominant content of quartz, muscovite, K-feldspar, carbonates (calcite, dolomite), and magnetite. The samples differed in the proportion of minor metal(loid)-hosting phases detected by the SEM and EPMA (Tuhý et al., 2020b) (Table 1). The vegetation fragments (leaves, twigs) found in the topsoils were covered with fragments of geogenic phases (quartz, clay minerals, carbonates) as well as particles of anthropogenic origin (windblown slag fragments, smelter emissions-derived arsenolite [As_2O_3] and rounded particulates of sulfides/metallic phases) (Fig. 2a–d). A large proportion of the phases originating from the mine tailings, slag disposal sites, and smelter emissions were also found in the heavy mineral fractions separated from the experimental topsoils (Fig. 2e–j) (also see the data in Tuhý et al., 2020b).

The industrial waste samples, representing dominant local sources of soil pollution, were also rich in metal(loid) contaminants. The smelter flue dust showed much higher concentrations of As (533,000 mg kg^{-1}), Cd (715 mg kg^{-1}), Cu (10,700 mg kg^{-1}), and Pb (34,100 mg kg^{-1}) when compared with the mine tailing and slag dusts. The latter had similar

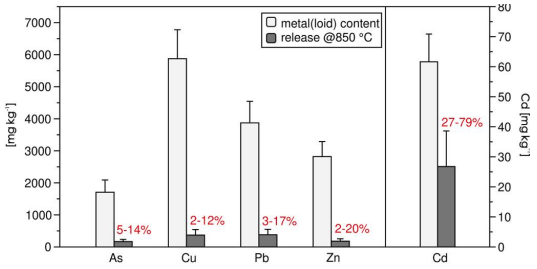

Fig. 5. Potential metal(loid) releases at 850 °C as compared with the concentrations in the original topsoil samples.

concentration levels of As (3190–3800 mg kg^{-1}) and Cu (6530–6680 mg kg^{-1}), but higher Pb and Zn concentrations were found for the smelter slag dust (22,300 and 48,500 mg kg^{-1}, respectively) (Table 1). The mineralogical composition of these waste materials is rather complex as revealed by previous studies (Table 1) (Ettler et al., 2009; Jarošíková et al., 2017, 2018; Ettler et al., 2019).

3.2. Temperature-dependent soil transformation and metal(loid) release

The single-step combustion experiment indicated that the topsoil weight loss increased with the temperature (up to 34.3–52.9% at 850 °C) and correlated with the C_{org} content in the samples (AM>A>G) (Figure S2). Small standard deviations indicated an excellent experimental reproducibility considering highly heterogeneous compositions and the comparatively low amount of the experimental samples (0.2 g) used in the combustion experiments (Figure S2). No significant changes in the bulk mineralogical compositions (XRD) were observed as a function of temperature, except for the ash residue obtained at 850 °C, where dolomite and partly calcite disappear and transform to portlandite (CaO) (major reflections at the *d* values of 0.490 and 0.262 nm), and hematite (Fe_2O_3) starts to be detected (major reflections at the *d* values of 0.269 and 0.252 nm) (Figure S3). The trends in the metal (loid) releases (Fig. 3) from the burned experimental samples were, thus, related to the mineralogical transformations and thermal stabilities of the minor phases (Tables 1 and 2).

A substantial release of metal(loid)s was observed at >550 °C, but the absolute values varied between the individual samples, likely due to the differences in their solid speciation (Fig. 3, Table 2). Samples A and AM, collected under the trees, exhibited small or no releases of metals at <550 °C (i.e., the amounts released were mostly within the standard deviation of the bulk concentration in the original sample). However, compared to the metals, the temperature-dependent release was different for As, which, in the case of samples AM and G, was substantially released even in the lowest temperature range 250–550 °C (Fig. 3).

Part of the released metal(loid)s may be trapped by the experimental setup components (tars deposited into the quartz tube, filtering unit, glass pipette, and particulates trapped on the filters). The amount of trapped As increased as a function of temperature and attained 12.1–29.4% of the total released As at 850 °C (Figure S4). In contrast, the metals were less trapped, and their capture increased only at >750 °C (Figure S4). The SEM observations of the aerosols collected on the filters at 850 °C indicated that the metal(loid)-bearing spherical slag particles, residual ore mineral grains, and complex aggregates composed of submicrometric grains of glassy slag particles enriched in metal(loid)s were emitted during the combustion at high temperature (Figure S5).

During the burning experiments with the online detection, the metals (Pb, Zn) also exhibited a significant increase in emissions from the experimental soils at temperatures higher than 600–650 °C (Fig. 4a). A similar increase was observed for Pb and Zn from the heated slag dust (Fig. 4b), which corroborates to the emissions of the Pb–Zn slag-like aerosols captured on the filters (Figure S5). Despite the relatively low quality of the signal, other peaks of the Zn release were reported for the combusted slag and flue dust (Fig. 4b) at 550–600 °C, probably corresponding to the thermal transformation of ZnS, which was also observed in the industrial waste samples as an important Zn-bearing solid (Table 1).

The releases of As and S as a function of temperature were significantly more complicated for the experimental soils (Fig. 4b). Three significant releases of As from the experimental samples occurred with peaks at ~275 °C (sample AM only), ~370–410 °C, and ~580 °C (all the samples). The As emissions, at similar temperatures (250, 380–450 and 650 °C), were observed for the heated mine tailing dust, where As was mainly found in the secondary Fe oxides, metal arsenates [duftite, PbCu(AsO_4)(OH) and conichalcite, CaCu(AsO_4)(OH)] and sulfides/sulfosalts (e.g., enargite, Cu_3AsS_4) (see the mineralogical compositions in Table 1).

Fig. 5 shows a comparison of the total and released concentrations of metal(loid)s in the experimental samples for the combustion experiments conducted at 850 °C, representing a "worst-case scenario", potentially occurring in the contaminated wooded savanna. The contaminant emissions were calculated as a percentage of the totals, corresponding to 5–14% As, 2–12% Cu, 3–17% Pb, 2–20% Zn and 27–79% Cd (note that for Cd, the total concentrations are significantly lower compared to the other metal(loid)s) (Fig. 5).

4. Discussion

4.1. Potential metal(loid) remobilization from the topsoil by heating during wildfires

Metals (Cd, Cu, Pb, Zn) remain in the ash of the heated topsoils and are released only at high temperatures. This may be partly related to the thermal degradation of carbonates, being important hosts of Cd, Cu, Pb, and Zn in the experimental soils (Tables 1 and 2; Tuhý et al., 2020b). However, at high temperatures, metals are also emitted in a particulate form only as demonstrated by the presence of the metal-bearing aerosols trapped by filtering the smoke at 850 °C (Figure S5). Jahn et al. (2021) observed that similarly complex aerosols <1 μm in size, corresponding to the fine ash particles ejected by the combustion process during the biomass burning, were substantially enriched in Zn (>0.5 at.%).

The temperature-dependent As release from the topsoils obtained by the continuous temperature increase experiment reflects its complex speciation in the solid phase. The first peak at 250 °C could be related to the thermal degradation of the As-bearing hydrous ferric oxides (HFO), which, for the experimental sample AM (and mine tailing), are dominant As carriers (Tuhý et al., 2020b) (Table 2). Johnston et al. (2016, 2018, 2019) studied the release of As from various As-bearing Fe phases (schwertmannite, ferrihydrite, goethite) under simulated fire conditions in a temperature range of 200–800 °C and found that, apart from the phase transformations, the biomass burning produces the reducing gases responsible for the reduction of As(V) to As(III), which is then easily volatilized. For instance, during the combustion of organic-rich soils containing As-bearing schwertmannite, even short-term heating (5–10 min) at > 300 °C can lead to a substantial As reduction (Johnston et al., 2018) and similar results were observed for As-bearing ferrihydrite and goethite, although re-oxidation to As(V) can occur for more extended combustion periods (>60 min) (Johnston et al., 2019).

The multiple peaks of As emissions in the temperature range of 370–410 °C observed for the experimental soil samples likely correspond to the complex decomposition of various species (Fig. 4a). A distinct peak at 350 °C is consistent with an arsenolite (As_2O_3) thermal transformation, the dominant As-bearing phase in the smelter flue dust (Fig. 4b) (Jarošíková et al., 2018). The thermogravimetric analysis (TGA) indicated that arsenolite is completely volatilized at 350 °C (Kercher and Nagle, 2001). The pyrolysis experiments with As_2O_3 adsorbed on the activated carbon showed that the major As volatilization occurs between 300 and 500 °C (Cuypers et al., 2009). Tiny

arsenolite crystals found on the biomass fragments (Fig. 2b,d) can be volatilized during the soil organic matter pyrolysis. Moreover, the large peak of S emissions observed at 390 °C (Fig. 4a) may also correspond to the organic matter's thermal degradation. This S emissions agree with the experimental data of Tiedemann (1987), who combusted forest foliage and litter at 375–575 °C for 5 min, and found that S losses ranged from 24 to 79%. The As release from the soils and mine tailing samples in this temperature range can also be related to the thermal degradation of metal arsenates, which are among the key hosts of As (e.g., duftite, conichalcite) (Fig. 4a and b; Tables 1 and 2). However, the thermal stabilities of many specific arsenate minerals are unknown. Whereas arsenates of the vivianite group $[(Mg,Co,Ni)_3(AsO_4)_2{\cdot}8H_2O]$ decompose at 750–800 °C (Frost et al., 2003), investigation of some fumarolic arsenates indicates that their thermal stability goes to much lower temperatures (≥450 °C) (Pekov et al., 2018). Combustion experiments with chromated copper arsenate (CCA)-treated wood waste demonstrated that the reductive pyrolysis is responsible for the transformation of As (V) species into As_2O_3, which sublimates from the matrix at temperatures around 400–500 °C (Kakitani et al., 2004; Cuypers and Helsen, 2011). Incineration of *Pteris vittata*, an As-hyperaccumulator, indicated that 24% of the total arsenic was emitted at 800 °C, of which 62.5% of the released As was volatilized at <400 °C; this process was also attributed to the As(V) reduction to As(III) (Yan et al., 2008). Additional experiments with As-rich *P. vittata* also reported a substantial increase in an As release between 400 and 600 °C during pyrolysis and gasification (Duan et al., 2017). We hypothesize that similar processes can be responsible for the thermal decomposition of the arsenate phases in the given temperature range (350–450 °C), but further experimentation is needed to verify this. Apatite is another key host of As in the heavy mineral fraction of the experimental soils (samples A and G; Tables 1 and 2) (Tuhý et al., 2020b); the As emissions in the given temperature range may be partly related to the apatite thermal decomposition. Two to four stages of mass loss have been observed for hydroxyapatite in the low-temperature region, up to 500 °C (Tonsuaadu et al., 2012), but detailed investigations of the As release from the apatite structures have never been conducted.

Our combustion experiments with the experimental soils demonstrated a sharp As emission peak centered around 580 °C, which corroborates with a peak in the S release (~600 °C) (Fig. 4a). Similar peaks at 650 °C (As) and 600–700 °C (S) can be noticed for the industrial waste samples (Fig. 4b). We assume that this release is closely related to the thermal instability of enargite and/or sulfides, which are quite abundant in the experimental soils and technological samples (Tables 1 and 2) (Ettler et al., 2009; Ettler et al., 2014; Jarošíková et al., 2017, 2018; Tuhý et al., 2020b). The experimental studies indicate that enargite, in the absence of oxygen, starts to decompose at ~550 °C and it fully transforms to Cu_2S and As vapors between 500 and 700 °C (Safarzadeh and Miller, 2016).

4.2. Environmental implications

Similar to the wildfire-driven remobilization of Pb in urban or industrialized areas, where contamination is mostly attributed to legacy leaded petrol combustion (Odigie et al., 2011, 2014; Kristensen and Taylor, 2012; Kristensen et al., 2014; Wu et al., 2017), contamination hotspots near metal mines and smelters in areas exposed to frequent wildfires (e.g., Australia, the Americas, Siberia, southern Africa) may be a significant source of metal(loid)s remobilization (Mihaljevič et al., 2011; Ettler et al., 2014; Abraham et al., 2018b; Tuhý et al., 2020a). The consequences of wildfire effects on the soils and the living vegetation in areas polluted by mining and smelting are dependent on many parameters: the total concentrations and solid speciation of contaminants, the particle sizes, the character of the fuel and its content, and the fire intensity and severity.

The high absolute numbers of the potential remobilizations observed in our experiments are closely related to high total concentrations of the individual metal(loid) (Fig. 5). The situation might be different in more distant areas, although the "halo" of the topsoil and vegetation contamination around the Tsumeb smelter is quite extensive (Kříbek et al., 2016). According to the modeling of the dust fallout (Kříbek et al., 2016), the contaminants were transported to the NW to a distance of >10 km from the smelter stack, mostly reflecting the prevailing wind direction (Figure S1). The average area of the contamination hotspot around the Tsumeb smelter was calculated from the spatial distribution maps (Kříbek et al., 2016; Tuhý et al., 2020a) and corresponded to ca. 10 km^2. This hotspot area seems to be quite small, but due to its local importance, it but must be definitely protected against wildfires to avoid the potential re-emissions of the contaminants.

We recognize the many limitations of our wildfire simulations. Our data indicate that such contaminated topsoils exhibit a high complexity in the metal(loid)s solid speciation and thermally induced transformations. The thermal stabilities and related element emissions, especially under wildfire-simulated conditions, have not been determined for many of the metal(loid)-hosting minerals and phases. As a result, to better interpret the temperature-dependent release patterns, similar experiments should be performed on these compounds and/or their mixtures with lab-prepared soil analogs or uncontaminated soils, inspired by previous studies on the thermal alteration of As-bearing Fe oxides (Johnston et al., 2016, 2018, 2019). Further experimentation is needed to understand the nature of aerosols and gaseous emissions from these combusted topsoils to quantify the wildfire-induced fluxes of the individual elements better and to improve the mass-balance calculations. This study raises many other questions, such as (i) if (and how) such lab-scale burning experiments can be extrapolated to real-scale conditions given the spatial variability in the vegetation cover and the soil composition (e.g., complexity in the partitioning of the contaminants) and (ii) how to design the *in situ* burning experiments to overcome all the mentioned difficulties.

5. Conclusions

Biomass-rich topsoils polluted by the nearby Cu smelter located in semi-arid Namibia were investigated by a series of laboratory combustion experiments to simulate the metal(loid)s behavior during wildfires. We have introduced a novel experimental setup, which (i) includes a continuous airflow more closely simulating the natural wildfire regime than in conventional muffle furnace experiments and (ii) enables aerosol sampling.

The metal(loid)s' temperature-dependent releases were controlled by their speciation in the solid phase. Metals (Cd, Cu, Pb, Zn) were only released at relatively high temperatures (>550–600 °C), and, at 850 °C, detected in the form of metal-bearing aerosols. As a result, these metals are mainly concentrated in the ash during low-intensity wildfires, but can be subsequently mobilized into other environmental compartments (e.g., surface water) or transported by wind. In contrast, upon heating, As exhibited several emission peaks (~275 °C, ~370–410 °C, and ~580 °C) due to the successive releases from various As-bearing phases (e.g., hydrous ferric oxides, arsenolite, metal arsenates, sulfosalts). Despite the spatial limitation of the presented study, our results clearly indicate that mining and smelting sites in semi-arid areas, especially those highly enriched in As, need protection against wildfires to avoid the potential re-emissions of inorganic contaminants.

Declaration of competing interest

The authors declare that they have no known competing financial interests or personal relationships that could have appeared to influence the work reported in this paper.

Acknowledgments

This study received funding from the Czech Science Foundation

(GAČR project no. 19-18513S), and a student project from the Grant Agency of Charles University attributed to Marek Tuhý (GAUK 1598218). The Charles University team was partially supported by institutional funding from the Center for Geosphere Dynamics (UNCE/SCI/006). The research at the Institute of Geology ASCR was co-financed by the institutional support of RVO 67985831. We acknowledge many colleagues for their help in the laboratory: Martin Racek (SEM/EDS, FEG-EPMA), Petr Drahota (XRD), Aleš Vaněk and Vít Penížek (field sampling). Mr. Alan Harvey Cook is thanked for his review of the English in the manuscript. We acknowledge the thorough reviews of three anonymous reviewers, which substantially helped to improve the original version of the manuscript.

Appendix A. Supplementary data

Supplementary data to this article can be found online at https://doi.org/10.1016/j.jenvman.2021.112899.

Credit authors statement – author contributions

Conceptualization: Marek Tuhý, Vojtěch Ettler, Jan Rohovec, Data curation: Marek Tuhý, Vojtěch Ettler, Jan Rohovec, Šárka Matoušková, Martin Mihaljevič, Bohdan Kříbek, Ben Mapani, Formal analysis: Marek Tuhý, Vojtěch Ettler, Jan Rohovec, Šárka Matoušková, Funding acquisition: Vojtěch Ettler, Marek Tuhý, Jan Rohovec. Investigation: Marek Tuhý, Vojtěch Ettler, Jan Rohovec. Methodology: Marek Tuhý, Vojtěch Ettler, Jan Rohovec. Project administration: Marek Tuhý, Vojtěch Ettler, Resources: Vojtěch Ettler, Martin Mihaljevič, Bohdan Kříbek, Ben Mapani. Supervision: Vojtěch Ettler. Validation: Vojtěch Ettler. Visualization: Marek Tuhý, Vojtěch Ettler. Roles/Writing - original draft: Marek Tuhý, Vojtěch Ettler. Writing - review & editing: Jan Rohovec, Šárka Matoušková, Martin Mihaljevič, Bohdan Kříbek, Ben Mapani.

References

Abraham, J., Dowling, K., Florentine, S., 2017. Risk of post-fire metal mobilization into surface water resources: a review. Sci. Total Environ. 599–600, 1740–1755. https://doi.org/10.1016/j.scitotenv.2017.05.096.

Abraham, J., Dowling, K., Florentine, S., 2018a. Effects of prescribed fire and post-fire rainfall on mercury mobilization and subsequent contamination assessment in a legacy mine site in Victoria, Australia. Chemosphere 190, 144–153. https://doi.org/10.1016/j.chemosphere.2017.09.117.

Abraham, J., Dowling, K., Florentine, S., 2018b. Influence of controlled burning on the mobility and temporal variations of potentially toxic metals (PTMs) in the soils of a legacy gold mine site in Central Victoria, Australia. Geoderma 331, 1–14. https://doi.org/10.1016/j.geoderma.2018.06.010.

Badía, D., López-García, S., Ortíz-Perpiñá, O., Girona-García, A., Casanova-Gascón, J., 2017. Burn effects on soil properties associated to heat transfer under contrasting moisture content. Sci. Total Environ. 601–602, 1119–1128. https://doi.org/10.1016/j.scitotenv.2017.05.254.

Bladon, K.D., Emelko, M.B., Silins, U., Stone, M., 2014. Wildfire and the future of water supply. Environ. Sci. Technol. 48, 8936–8943. https://doi.org/10.1021/es500130g.

Campos, I., Vale, C., Abrantes, N., Keizer, J.J., Pereira, P., 2015. Effect of wildfire on mercury mobilization in eucalypt and pine forests. Catena 131, 149–159. https://doi.org/10.1016/j.catena.2015.02.024.

Campos, I., Abrantes, N., Keizer, J.J., Vale, C., Pereira, P., 2016. Major and trace elements in soils and ashes of eucalypt and pine forest plantation in Portugal following a wildfire. Sci. Total Environ. 572, 1363–1376. https://doi.org/10.1016/j.scitotenv.2016.01.190.

Cerrato, J.M., Blake, J.M., Hirani, C., Clark, A.L., Ali, A.M.S., Artyushkova, K., Peterson, E., Bixby, R.J., 2016. Wildfires and water chemistry: effect of metals associated with wood ash. Environ. Sci. Process. Impacts 18, 1078–1089. https://doi.org/10.1039/C6EM00123H.

Creamean, J.M., Neiman, P.J., Coleman, T., Senff, C.J., Kirgis, G., Alvarez, R.J., Yamamoto, A., 2016. Colorado air quality impacted by long-range-transported aerosol: a set of case studies during the 2015 Pacific Northwest fires. Atmos. Chem. Phys. 16, 12329–12345. https://doi.org/10.5194/acp-16-12329-2016.

Cuypers, F., De Dobbelaere, C., Hardy, A., Van Bael, M.K., Helsen, L., 2009. Thermal behavior of arsenic trioxide adsorbed on activated carbon. J. Hazard Mater. 166, 1238–1243. https://doi.org/10.1016/j.jhazmat.2008.12.048.

Cuypers, F., Helsen, L., 2011. Pyrolysis of chromated copper arsenate (CCA) treated wood waste at elevated pressure: influence of particle size, heating rate, residence time, temperature and pressure. J. Anal. Appl. Pyrol. 92, 111–122. https://doi.org/10.1016/j.jaap.2011.05.002.

Duan, L., Li, X., Jiang, Y., Lei, M., Dong, Z., Longhurst, P., 2017. Arsenic transformation behavior during thermal decomposition of *P. vittata*, and arsenic hyperaccumulator. J. Anal. Appl. Pyrol. 124, 584–591. https://doi.org/10.1016/j.jaap.2017.01.013.

Ettler, V., Johan, Z., Kříbek, B., Šebek, O., Mihaljevič, M., 2009. Mineralogy and environmental stability of slags from the Tsumeb smelter, Namibia. Appl. Geochem. 24, 1–15. https://doi.org/10.1016/j.apgeochem.2008.10.003.

Ettler, V., Konečný, L., Kovářová, L., Mihaljevič, M., Šebek, O., Kříbek, B., Majer, V., Veselovský, F., Penížek, V., Vaněk, A., Nyambe, I., 2014. Surprisingly contrasting metals distribution and fractionation patterns in copper smelter-affected tropical soils in forested and grassland areas (Mufulira, Zambian Copperbelt). Sci. Total Environ. 473–474, 117–124. https://doi.org/10.1016/j.scitotenv.2013.11.146.

Ettler, V., Johan, Z., Kříbek, B., Veselovský, F., Mihaljevič, M., Vaněk, A., Penížek, V., Majer, V., Sracek, O., Mapani, B., Kamona, F., Nyambe, I., 2016. Composition and fate of mine- and smelter-derived particles in soils of humid subtropical and hot semi-arid areas. Sci. Total Environ. 563–564, 329–339. https://doi.org/10.1016/j.scitotenv.2016.04.133.

Ettler, V., Cihlová, M., Jarošíková, A., Mihaljevič, M., Drahota, P., Kříbek, B., Vaněk, A., Penížek, V., Šráček, O., Klementová, M., Engel, Z., Kamona, F., Mapani, B., 2019. Oral bioaccessibility of metal(loid)s in dust materials from mining areas of northern Namibia. Environ. Int. 124, 2005–2015. https://doi.org/10.1016/j.envint.2018.12.027.

Friedli, H., Arellano, A., Cinnirella, S., Pirrone, N., 2009. Initial estimates of mercury emissions to the atmosphere from global biomass burning. Environ. Sci. Technol. 43, 3507–3513. https://doi.org/10.1021/es802703g.

Frost, R.L., Weier, M.L., Martens, W., Kloprogge, J.T., Ding, Z., 2003. Thermal decomposition of the vivianite arsenates – implications for soil remediation. Thermochim. Acta 403, 237–249. https://doi.org/10.1016/S0040-6031(03)00046-7.

Gaudichet, A., Echalar, F., Chatenet, B., Quisefit, J.P., Malingre, G., Cachier, H., Buat-Menard, P., Artaxo, P., Maenhaut, W., Trace elements in tropical African savanna biomass burning aerosols. J. Atmos. Chem. 22, 19-39. https://doi.org/10.1007/BF00708179.

Girona-García, A., Badía-Villas, D., Martí-Dalmau, C., Ortiz-Perpiñá, O., Mora, J.L., Armas-Herrera, C.M., Effects of prescribed fire for pasture management on soil organic matter and biological properties: A 1-year study case in the Central Pyrenees. Sci. Total Environ. 618, 1079-1087. https://doi.org/10.1016/j.scitotenv.2017.09.127.

Goss, M., Swain, D.L., Abatzoglou, J.T., Sarhadi, A., Kolden, C.A., Williams, A.P., Diffenbaugh, N.S., 2020. Climate change is increasing the likelihood of extreme autumn wildfire conditions across California. Environ. Res. Lett. 15, 094016 https://doi.org/10.1088/1748-9326/ab83a7.

Howard, D., Macsween, K., Edwards, G.C., Desservettaz, M., Guérette, E.-A., Paton-Walsh, C., Surawski, N.C., Sullivan, A.L., Weston, C., Volkova, L., Powell, J., Keywood, M.D., Reisen, F., Meyer, C.P.M., 2019. Investigation of mercury emissions from burning of Australian eucalypt forest surface fuels using a combustion wind tunnel and field observations. Atmos. Environ. 202, 17–27. https://doi.org/10.1016/j.atmosenv.2018.12.015.

Isley, C.F., Taylor, M.P., 2020. Atmospheric remobilization of natural and anthropogenic contaminants during wildfires. Environ. Pollut. 267, 115400. https://doi.org/10.1016/j.envpol.2020.115400.

Jahn, L.G., Jahl, L.G., Bland, G.D., Monroe, L.W., Sullivan, R.C., 2021. Metallic and crustal elements in biomass-burning aerosol and ash: prevalence, significance, and similarity to soil particles. ACS Earth Space Chem 5, 136–148. https://doi.org/10.1021/acsearthspacechem.0c00191.

Jarošíková, A., Ettler, V., Mihaljevič, M., Kříbek, B., Mapani, B., 2017. The pH-dependent leaching behavior of slags from various stages of a copper smelting process: environmental implications. J. Environ. Manag. 187, 178–186. https://doi.org/10.1016/j.jenvman.2016.11.037.

Jarošíková, A., Ettler, V., Mihaljevič, M., Drahota, P., Culka, A., Racek, M., 2018. Characterization and pH-dependent environmental stability of arsenic trioxide-containing copper smelter flue dust. J. Environ. Manag. 209, 71–80. https://doi.org/10.1016/j.jenvman.2017.12.044.

Johnston, S.G., Burton, E.D., Moon, E.M., 2016. Arsenic mobilization is enhanced by thermal transformation of schwertmannite. Environ. Sci. Technol. 50, 8010–8019. https://doi.org/10.1021/acs.est.6b02618.

Johnston, S.G., Bennett, W.W., Burton, E.D., Hockmann, K., Dawson, N., Karimian, N., 2018. Rapid arsenic(V)-reduction by fire in schwertmannite-rich soil enhances arsenic mobilization. Geochem. Cosmochim. Acta 227, 1–18. https://doi.org/10.1016/j.gca.2018.01.031.

Johnston, S.G., Karimian, N., Burton, E.D., 2019. Fire promotes arsenic mobilization and rapid arsenic(III) formation in soil via thermal alteration of arsenic-bearing iron oxides. Front. Earth Sci. 7, 139. https://doi.org/10.3389/feart.2019.00139.

Kakitani, T., Hata, T., Kajimoto, T., Imamira, Y., 2004. Two possible pathways for the release of arsenic during pyrolysis of chromated copper arsenate (CCA)-treated wood. J. Hazard Mater. B 113, 247–252. https://doi.org/10.1016/j.jhazmat.2004.05.029.

Kayee, J., Sompongchaiyakul, P., Sanwlani, N., Bureekul, S., Wang, X., Das, R., 2020. Metal concentrations and source apportionment of PM2.5 in Chiang Rai and Bangkok, Thailand during a biomass burning season. ACS Earth Space Chem 4, 1213–1226. https://doi.org/10.1021/acsearthspacechem.0c00140.

Kganyago, M., Shikwambana, L., 2020. Assessment of the characteristics of recent Major wildfires in the USA, Australia and Brazil in 2018–2019 using multi-source satellite products. Rem. Sens. 12, 1803. https://doi.org/10.3390/rs12111803.

Kercher, A.K., Nagle, D.C., 2001. TGA modeling of the thermal decomposition of CCA treated lumber waste. Wood Sci. Technol. 35, 325–341. https://doi.org/10.1007/s002260100094.

Kříbek, B., Majer, V., Knésl, I., Keder, J., Mapani, B., Kamona, F., Mihaljevič, M., Ettler, V., Penížek, V., Vaněk, A., Šráček, O., 2016. Contamination of soil and grass in the Tsumeb smelter area, Namibia: modeling of contaminants dispersion and ground geochemical verification. Appl. Geochem. 64, 75–91. https://doi.org/10.1016/j.apgeochem.2015.07.006.

Kristensen, L.J., Taylor, M.P., 2012. Fields and forests in flames: lead and mercury emissions from wildfire pyrogenic activity. Environ. Health Perspect. 120, A56–A57. https://doi.org/10.1289/ehp.1104672.

Kristensen, L.J., Taylor, M.P., Odigie, K.O., Hibdon, S.A., Flegal, A.R., 2014. Lead isotopic compositions of ash sourced from Australian bushfires. Environ. Pollut. 190, 159–165. https://doi.org/10.1016/j.envpol.2014.03.025.

Kristensen, L.J., Taylor, M.P., Flegal, A.R., 2017. An odyssey of environmental pollution: the rise, fall and remobilisation of industrial lead in Australia. Appl. Geochem. 83, 3–13. https://doi.org/10.1016/j.apgeochem.2017.02.007.

Mihaljevič, M., Ettler, V., Šebek, O., Sracek, O., Kříbek, B., Kyncl, T., Majer, V., Veselovský, F., 2011. Lead isotopic and metallic pollution record in tree rings from the Copperbelt mining-smelting area, Zambia. Water Air Soil Pollut. 216, 657–668. https://doi.org/10.1007/s11270-010-0560-4.

Mihaljevič, M., Ettler, V., Vaněk, A., Penížek, V., Svoboda, M., Kříbek, B., Sracek, O., Mapani, B.S., Kamona, A.F., 2015. Trace elements and the lead isotopic record in marula (*Sclerocarya birrea*) tree rings and soils near the Tsumeb smelter, Namibia. Water Air Soil Pollut. 226, 177. https://doi.org/10.1007/s11270-015-2440-4.

Muñoz-Rojas, M., Pereira, P., 2020. Editorial: fire in the environment. J. Environ. Manag. 253, 109703. https://doi.org/10.1016/j.envman.2019.109703.

Nriagu, J.O., 1989. A global assessment of natural sources of atmospheric trace metals. Nature 338, 47–49. https://doi.org/10.1038/338047a0.

Odigie, K.O., Flegal, A.R., 2011. Pyrogenic remobilization of historic industrial lead depositions. Environ. Sci. Technol. 45, 6290–6295. https://doi.org/10.1021/es200944w.

Odigie, K.O., Flegal, A.R., 2014. Trace metal inventories and lead isotopic composition chronicle a forest fire's remobilization of industrial contaminants deposited in the Angeles National Forest. PloS One 9, e107835. https://doi.org/10.1371/journal.pone.0107835.

Pekov, I.V., Koshlyakova, N.N., Zubkova, N.V., Lykova, I.S., Britvin, S.N., Yapaskurt, V.O., Agakhanov, A.A., Shchipalkina, N.V., Turchkova, A.G., Sidorov, E.G., 2018. Fumarolic arsenates – a special type of arsenic mineralization. Eur. J. Mineral 30, 305–322. https://doi.org/10.1127/ejm/2018/0030-2718.

Pereira, P., Mataix-Solera, J., Úbeda, X., Rein, G., Cerdà, A. (Eds.), 2019. Fire Effects on Soil Properties. CSIRO Publishing, Clayton South, ISBN 9781486308132.

Rahman, A., El Hayek, E., Blake, J.M., Bixby, R.J., Ali, A.M., Spilde, M., Otieno, A.A., Miltenberger, K., Ridgeway, C., Artyushkova, K., Atudorei, V., Cerrato, J.M., 2018. Metal reactivity in laboratory burned wood from a watershed affected by wildfires. Environ. Sci. Technol. 52, 8115–8123. https://doi.org/10.1021/acs.est.8b00530.

Ryan, K.C., 2002. Dynamic interactions between forest structure and fire behavior in boreal ecosystems. Silva Fenn. 36, 13–39. https://doi.org/10.14214/sf.548.

Safarzadeh, M.S., Miller, J.D., 2016. The pyrometallurgy of enargite: a literature update. Int. J. Miner. Process. 157, 103–110. https://doi.org/10.1016/j.minpro.2016.09.008.

Tiedemann, A.R., 1987. Combustion losses of sulfur from forest foliage and litter. Forest Sci 33, 216–223. https://doi.org/10.1093/forestscience/33.1.216.

Tonsuaadu, K., Gross, K.A., Pluduma, L., Veiderma, M., 2012. A review on the thermal stability of calcium apatites. J. Therm. Anal. Calorim. 110, 647–659. https://doi.org/10.1007/s10973-011-1877-y.

Tuhý, M., Rohovec, J., Matoušková, Š., Mihaljevič, M., Kříbek, B., Vaněk, A., Mapani, B., Göttlicher, J., Steininger, R., Majzlan, J., Ettler, V., 2020a. The potential wildfire effects on mercury remobilization from topsoils and biomass in a smelter-polluted semi-arid area. Chemosphere 247, 125972. https://doi.org/10.1016/j.chemosphere.2020.125972.

Tuhý, M., Hrstka, T., Ettler, V., 2020b. Automated mineralogy for quantification and partitioning of metal(loid)s in particulates from mining/smelting-polluted soils. Environ. Pollut. 226, 115118. https://doi.org/10.1016/j.envpol.2020.115118.

Weber, K.T., Yadav, R., 2020. Spatiotemporal trends in wildfires across the western United States (1950–2019). Rem. Sens. 12, 2959. https://doi.org/10.3390/rs12182959.

Weinhold, B., 2011. Fields and forests in flames: vegetation smoke and human health. Environ. Health Perspect. 119, A236–A393. https://doi.org/10.1289/ehp.119-a386.

Westerling, A.L., Hidalgo, H.G., Cayan, D.R., Swetnam, T.W., 2006. Warming and earlier spring increase western U.S. forest wildfire activity. Science 313, 940–943. https://doi.org/10.1126/science.1128834.

Wiedinmeyer, C., Friedli, H., 2007. Mercury emission estimates from fires: an initial inventory for the United States. Environ. Sci. Technol. 41, 8092–8098. https://doi.org/10.1021/es071289o.

Witze, A., 2020. Why Arctic fires are bad news for climate change. Nature 585, 336–337. https://doi.org/10.1038/d41586-020-02568-y.

Wu, L., Taylor, M.P., Handley, H.K., 2017. Remobilisations of industrial lead depositions in ash during Australian wildfires. Sci. Total Environ. 599–600, 1233–1240. https://doi.org/10.1016/j.scitotenv.2017.05.044.

Yan, X.L., Chen, T.B., Liao, X.Y., Huang, Z.C., Pan, J.R., Hu, T.D., Nie, C.J., Xie, H., 2008. Arsenic transformation and volatilization during incineration of the hyperaccumulator *Pteris vittata* L. Environ. Sci. Technol. 42, 1479–1484. https://doi.org/10.1021/es0717459.

Young, D.R., Jan, T.K., 1977. Fire fallout of metals off California. Mar. Pollut. Bull. 8, 109–112. https://doi.org/10.1016/0025-326X(77)90133-3.

IV

Tuhý, M., Ettler, V., Rohovec, J., Matoušková, Š., Mihaljevič, M., Kříbek, B., Mapani, B., Wildfires remobilize metal(loid)s from contaminated grass in mining areas of sub-Saharan Africa (unpublished results)

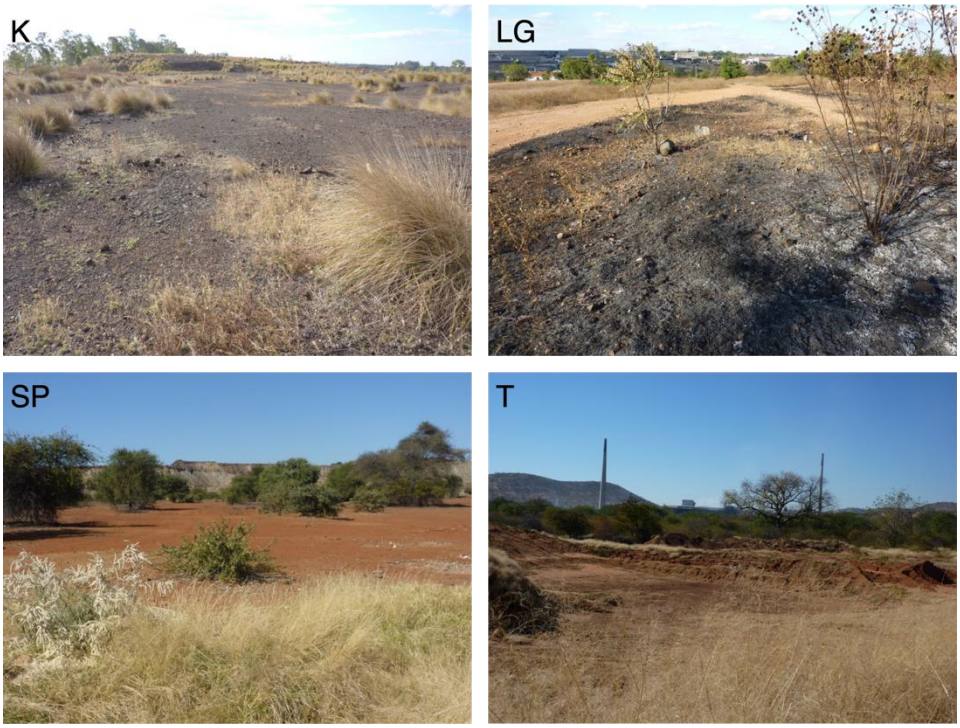

Figure AIV-1. Abandoned and active mining/smelting sites, where experimental biomass/grass samples were collected. K – slag dumps with grass cover (Kabwe, Zambia); LG – recently burned surroundings of the Luanshya smelter (Zambian Copperbelt); SP – area downwind the smelter in Selebi-Phikwe (Botswana); T – grassland plots downwind the Tsumeb smelter (Namibia).

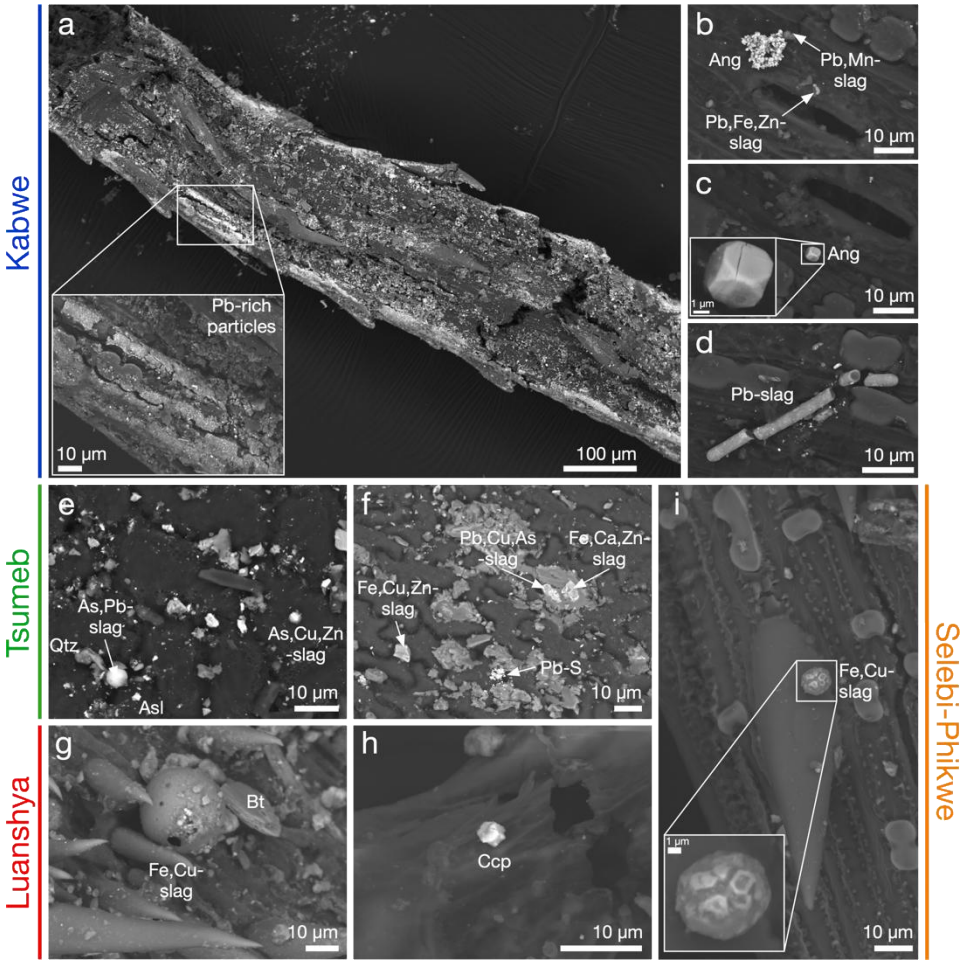

Figure AIV-2. Micrographs of particles adhering to the grass surface obtained by FEG-SEM. a) Surface of a grass fragment from Kabwe highly enriched in anthropogenic and geogenic particles; b) Pb-rich slag particles associated to newly formed submicrometric anglesite aggregates (Ang; $PbSO_4$), c) Pseudomorphoses of anglesite after galena (PbS); d) Elongated Pb-slag particles; e,f) Grass fragments from Tsumeb containing both geogenic particles (Qtz – quartz, SiO_2), metal(loid)-bearing slags and arsenolite (Asl; As_2O_3); g,h) Plants fragments from Luanshya with a spherical Cu-rich slag particle in association with biotite [Bt, $K(Mg,Fe^{2+})_3[(OH,F)_2(Al,Fe^{3+})Si_3O_{10}]$] and a grain of chalcopyrite ($CuFeS_2$); i) Heterogeneous spherical slag particle from Selebi-Phikwe enriched in Fe and Cu attached to grass surface.

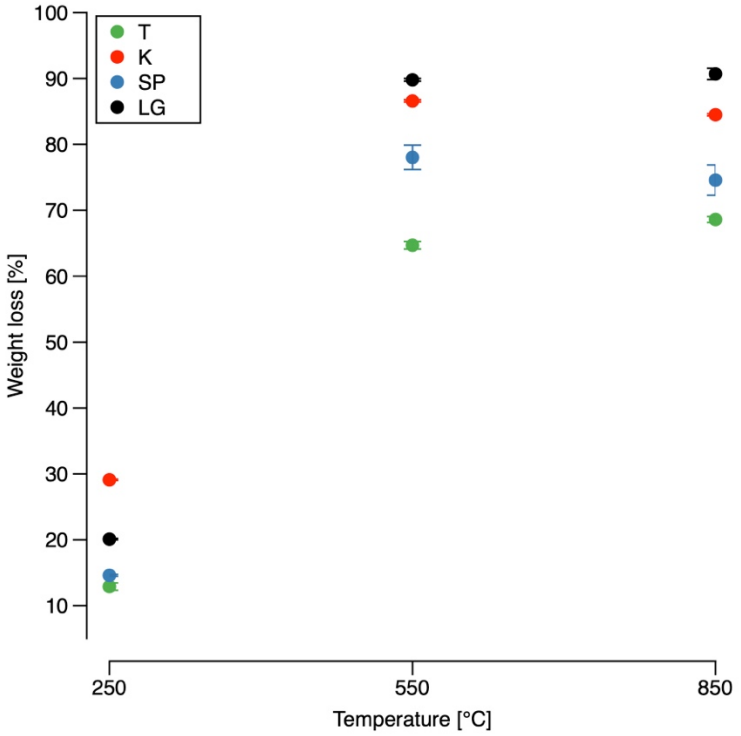

Figure AIV-3. Weight losses of biomass samples after a wildfire-simulating experiment as obtained at temperatures of 250 °C, 550 °C, and 850 °C. Error bars correspond to standard deviations obtained from replicated experiment (n = 3). Abbreviations: T – Tsumeb; K – Kabwe; SP – Selebi-Phikwe; LG – Luanshya.

Figure AIV-4. Photographs of the ashes obtained during the biomass-burning experiment at individual temperatures (250 °C, 550 °C and 850 °C). The colors were determined according to the Munsell color system (Munsell Soil Color Chart). Abbreviations: T – Tsumeb; K – Kabwe; SP – Selebi-Phikwe; LG – Luanshya.

Table AIV-1. Total concentrations (mg/kg) of metal(loid)s in original experimental biomass samples and ashes obtained during the wildfire-simulating experiment. Abbreviations: T – Tsumeb; K – Kabwe; SP – Selebi-Phikwe; LG – Luanshya.

Sample		**As**	**Cd**	**Co**	**Cr**	**Cu**	**Ni**	**Pb**	**Sb**	**Zn**
G		725±8	11.0±1.4	4.00±0.00	14.3±0.5	2070±40	4.00±0.00	1770±240	32.0±3.6	1290±40
K		<5.00	0.67±0.00	2.22±0.02	39.6±0.8	24.5±2.3	27.7±0.8	316±4	0.43±0.01	300±7
LG		<5.00	0.37±0.01	12.7±1.2	124±7	1460±212	73.2±3.1	12.0±0.4	0.14±0.03	73.0±1.3
SP		<5.00	0.68±0.09	31.8±10.2	149±16	677±188	555±142	7.25±1.85	<0.17	27.7±4.7
Ash	**Temperature [°C]**	**As**	**Cd**	**Co**	**Cr**	**Cu**	**Ni**	**Pb**	**Sb**	**Zn**
G	250	858±13	25.0±1.5	8.68±0.89	32.3±0.4	2410±50	7.97±0.24	1230±10	70.0±3.6	1600±0.6
G	550	1940±20	45.4±3.0	15.8±0.5	55.8±1.6	5830±30	14.0±0.2	4280±20	132±9	3570±30
G	850	2100±1	8.07±2.08	24.7±0.7	82.5±0.3	7130±460	20.5±0.5	3510±180	154±2	3620±10
K	250	9.00±4.00	1.00±0.00	1.50±0.50	20.5±2.5	23.0±1.0	10.5±0.5	294±13	<0.34	297±12
K	550	16.0±11.0	5.50±0.5	14.0±0.1	160±4	189±2	87.5±3.5	2160±60	3.50±0.50	2050±50
K	850	39.0±1.0	5.00±3.00	19.0±2.0	186±8	318±61	106±7	2100±150	4.50±0.50	2480±70
LG	250	20.1±3.5	0.47±0.00	9.39±0.48	45.9±3.6	1460±10	24.2±0.6	8.76±0.56	0.23±0.00	213±1
LG	550	42.4±11.7	4.17±0.19	134±7	577±51	14500±200	341±39	86.9±3.8	2.88±0.20	1930±20
LG	850	64.4±1.3	10.7±1.6	157±6	709±50	14300±800	365±8	747±162	4.32±0.36	2240±20
SP	250	20.3±0.3	0.75±0.04	14.2±5.0	143±46	550±179	546±169	5.96±1.61	0.04±0.01	36.0±4.6
SP	550	29.0±5.2	2.31±0.03	51.3±1.5	495±2	1660±1	1570±30	20.0±1.1	0.17±0.01	114±2
SP	850	29.0±5.2	3.18±0.18	85.2±3.6	517±47	2180±110	1830±60	105±53	0.42±0.09	165±31

V

Tuhý, M., Ettler, V., 2020. Přírodní požáry a remobilizace kovů. *Vesmír* 99: 458-460.

Přírodní požáry a remobilizace kovů

Pozornost veřejnosti v roce 2019 upoutaly rozsáhlé přírodní požáry Amazonie, Portugalska a ruské Sibiře. Požáry v Austrálii se nekontrolovaně šířily ještě počátkem roku 2020 na rozloze větší než 110 000 km². Vyžádaly si nejen lidské oběti a škody na majetku, ale také ovlivnily ekosystémy na dosud nevídaných plochách. Požáry se šíří i do člověkem kontaminovaných oblastí. Nedochází tak k významným emisím kovů a dalších polutantů do atmosféry?

text **MAREK TUHÝ, VOJTĚCH ETTLER**

ZE SEDIMENTÁRNÍHO záznamu je patrné, že požáry jsou na naší planetě přirozeným jevem již 400 milionů let. Jejich četnost se úměrně zvyšovala s rostoucím zastoupením kyslíku v atmosféře [1]. V některých oblastech jsou přirozené požáry nezbytné pro správné fungování ekosystému. Například australské blahovičníkové (*Eucalyptus*) porosty jsou z hlediska reprodukce na požárech přímo závislé. Dokonce sám blahovičník z povrchu svých listů uvolňuje těkavé hořlaviny, a tím sám vybízí k zahoření, které má za následek nejen rozpukání semen a snazší klíčivost, ale i vyhoření podrostu a zvýšení konkurenceschopnosti mladých blahovičníků. Ohořelý kmen je poté schopen znovu obrůst výhonky a porost se tímto procesem obnovuje.

Nejinak je tomu i v afrických savanách. Existence savany je přímo závislá na epizodickém hoření. Savana nikdy úplně nezarostete dřevinami, protože ty po požáru regenerují pomaleji než tráva. Čím více je v savaně travin, tím je vyšší četnost požárů a savana si tak přirozeně udržuje svůj charakter [2].

Mezi pozitivní efekty požárů patří redukce přebytečné biomasy, přirozené udržování biodiverzity a vznik popela, který působí jako půdní hnojivo (to je ostatně jedním z důvodů řízeného vypalování porostů v nejrůznějších koutech světa). Kromě zjevných benefitů mají požáry i svá úskalí, jako například emise skleníkových plynů a částic do atmosféry, zvýšení náchylnosti půdy k erozi, prohřátí svrchních půdních horizontů a s tím související vliv na půdní biotu [3].

Přestože víme, že člověk má na svědomí větší část emisí kovů do atmosféry, přírodní

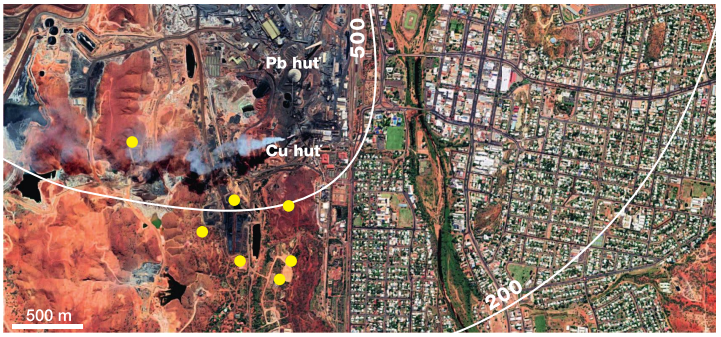

1. OKOLÍ METALURGICKÝCH PROVOZŮ na lokalitě Mount Isa v Austrálii se zřetelnou kouřovou vlečkou z komína měděné hutě (Google Maps, 23. 1. 2020). Izolinie vymezují místa o stejné roční depozici olova (500 a 200 mg/m²/rok) [5]. Na snímku jsou žlutě vynesena ohniska požárů ze dne 20. 1. 2020 (Fire Watch Landgate [6]).

Mgr. MAREK TUHÝ (*1993) vystudoval geologii na Přírodovědecké fakultě UK. Je doktorandem Ústavu geochemie, mineralogie a nerostných zdrojů na PřF UK, kde se věnuje problematice požárů v kontaminovaných oblastech. Zabývá se mineralogií, experimentální mineralogií a geochemií.

Prof. RNDr. VOJTĚCH ETTLER, Ph.D., (*1974) vystudoval Přírodovědeckou fakultu UK a Université d'Orléans ve Francii. Působí v Ústavu geochemie, mineralogie a nerostných zdrojů PřF UK. Jeho výzkum je zaměřen na enviromentální mineralogii a geochemii s důrazem na chování odpadů z vysokoteplotních technologií a kontaminaci životního prostředí v těžebních oblastech.

Snímky Vojtěch Ettler

2. POŽÁRY V SUBSAHARSKÉ AFRICE: A. přírodní požár v blízkosti dolu na zlato a přilehlých odkališť u Johannesburgu (JAR); B. hořící travní porost v těžbou kontaminované oblasti Tsumeb (Namibie); C. kouř z rozsáhlého požáru savany v oblasti Tsumebu; D. spáleniště v národním parku Pilanesberg (JAR).

zdroje mají také nezanedbatelný význam. Jedním z nich jsou i přirozené požáry, u nichž první výpočty ukázaly, že se podílejí na téměř 17 % z celkových emisí olova i zinku z přírodních zdrojů [4]. K mnohem významnější remobilizaci kovů a polokovů do atmosféry však může docházet při požárech v oblastech znečištěných činností člověka. Rozsáhlé požáry v Austrálii se počátkem letošního roku nevyhnuly ani takovým místům. Ohniska požárů byla zaznamenána i v bezprostřední blízkosti hutního provozu u hornického města Mount Isa v severozápadním Queenslandu, kde se kvůli vysoké depozici antropogenních částic ve svrchních půdách vyskytují koncentrace kovů a polokovů v řádu tisíců mg/kg (**obr. 1**).

K hoření dochází také v těžebních oblastech subsaharské Afriky (**obr. 2**). Důležitým faktorem ovlivňujícím reemise kovů a polokovů ze svrchního půdního horizontu je teplota, která určuje intenzitu požáru. Nepřímým indikátorem intenzity požáru je pak barva vzniklého popela. Požáry travin jsou velmi rychlé, místními obyvateli dokonce nazývané „running fires“, vykazují relativně nízké teploty hoření (cca 350 °C) a vzniká při nich popel zpravidla tmavě šedé až černé barvy. Naopak v místech s dostatkem paliva (opadanka, dřeviny) mohou teploty přesahovat i 1000 °C. Již při teplotách nad 550 °C vzniká popel světlý [7] – na **obr. 2D** pozorujeme zřetelné rozdíly v barvě popela pod akáciemi a na vypálené travnaté ploše.

Emise z těžebních a hutních provozů a větrná eroze jsou přímo zodpovědné za transport částic s obsahem kontaminantů. Rostliny je vychytávají z atmosféry (**obr. 3A–C**) a prostřednictvím opadu, případně přímou depozicí do půdy se tyto částice dostávají do svrchního půdního horizontu (**obr. 3D, E**), kde se kontaminanty koncentrují. Právě tato připovrchová vrstva o mocnosti do 1 cm je při požáru zahřívána na nejvyšší teplotu.

Faktorů ovlivňujících náchylnost jednotlivých prvků k remobilizaci při požáru je však více. Kromě teploty je klíčová zejména forma vazby prvku v půdě a biomase. Například rtuť v blízkosti hutních provozů je do půd a biomasy deponovaná jako plynná Hg^0, případně ve formě sulfidu, váže se na organickou hmotu nebo je přítomna ve formě nanočástic a je při požáru uvolnitelná již při nízkých teplotách (cca. 350 °C). Během požárů travnaté savany se tak veškerá rtuť uvolní do atmosféry, kde má dlouhou dobu setrvání, a stane se tak součástí globálního cyklu. Například při vyhoření území o rozloze 184 km² v okolí měděné huti v semiaridní Namibii by došlo k uvolnění přibližně 300 kg rtuti. [8]

Jiné kontaminanty (olovo, měď, zinek, kadmium, arzen) se uvolňují výrazně méně a míra jejich remobilizace závisí na vazbě v hořlavém substrátu. Například mikročástice arzenolitu (As_2O_3), emitované hutním provozem a zachycené na povrchu vegetace (**obr. 3B**), jsou nestabilní již při nízkoteplotním hoření. Naše experimenty ukazují, že pokud bychom v okolí takové huti předpokládali požár s teplotami do 850 °C, do atmosféry by se z kontaminovaného hořlavého materiálu uvolnilo až 17 % z celkového množství těchto prvků. To představuje stovky miligramů každého z kontaminantů

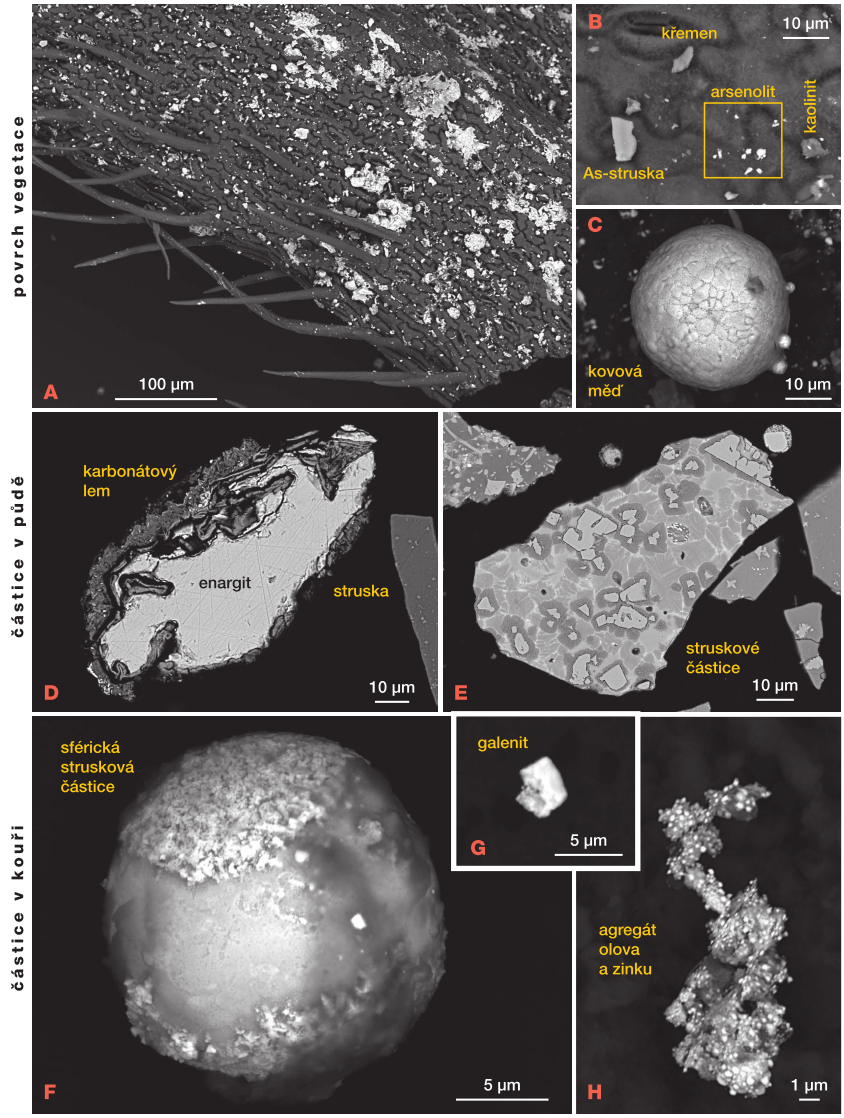

3. MIKROFOTOGRAFIE Z ŘÁDKOVACÍHO ELEKTRONOVÉHO MIKROSKOPU: **A–C. částice pocházející z odkališť důlních odpadů a hutních provozů a zachycené na povrchu vegetace; D. rudní a E. struskové částice separované z kontaminovaných svrchních půdních horizontů; F–H. aerosolové částice emitované při laboratorních simulacích požárů kontaminované biomasy svrchního půdního horizontu. Chemické vzorce minerálů či fází s obsahem kovů a polokovů: arsenolit (As_2O_3), enargit (Cu_3AsS_4), galenit (PbS).**

na jeden kilogram spálené svrchní půdní vrstvy.

Potenciálně toxické prvky mohou být v kouři unášeny ve formě malých částic (**obr. 3F–H**). Podle odhadů Světové meteorologické organizace migroval dým z nedávných australských požárů přes oceán až do Chile a na Antarktidu. Tímto způsobem se tak signál původně lokálního antropogenního znečištění šíří na značné vzdálenosti. Zbytek kontaminantů koncentrovaný v popelu i tak představuje lokální environmentální zátěž. V průběhu požáru může dojít k mineralogickým transformacím, a tím ke změně formy vazby kontaminantů a zvýšení jejich vyluhovatelnosti. Popel jako jemnozrnný materiál s velkým měrným povrchem také může být snadno unášen větrem i vodou a šířit se tak do okolního prostředí.

Zdá se, že četnost i intenzita přírodních požárů jsou v posledních letech na vzestupu. Lze očekávat, že se současné požáry velice brzy dostanou do hledáčku geochemiků i dalších environmentálních badatelů. Cílem takových výzkumů by měly být kromě jiného zejména přesnější popis toků jednotlivých prvků a určení vlivu požárů na globální cykly polutantů. ●

Poděkování: *Studie byla podpořena projektem GA UK 1598218 a Centrem pro dynamiku geosféry (UNCE/SCI/006) při Univerzitě Karlově. Experimenty probíhaly ve spolupráci s J. Rohovcem a Š. Matouškovou z Geologického ústavu AV ČR.*

K dalšímu čtení…

[1] Scott A. C.: Burning Planet. Oxford University Press 2018, ISBN 978-0-19-873484-0.
[2] Pokorný P. (ed.) et al.: Afrika zevnitř. Kontinentem sucha a věčných proměn. Academia 2016, ISBN 978-80-200-2627-9, viz také Vesmír 95, 572, 2016/10.
[3] Pereira P. et al.: Fire Effects on Soil Properties. CSIRO Publishing 2019, ISBN 978-0-367-18655-5.
[4] Nriagu J. O.: Nature, 1989, DOI: 10.1038/338047a0.
[5] Wilson I. H.: Applied Geochemistry, 2018, DOI: 10.1016/j.apgeochem.2018.04.007.
[6] Fire Watch Landgate, firewatch-pro.landgate.wa.gov.au.
[7] Bodí M. B. et al.: Earth-Science Reviews, 2014, DOI: doi.org/10.1016/j.earscirev.2013.12.007.
[8] Tuhý M. et al.: Chemosphere, 2020, DOI: 10.1016/j.chemosphere.2020.125972.